Ab Initio Modeling of Thermal Barrier Coatings: Effects of Dopants and Impurities on Interface Adhesion, Diffusion and Grain Boundary Strength

Asli Isil Ozfidan

Thesis submitted to the
Faculty of Graduate and Postdoctoral Studies
in partial fulfillment of the requirements for the

MSc degree in physics

Department of Physics
Faculty of Science
University of Ottawa

Abstract

The aim of this thesis is to investigate the effects of additives, reactive elements and impurities, on the lifetime of thermal barrier coatings. The thesis consists of a number of studies on interface adhesion, impurity diffusion, grain boundary sliding and cleavage processes and their impact on the mechanical behaviour of grain boundaries.

The effects of additives and impurity on interface adhesion were elaborated by using total energy calculations, electron localization and density of states, and by looking into the atomic separations. The results of these calculations allow the assessment of atomic level contributions to changes in the adhesive trend. Formation of new bonds across the interface is determined to improve the adhesion in reactive element(RE)-doped structures. Breaking of the cross interface bonds and sulfur(S)-oxygen(O) repulsion is found responsible for the decreased adhesion after S segregation.

Interstitial and vacancy mediated S diffusion and the effects of Hf and Pt on the diffusion rate of S in bulk NiAl are studied. Hf is shown to reduce the diffusion rate, and the preferred diffusion mechanism of S and the influence of Pt are revealed to be temperature dependent.

Finally, the effects of reactive elements on alumina grain boundary strength are studied. Reactive elements are shown to improve both the sliding and cleavage resistance, and the analysis of atomic separations suggest an increased ductility after the addition of quadrivalent Hf and Zr to the alumina grain boundaries.

Statement of Originality

The current thesis is realized under Dr. Kuiying Chen's immediate supervision at the Structures and Materials Performance Laboratory - Institute of Aerospace Research - National Research Council Canada (NRC). All the calculations and atomic model creations reported are performed by the author with the help of Dr. Kuiying Chen who independently verified the author's results.

Acknowledgements

I am thankful to my supervisor, Dr Kuiying Chen, whose encouragement, patience, guidance and support was indispensable throughout this project. I am grateful to the National Research Council of Canada (NRC) for allowing me to use their facilities.

I should also thank my friends and family who have supported me and helped me during the completion of this thesis.

This project was financially supported by the Natural Science and Engineering Research Council of Canada (NSERC). Also it was made possible by the facilities of the Shared Hierarchical Academic Research Computing Network (SHARCNET: www.sharcnet.ca) and Compute/Calcul Canada.

Contents

List of Figures

List of Tables

List of Abbreviations

6JC	Six Jump Cycle
ASB	Anti Structure Bridge mechanism
ASP	Aluminium Sublattice Plane
ATAT	Alloy Theoric Automated Toolkit
BCC	Body Centered Cubic
CINEB	Climbing Image Nudged Elastic Band
DFT	Density Functional Theory
DOS	Density Of States
EB-PVD	Electron Beam Physical Vapor Deposition
ELF	Electron Localization Function
ELNES	Electron Energy-Loss Near Edge Structure
FCC	Face Centered Cubic
GB	Grain Boundary
GGA	Generalized Gradient Approximation
HCP	Hexagonal Closed Packed
LDA	Local Density Approximation
LEED	Low Energy Electron Diffraction
LEPS	London-Eyring-Polanyi-Sato potential
LUP	Locally Updated Planes
MEP	Minimum Energy Path
NEB	Nudged Elastic Band
NNN	Next Nearest Neigbour mechanism
NSP	Nickel Sublattice Plane
PAW	projector augmented wave
PS	Plasma Sprayed
RE	Reactive Element
TBC	Thermal Barrier Coating
TD	Triple Defect
TGO	Thermally Grown Oxide
UBER	Universal Binding Energy Relation
US-PP	Ultra Soft Pseudo Potential
VASP	Vienna Ab initio Simulation Package
YSZ	Yttria-Stabilized Zirconia

Chapter 1

Introduction

1.1 Thesis Motivation and Outline

Improvements in technology have led to a need for high performance gas turbine engines that can work at high operating temperatures and harsh environments. Application of advanced cooling schemes together with deposition of thermal barrier coatings (TBCs) on engine components can maximize the engine efficiency and lifetime. With the application of TBCs, the need for cooling air is decreased and higher operating temperatures can be reached without affecting the component integrity, leading to reduction in fuel consumption and increase in the power to weight ratios.

TBCs typically have 3 main components: the bond coat (NiAl) deposited on turbine blades, the thermally grown oxide (TGO (Al_2O_3)) which grows as a result of oxidation, and finally the top coat to protect the component from high temperatures. The failure of TBC systems mostly occurs at the TGO/bond coat interface, and addition of reactive elements or diffusion of impurities to this interface affects the bonding strength and the lifetime. The reactive elements are also known to segregate from the interface to TGO grain boundaries (GB), altering the GB strength and changing the threshold stresses required for the onset of deformation. A literature review about the TGO/bond coat interface, diffusion of segregants in NiAl, and the Al_2O_3 grain boundaries is provided in Chapter 1.

Microscopic level models are developed for investigating the TGO/bond coat interface, diffusion in the bond coat, and the TGO properties where the interactions between atoms are elaborated using density functional theory to link microscopic mechanisms to macroscopic properties. The computational methods used are explained in Chapter 2 and a brief theoretical review is provided in Chapter 3.

Chapter 4 concentrates on the effects of alloying element (Pt), reactive elements (Hf, Cr, Zr, Y) and impurity (S), alone or in combination on the adhesive trends of the TGO/bond coat interface. S diffusion in NiAl and the effects of Hf and Pt on the diffusion rate of S are analyzed in Chapter 5. Finally, Chapter 6 focuses on the $\Sigma 3$ Al_2O_3 GB and the effects of reactive elements on the cleavage and slip behavior of this GB.

Chapter 7 is the conclusion of this thesis summarizing the key findings and outlining further research.

1.2 Literature Review

TBCs exhibit low thermal conductivity that is essential for reducing the heat transfer from the hot combustion gas to the turbine blade substrate. In addition, some advanced TBCs also provide protection against oxidation and hot corrosion. In order to achieve both low thermal conductivity and high oxidation resistance, a multilayered coating scheme is used (Figure 1.1).

In a typical TBC system, there are three primary layers: the top coat, the bond coat and the thermally grown oxide (TGO). The thermally insulating ceramic-based top coat is deposited on top of a metallic bond coat that protects the substrate from oxidation and hot corrosion. Yttrium stabilized zirconia (YSZ) is preferred as the ceramic top coat material while the bond coat is a nickel-based alloy (for instance β-

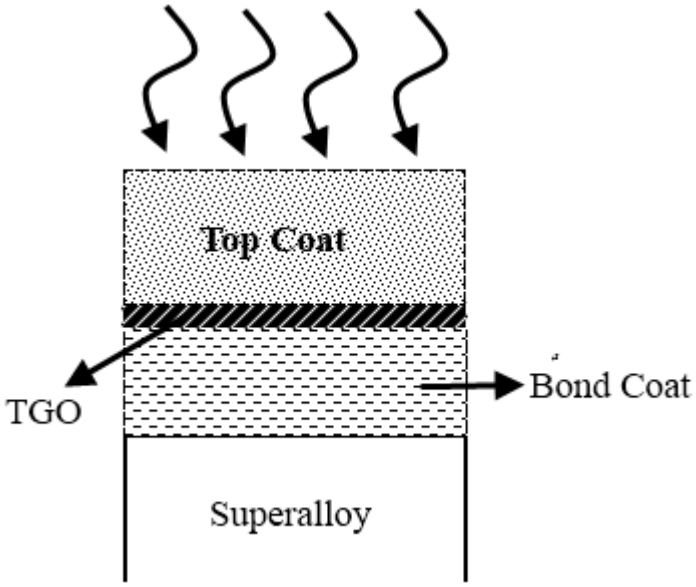

Figure 1.1: Cross section of a TBC: The thermally insulating top coat, the bond coat to alleviate the thermal expansion mismatch and the thermally grown oxide that grows from the oxidation of the bond coat.

NiAl) that usually contains elements such as Cr, Pt, Y and Hf to increase its lifetime [1]. The bond coat acts as a bridge, connecting the substrate and the top coat in order to minimize the strains caused by the thermal expansion mismatch [2]. The TGO layer is formed through oxidation of the bond coat and it provides protection against oxidation and corrosion. However, its thickening causes spalls along the TGO-bond coat interface [2], thus the bond coat is designed to form Al_2O_3 that has a low growth rate and greater stability and adherence compared to other oxides [3].

Among ceramics, ZrO_2 is found to be the ideal choice as a top coat material owing to its low thermal conductivity, high thermal expansion coefficient and good thermal shock resistance [4]. At low temperatures, from 0 to 1180°C, ZrO_2 has a monoclinic symmetry. However at higher temperatures, above 1180°C, it becomes unstable, decomposing to a mixture of cubic and tetragonal zirconia [5]. In order to overcome this issue, the cubic phase of ZrO_2 is stabilized at ambient temperatures by doping with Y_2O_3. The dopant cations substitute for Zr sites and create oxygen vacancies. The presence of vacancies

reduces the zirconia coordination number from eight (in cubic and tetragonal) to a value closer to seven as in monoclinic phase.

There are two major types of metallic bond coats that are designed to form α-Al_2O_3 as their oxides. One is based on a MCrAlY-type composition (M stands for one or more of these elements Co, Ni, Fe). In these type of metallic bond coats, Y improves the adherence of the oxide scale by gettering S, and Cr functions to increase the chemical activity of Al. The other type of metallic bond coat is a Pt modified nickel-aluminide (PtNiAl), which is preferred in higher temperature operating conditions.

The two principal deposition techniques that are used in TBC fabrication are the plasma spraying (PS) and the electron beam physical vapor deposition (EB-PVD). Both techniques are used for deposition of the top coat and the bond coat, however both have their drawbacks. The discontinuity formation during the solidifying process in PS technique may cause weak adhesion; while in EB-PVD method, there is a possibility of spallation occurring at the top coat-bond coat interface during the cooling process [1]. Different failure mechanisms are observed in EB-PVD and PS deposited TBCs. PS deposition is preferred on rough bond coats and failure occurs by crack evolution in the top coat, whereas EB-PVD is used on smoother bond coats and failure occurs at the TGO/bond coat interface by the loss of adherence [3]. When compared, TBCs deposited by the EB-PVD method have a longer lifetime, smoother surface finish, superior erosion resistance and better stress compliance due to their columnar structure [4, 6].

Failure mechanisms have been extensively studied by several researchers [3, 7–10] in order to improve the lifetime of TBCs. The two main factors that initiate the TBC failure are observed as: i) the interfacial structure; weakening of the adhesion between the bond coat/TGO and the topcoat/TGO interfaces and ii) the elastic and thermal property mismatch (thermal expansion and thermal conductivity) among these layers.

During oxide growth, the bond coat roughens and causes localized flaws that even-

tually link together with nearby flaws and cause large scale buckling and spallation failure. As the TGO layer thickens, lateral compressive stresses are developed due to the thermal expansion mismatch between the materials used. However, because the TGO is adhered to the bond coat, it cannot expand and it undulates to reduce the strain energy. This undulation causes oxide and alloy deformation and localized voids at the interface. These voids start a folding effect, leading to cracking and spallation of TBC at various points. Cracking causes the TBC to lose its function, and the substrate becomes thermally unprotected [3]. Since the failure of TBC often results from delamination of the TGO/bond coat interface, it is important to understand the nature of the interfacial elastic and thermal properties together with the mechanisms and factors initiating the failure.

1.2.1 TGO/Bond Coat Interface

It is necessary to understand the interfacial bonding mechanism and develop methods to improve the adhesive strength of interfaces since most spallation in TBCs occurs at the TGO/bond coat interface [11–15]. After deposition, the bond coat shows a homogeneous β-NiAl structure. However during thermal cycling, aluminum depletes due to oxide formation and some parts of β-NiAl transforms into γ'-Ni_3Al. The oxide (Al_2O_3) forms on the NiAl(110) surface with different surface terminations and usually crystallizes in the corundum (sapphire, α-Al_2O_3) form that grows with its (0001) plane parallel to NiAl(110) [11, 16, 17]. In order to observe the failure mechanisms and effects of thermal cycling on the TGO/bond coat adherence, Al_2O_3/Ni, Al_2O_3/NiAl and Al_2O_3/Ni_3Al interfaces have been studied both theoretically and experimentally [12, 13, 18–25].

Nickel has a face-centered-cubic (FCC) structure with a melting point of 1453°C. The adhesion of Al_2O_3 on pure Ni substrate is investigated since the interactions

between Ni and Al_{oxide} atoms play a major role on the interfacial adhesion trends of Ni/Al_2O_3, $NiAl/Al_2O_3$ and Ni_3Al/Al_2O_3. Special attention is given to Ni(111) surface because it possess the lowest lattice misfit with $Al_2O_3(0001)$ [25] and forms the most stable interface [16]. γ'-Ni_3Al also has an FCC structure and the (111) surface is its closest-packed surface. It possesses 75 %at Ni, 25 %at Al, and has a surface rippling of 0.06 Å [26, 27]. At high temperatures, α-$Al_2O_3(0001)$ is found to grow parallel to this surface, and formation of γ'-Ni_3Al is proposed to facilitate the formation of Ni-Al bonds instead of a brittle spinel phase containing Ni-O bonds [16, 20].

NiAl, unlike Ni_3Al and Ni, has a body-centered-cubic (BCC) lattice structure with 1640°C melting point. Although it is highly resistant to oxidation at high temperatures, it has a poor fracture resistance at ambient temperatures [18, 28]. The ordered NiAl has a typical CsCl-type structure with a lattice constant of 2.887Å. Its (110) plane (dimensions 2.887Å x $2.887\sqrt{2}$Å and interlayer spacing $2.887/\sqrt{2}$Å) consists of composite Ni-Al layers with each layer containing 50-50 Ni-Al sites (Figure 1.2). A rippling geometry at the outer layer of this plane is observed in several experimental studies [29–33]. At the topmost layer, Al atoms are observed to move outwards, while the Ni atoms were relaxing inwards, towards the second Ni-Al layer, corresponding to a rippling amplitude of 0.22Å. A rippled structure is found in the first layer of NiAl(110) using theoretical approaches, in agreement with previous experimental observations, [27, 34, 35]. Kang and Mele [35] proposed two different forces that might be causing the inward relaxation of Ni atoms, i.e., enhanced interlayer attraction due to reduction of repulsive *s, p* electrons between layers, and the interaction of ion cores and d electrons of Ni atoms with redistributed *s, p* electrons. For the second layer, a smaller oscillatory rippling is observed compared to the first layer, with Ni atoms displacing up away and Al down towards the bulk NiAl [33, 35]. Such oscillatory behavior is explained by the repulsion between the Ni atoms from the first layer and the Al *s, p* electrons from the second layer. However, since the results found were within the error

bars of the experiments and calculations, no certain conclusion is made about relaxed structure of the second layer.

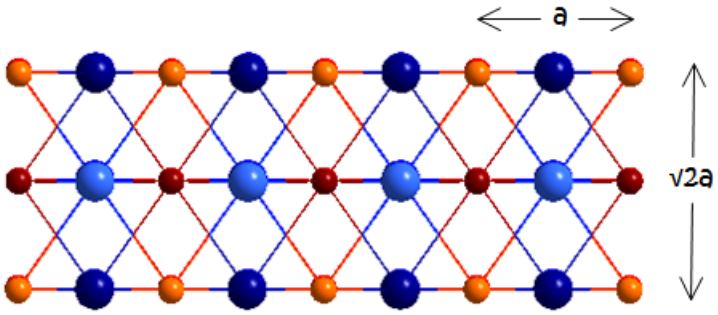

Figure 1.2: Ideal NiAl(110) surface. orange, light blue, red and blue colors corresponds to 1st layer Al, 1st layer Ni, 2nd layer Al and 2nd layer Ni atoms respectively

In previous experimental studies [11–15, 36, 37], a well-defined long range structure of a distorted hexagonal Al_2O_3 as the oxide film formed on the NiAl(110) surface is observed, and the Al terminated Al_2O_3 layer is found to form the most stable interface. The oxide mesh formed on NiAl is determined to be rotated by 24° with respect to the substrate, and its real space unit mesh is calculated as (A_1=10.55Å, A_2=17.88Å, γ=88.7) using low energy electron diffraction (LEED) [36] and X-ray diffraction [13] experiments, which is much larger than that of the NiAl(110) mesh (A_1=2.887, A_2=4.083, γ=90) [12, 14, 37]. Furthermore, greater rippling of Al and Ni atoms is observed on the oxide covered NiAl(110) compared to the oxide-free NiAl(110) surface [13].

Sulfur is present at every step of deposition as well as in combustion gases and is known to have detrimental effects on the oxide/bond coat adherence. During oxide growth, it segregates to the metal surface and to the metal/oxide interface, promoting void and defect formation, decreasing the interface and surface energy, and consequently causing spallation [38–44]. The segregated S is observed to get trapped at the interface, contributing to void growth, and with increasing S content, an increased cavity formation followed by a significant mass loss is detected [44]. The effects of sulfur on the bond coat/TGO interface are studied using computational methods to understand

the atomic-scale aspects of spallation [17, 45–48]. The simulations showed that the S atoms segregating to the bond coat-oxide interface tend to reside on the metal surface rather than moving towards the oxide. Carling *et.al.* studied the site preference of S on the NiAl(110) metal surface and found the three-fold 2Ni-Al site as the most stable adsorption position for S [49].

Various methods are being developed in order to mitigate the detrimental effects of S. Modifying the bond coat structure using additives is one of the strategies employed. Pt is known to improve the oxide adhesion and is shown to slow down the S segregation to the interface [50, 51]. In compositional profile analyses, the Pt atoms segregating to the interface are found to substitute for Ni atoms [25]. In short term isothermal oxidation tests, it is observed to improve the scale adhesion by increasing the oxide growth that fills up the voids and reduces the void formation [25, 40, 52, 53]. However in long term cycles, again due to increased scale growth rates, thickening of the oxide layer eventually triggers creep and plastic deformations and causes spallation.

The effects of Pt are also studied in atomic level using density functional theory (DFT) calculations [54–57]. Two different Pt adsorption sites are modelled: 1) as a Ni or Al substitute and 2) at the metal/oxide interface. Once Ni site preference of Pt atoms in β-NiAl is verified using DFT methods, the adhesion of the clean, and Pt modified interfaces are calculated. Even though, experimentally, Pt is shown to improve the TBC lifetime, no significant change in the interface adhesion is observed after its addition in DFT calculations. In order to clarify this conflict, it is suggested to improve the lifetime by promoting Al diffusion to the interface concomitant with increased oxide growth that prevents formation of fast growing, brittle Ni-rich oxides. Supporting this proposition, Marino *et. al.* observed an increase in Al diffusion rate in the presence of Pt [58]. Thus, reduced S segregation and increased Al diffusion to the interface are considered to be the main causes of enhanced TBC lifetime.

At lower temperatures, the oxide grows on the bond coat with its metastable, fast

growing γ and θ phases. In general, reactive elements (RE) are known to promote transformations from fast growing γ and θ-Al_2O_3 phases to stable, protective and slow growing α-Al_2O_3 phase [59, 60]. Thus, addition of most reactive elements into the bond coat is found to slow down the oxide growth rate, increase the stability of its β-phase and consequently improve the lifetime of the TBC [61–63]. In addition to reducing the oxide growth rate, REs are also known to increase the TBC lifetime by inhibiting the void formation and forming strong sulphides within bulk NiAl to stop S diffusion to the interface [43, 44, 64–66]. Especially Hf, Y and Zr are known to be the most effective dopants in decreasing S segregation and improving the cyclic oxidation resistance [60, 67]. These positive effects of REs are also suggested to be associated with their segregation from the bond coat to metal-oxide interface, towards the oxide grain boundaries to form RE-oxides [63, 68].

To explain the improved scale adherence in atomic level, using DFT calculations a metal-oxide interface with an Hf additive is modeled. These calculations showed that its tendency to move towards the oxide is due to the strong, partly ionic-partly covalent Hf-O bonds [17]. Moreover, as expected, addition of Hf to the interface or as a substitute in the bond coat is determined to increase the adhesion of the interface [17, 46].

Just like other reactive elements, Cr promotes θ to γ phase transformations, decreases the interfacial void growth and increases the fracture toughness of NiAl [69, 70]. However it is proposed that addition of Cr deteriorates the oxide adhesion by increasing the oxide formation rate [68, 71, 72]: At the early stages of Cr containing bond coats, the hexagonal Cr_2O_3 is formed at the bond coat surface which acts as nuclei to form finer grained hexagonal α-Al_2O_3. Due to its fine grained structure, it provides more paths for Al and O diffusion that causes greater oxidation. In addition, it is found to co-segregate with S, increasing S content at the interface [73]. This behaviour is shown to cause plastic deformations and result in reduced TBC lifetime. Addition of

Zr to Cr containing alloys is found to improve oxidation resistance, however not enough to outweigh the increased oxide growth rate due to presence of Cr [74]. Similarly, Cr addition to a Hf doped bond coat is found to increase oxide growth and spallation rates [68].

Compared to Hf or Zr, Y is shown to be less effective in reducing the oxide growth and small amounts of yttrium-sulfide is observed at the metal-oxide interface [75, 76]. Furthermore, co-doping Y with Hf or Zr is found to be more efficient than purely Y, Hf or Zr doped structures, and a slower oxide growth is observed in Y+Zr and Y+Hf doped interfaces [77–79].

1.2.2 Diffusion in NiAl

Self-diffusion and diffusion of REs or impurities in NiAl are dominant mechanisms effecting the oxide growth and oxide spallation rates in TBCs. As explained previously, segregation of impurities, such as S, reduces the surface energy and initiates void and crack nucleation, while self-diffusion of Al to the metal surface increases the oxide growth rate. Thus the diffusion phenomenon is very important in understanding oxide adherence and in enhancing the TBC lifetime.

Since both Ni and Al atoms possess large atomic radii, the self-diffusion in NiAl occurs via vacancy formation. However, more complex vacancy mediated diffusion mechanisms have been proposed for self-diffusion in NiAl, because diffusion by a random nearest neighbor jump creates disorder in the structure. Triple defect mechanism (TD), anti-structural bridge mechanism (ASB), next nearest neighbor jump (NNN) and six jump cycles (6JC), all of which requires complex defect structures, are explained in detail in Chapter 3. NiAl is known for its capacity to accommodate excess Ni and Al atoms and it is agreed upon that the concentration of the NiAl alloy is a factor affecting the diffusion mechanism [80, 81]. Depending on the concentration and the temperature,

four types of defects exist in NiAl; vacancy on a Ni (V_{Ni}) or an Al (V_{Al}) lattice site, and anti-structure atoms (Ni atom at an Al site (Ni_{Al}) or an Al atom at a Ni site (Al_{Ni})). The NiAl anti-structure atoms are commonly encountered in Ni-rich NiAl alloys while the V_{Ni} vacancies are common in Al-rich compositions [80]. Some of the factors used in determining the diffusion rate are the migration energy, formation energy and the jump frequency. These factors, which are explained in detail in Chapter 3, are also considered to be important in determining the preferred diffusion mechanisms.

Ni self-diffusion in NiAl

Self-diffusion of Ni in B2-NiAl alloy is measured at various compositions and over a wide temperature range, since the preferred diffusion mechanisms are known to be concentration dependent. It is agreed that at temperatures over 1000K, for Al-rich and stoichiometric compositions, Ni prefers a triple defect mechanism while for Ni-rich side of the composition the ASB mechanism is shown to be dominant [80, 82]. In agreement with experimental data, theoretically, the TD is found to be the most plausible mechanism due to its low diffusion barrier [83, 84], and for Ni-rich side, an increased anti-site concentration that is essential for diffusion by the ASB mechanism is predicted [85, 86]. In addition, the NNN mechanism is proposed to occur concurrently with other mechanisms due to its low energy barrier [87]. Finally, even though some researchers proposed the 6JC as the major diffusion mechanism, it is later shown to be dominant at low temperatures (T<1000K) and at stoichiometric composition only [88–90].

Al self-diffusion in NiAl

Minamino *et. al.* [91] calculated the formation and migration energies of Al self-diffusion in Ni rich and stoichiometric NiAl. For Al self-diffusion, they proposed NNN or Ni-ASB mechanism in Ni-rich NiAl, and a possible TD mechanism in stoichiometric NiAl. In agreement, Nakamura *et. al.* [82] used Kirkendall effect and showed that at high temperatures, TD is dominant for Al self-diffusion in stoichiometric and Ni-rich compositions. Furthermore theoretically Xu *et. al.* [85] predicted the ASB mechanism for Al diffusion while Marino *et. al.* [58, 86] proposed ASB would contribute only to short range Al diffusion and that TD mechanism will dominate long range Al diffusion in both Ni rich and stoichiometric compositions.

In order to assess the effects of additives on Ni and Al self-diffusion, Marino *et. al.* studied Ni and Al self-diffusion in the presence of Pt using first principles [58, 86]. In agreement with previous experimental data [52, 92], they found that addition of Pt increased the diffusion rate of Ni and Al for all proposed mechanisms by decreasing the migration barrier. They concluded that an enhanced Al diffusion rate due to the Pt addition is one of the reasons for increased TBC lifetime.

Diffusion of Impurities and Additives in NiAl

Diffusion of S within NiAl is proposed to be by an interstitial mechanism due to its lower diffusion rate compared to Ni self-diffusion in NiAl [38, 93]. Whereas the diffusion of Pt in NiAl is observed to be mainly by TD, ASB and NNN at stoichiometric, Ni-rich and Al-rich sides of the composition, respectively [91]. Since Pt is suggested to have an effect on S diffusion rates in NiAl, Christien *et. al.* [94] measured the concentration profiles by Auger electron spectroscopy. They found that below 900°C, S atoms are diffusing faster after Pt addition, while beyond 900°C, Pt was delaying the S diffusion to the interface. Similarly Hou *et. al.* showed that Pt was reducing the S segregation

on both stoichiometric and Ni-rich NiAl surfaces [50].

1.2.3 Al_2O_3 Grain Boundary

Failure is an important phenomenon in determining the lifetime of TBCs, and the stresses acting on the TGO layer play a major role. During thermal cycles, most imperfections occur at TGO grain boundaries (GB), and the stresses caused by thermal expansion mismatch and the TGO growth are alleviated by displacement of neighboring grains parallel or perpendicular to the boundary. Due to its wide range of applications, mechanical properties of Al_2O_3 GBs and the effects of segregants on the properties of these GBs are studied by many researchers [95–113]. Sliding is determined as the dominant process in creep of alumina grain boundaries which is shown to be affected by segregation of reactive elements. Hf, Y, Zr, and other REs are determined to decrease the creep rate significantly, and in tensile tests, YSZ addition is observed to improve the tensile strength of the oxide.

Fabris *et. al.* analyzed different terminations of the $\Sigma13$ $(10\bar{1}4)$ Al_2O_3 symmetrical tilt and the $\Sigma3$ $(10\bar{1}0)$ Al_2O_3 GBs using DFT for both, and additionally ELNES for the $\Sigma3$ GB. In their study they demonstrated that a combination of experimental and computational observations is far more reliable compared to the information gathered from individual methods [95, 98, 99, 108, 109, 114]. A similar conclusion, that a combination of methods is more reliable, is drawn from Milas *et. al.*'s studies, in which the cohesive properties and sliding barriers of $\Sigma11$ tilt GB with and without segregants are calculated [111, 112]. Even though, a weaker adhesion is determined after Y segregation, the sliding barrier in the Y and other RE doped grain boundaries are much higher than the un-doped interface as expected. In addition to improving the sliding barrier, Y is shown to improve the tensile strength of $\Sigma3$ GBs in theoretical tensile tests, in agreement with experimental observations [100, 102, 106, 111, 115]. Vacancy

formation, however, at the Σ3 tilt GB is calculated to decrease the sliding threshold stress in low energy GBs [116].

The bond structure between two grains influences the creep resistance [96, 113]. During Σ13 $[1\bar{2}10]$ pyramidal twin GB sliding, breaking and re-bonding of the bonds at the boundary, especially the Al-O bonds, are found to be the controlling factor of this process [117]. In addition, for twin alumina grain boundaries, the Al-Al nearest neighbor pairs and the repulsion caused by short range anion packing is shown to dominate the interfacial energetics [110]. In RE containing GBs, REs are detected to form partially covalent transition metal-O bonds that are predicted to improve the creep resistance and GB strength for Σ3, Σ7 and Σ13 alumina GBs [96, 100, 102]. During these calculations, the main factor affecting the segregation energy is proposed to be the ionic radius of segregants [96, 100].

Chapter 2

Computational Methods

2.1 Introduction

Atomic-scale modeling creates an ideal laboratory environment and offers a way to investigate the dynamic behavior of systems that are currently impossible to explain using traditional experimental schemes. Computational methods are essential in investigating the microscopic nature of metal-ceramic interfaces, such as the $NiAl/Al_2O_3$ interface. A better understanding of a particular interface structure helps elucidate ways to optimize fabrication parameters in order to maximize thermal insulation and minimize spallation. Furthermore, calculating phonon frequencies and ground state energy by means of computational methods will help determining the effects of atomic and electrostatic interactions on diffusion coefficients and diffusion paths. By analyzing the influence of dopants on impurity diffusion, the crucial effects of dopants on the performance of the TBC can be determined.

In this thesis, electronic structure relaxations are conducted to calculate the energy of an interface or a system with a diffusing atom, using the *ab initio*: density functional theory as implemented by Vienna Ab initio Simulation Package (VASP) [118]. The transition state energies are found using the Nudged Elastic Band (NEB) method [119] and phonon frequencies are determined using the supercell method [120] as utilized in Alloy Theoretic Automated Toolkit (ATAT)[121].

2.2 Density Functional Theory

In quantum mechanics, information regarding material systems can be obtained by solving the Schrödinger equation of the many electron system. Solving a many-electron system is a mathematical challenge thus several approximations have been proposed to simplify it. These approximations can be categorized as: (i) methods based on the wave functions, which have led to the development of Hartree and Hartree-Fock approximations, (ii) methods utilizing the electron density as the main variable, which are initiated by Thomas-Fermi Model and led to development of DFT by Hohenberg and Kohn[122].

A single electron under the influence of a potential field, defined by the wave function $\psi(\mathbf{r})$, satisfies the time independent Schrödinger equation:

$$H\psi(\mathbf{r}) = \left(-\frac{\hbar^2}{2m}\nabla^2 + U(\mathbf{r})\right)\psi(\mathbf{r}) = \varepsilon\psi(\mathbf{r}), \tag{2.1}$$

For the case of a many body problem consisting of N interacting electrons under the influence of a potential defined by the wave function $\Psi = \Psi(\mathbf{r}_1, \mathbf{r}_2, \ldots, \mathbf{r}_N)$, the Schrödinger equation takes the form:

$$\langle \Psi | T + U + V | \Psi \rangle = E\Psi \tag{2.2}$$

where the first term is the kinetic energy operator, the second term represents the interaction of electrons with the nuclei at position $\mathbf{R}$, and the last term is the Coulomb energy caused by the electron-electron interactions:

$$T(\mathbf{r}) = \frac{-\hbar^2}{2m}\sum_i \nabla_i^2, \tag{2.3}$$

$$V(\mathbf{r}) = -Ze^2\sum_R \frac{1}{|\mathbf{r}_i - \mathbf{R}|}, \tag{2.4}$$

$$U(\mathbf{r}) = \frac{1}{2}\sum_{i\neq j}\frac{e^2}{|\mathbf{r}_i - \mathbf{r}_j|}. \tag{2.5}$$

Thus, Eq. 2.2 can be rewritten as:

$$\left(\sum_{i=1}^{N}\left(-\frac{\hbar^2}{2m}\nabla^2 - Ze^2\sum_R\frac{1}{|\mathbf{r}_i - \mathbf{R}|}\right) + \frac{1}{2}\sum_{i\neq j}\frac{e^2}{|\mathbf{r}_i - \mathbf{r}_j|}\right)\Psi(\mathbf{r}) = E\Psi(\mathbf{r}) \tag{2.6}$$

In order to simplify Eq. 2.6 and derive a one electron Schrödinger equation, one assumes a single electron moving under the influence of the potential energy created by other electrons. According to the Thomas-Fermi approximation, if other electrons are treated as a smooth distribution of negative charges with the electron charge density $n(\mathbf{r})$, Eq. 2.5, can be rewritten:

$$U(\mathbf{r}) \approx U_H[n] = -e\int d\mathbf{r}' n(\mathbf{r}')\frac{1}{|\mathbf{r} - \mathbf{r}'|} \tag{2.7}$$

where the electron density, in terms of the independent wave functions is given as:

$$n(\mathbf{r}) = -e\sum_i |\psi_i(\mathbf{r})|^2 \tag{2.8}$$

Hohenberg and Kohn[122] have developed two important theorems: (i) the ionic potential has one to one correspondence with the electron charge density n and (ii) only the correct density that satisfies the normalization condition:

$$-eN = \int n(\mathbf{r})d\mathbf{r} \tag{2.9}$$

minimizes the ground state energy. Hohenberg and Kohn have also defined a universal functional, $F[n]$ which only depends on the kinetic energy of the electrons and the

potential due to electron-electron interactions.

$$F[n] = \langle \Psi \left| (T + U) \right| \Psi \rangle \tag{2.10}$$

The universal functional does not have an exact expression since the energy due to the interaction of electrons cannot be derived analytically.

Using the Hartree approximation to express the N-electron wave function in terms of N one-electron wave functions:

$$\Psi(\mathbf{r}_1, \mathbf{r}_2, \ldots, \mathbf{r}_N) = \psi_1(\mathbf{r}_1)\psi_2(\mathbf{r}_2)\ldots\psi_N(\mathbf{r}_N) \tag{2.11}$$

and placing Eq.'s 2.7 - 2.11 into Eq. 2.6, the one-electron *Hartree Equations* are obtained:

$$-\frac{\hbar^2}{2m}\nabla^2\psi_i(\mathbf{r}) + V(\mathbf{r})\psi_i(\mathbf{r}) + \left[e^2 \sum_j \int d\mathbf{r}' \left|\psi_j(\mathbf{r}')\right|^2 \frac{1}{|\mathbf{r} - \mathbf{r}'|}\right] \psi_i(\mathbf{r}) = \varepsilon_i \psi_i(\mathbf{r}) \tag{2.12}$$

Within the Thomas-Fermi approximation, the electron-electron interactions are not taken into consideration and the kinetic energy is approximated as the kinetic energy of the non-interacting electrons $T_s[n]$.

$$T[n] \approx T_s[n] \tag{2.13}$$

As a result, the energy functional for a system of non-interacting electrons is given as:

$$E_s[n] = \langle \Psi_s[n] \left| \hat{T}_s + \hat{V}_s \right| \Psi_s[n] \rangle \tag{2.14}$$

where $\hat{V}_s = \hat{V} + \hat{U}_H + \hat{T} - T_s$ if $n_s(\mathbf{r}) = n(\mathbf{r})$.

Kohn and Sham[123] constructed a system using fictitious non-interacting electrons

with the same density as interacting electrons in order to satisfy the Pauli Principle and to include the correlation of electrons. They used single particle orbitals and introduced the exchange correlation energy $E_{xc}(\mathbf{r})$.

$$E[n] = \left\langle \Psi[n] \left| \hat{T} + \hat{U} + \hat{V} \right| \Psi[n] \right\rangle = \left\langle \Psi[n] \left| \hat{T}_s + \hat{U}_H + \hat{E}_{xc} + \hat{V} \right| \Psi[n] \right\rangle \tag{2.15}$$

where E_{xc} is composed of $(U - U_H)$ and $(T - T_s)$. For a non-interacting system the kinetic energy is the sum of the individual kinetic energies[124], $T_s[n]$, which can be written in terms of single-particle orbitals that are functionals of the electron density, n:

$$T_s[\{\phi(n)\}] = -\frac{\hbar^2}{2m} \sum_i^N \int d\mathbf{r} \phi_i^*(\mathbf{r}) \nabla^2 \phi_i(\mathbf{r}) \tag{2.16}$$

where the Kohn-Sham wave function is constructed using the single particle orbitals:

$$\Psi = \frac{1}{\sqrt{N!}} Det[\phi_1 \phi_2 \cdots \phi_N] \tag{2.17}$$

The ground state energy with respect to the electron density is minimum when its derivative with respect to $n(\mathbf{r})$ is zero.

$$\begin{aligned} 0 &= \frac{\partial E}{\partial n} \\ &= \frac{\partial T_s[n]}{\partial n(\mathbf{r})} + \frac{\partial V}{\partial n(\mathbf{r})} + \frac{\partial U_H}{\partial n(\mathbf{r})} + \frac{\partial E_{xc}}{\partial n(\mathbf{r})} \\ &= \frac{\partial T_s[n]}{\partial n(\mathbf{r})} + v(\mathbf{r}) + v_H(\mathbf{r}) + v_{xc}(\mathbf{r}) \end{aligned} \tag{2.18}$$

Similarly, for a system of non-interacting particles the derivative with respect to $n(\mathbf{r})$ is:

$$\frac{\partial E}{\partial n} = \frac{\partial T_s[n]}{\partial n(\mathbf{r})} + \frac{\partial V_s[n]}{\partial n(\mathbf{r})}$$

$$= \frac{\partial T_s[n]}{\partial n(\mathbf{r})} + v_s(\mathbf{r}) = 0 \tag{2.19}$$

These Eq.'s (Eq. 2.19 and Eq. 2.18) have the same solution, $n_s(\mathbf{r}) = n(\mathbf{r})$, if v_s is chosen to be:

$$v_s(\mathbf{r}) = v(\mathbf{r}) + v_H(\mathbf{r}) + v_{xc}(\mathbf{r}) \tag{2.20}$$

As a result, the electron density of an interacting system under the influence of a potential $v(\mathbf{r})$ can be calculated by solving the following Schrödinger equation of a system of non-interacting particles in a potential $v_s(\mathbf{r})$:

$$\left[\frac{-\hbar^2}{2m}\nabla^2 + v_s(\mathbf{r})\right]\phi_i(\mathbf{r}) = \epsilon_i\phi_i(\mathbf{r}) \tag{2.21}$$

A self-consistent approach is followed, to obtain the electron density. An initial guess of $n(r)$ is made to calculate V_s and Eq. 2.21 is solved for ϕ_i to obtain a new density $n(\mathbf{r})$. This iteration continues until the desired accuracy is obtained.

The *exchange-correlation* term is not explicitly known, thus different approximations are made to define E_{xc} in terms of the electron density. Local Density Approximation (LDA) and Generalized Gradient Approximation (GGA) are the most commonly used approximations.

2.2.1 Local Density Approximation (LDA)

LDA assumes that the exchange-correlation energy per electron $\varepsilon_{xc}(\mathbf{r})$ at any point r is equal to the exchange-correlation energy per electron in a uniform electron gas with the same density at point r[123]:

$$\varepsilon_{xc}[n(\mathbf{r})] = \varepsilon_{xc}^{hom}[n(\mathbf{r})] \tag{2.22}$$

giving

$$E_{xc}[n(\mathbf{r})] = \int \varepsilon_{xc}[n(\mathbf{r})]n(\mathbf{r})d\mathbf{r} = \int (\varepsilon_x[n(\mathbf{r})] + \varepsilon_c[n(\mathbf{r})])n(\mathbf{r})d\mathbf{r} \tag{2.23}$$

Here $\varepsilon_x[n(\mathbf{r})]$ and $\varepsilon_c[n(\mathbf{r})]$ are the exchange and correlation energies of a uniform electron gas with density $n(\mathbf{r})$ where the exchange correlation functional for a uniform electron gas is [125]:

$$E_{xc}^{LDA}[n(\mathbf{r})] = -\frac{3}{4}\left(\frac{3}{\pi}\right)^{1/3} \int n(\mathbf{r})^{4/3} d\mathbf{r} \tag{2.24}$$

The correlation functional does not have an explicit analytical expression, however approximate values are derived for various densities using Quantum Monte Carlo calculations[126]. LDA is successful in harmonic frequencies and equilibrium structure calculations, however it does not provide accurate binding energies. In order to suppress its over-binding effects various improvements have been proposed.

2.2.2 Generalized Gradient Approximation (GGA)

On top of its over binding problem, LDA fails when the density undergoes rapid changes. The GGA overcomes this problem and accounts for inhomogeneities by considering the gradient of the electron density[127]:

$$E_{xc} = E_{xc}^{GGA}[n(\mathbf{r}), \nabla n(\mathbf{r})] \tag{2.25}$$

which has the form[128]:

$$E_{xc}^{GGA} = \frac{3}{4}\left(\frac{3}{\pi}\right)^{1/3} \int n(\mathbf{r})^{4/3} F(\mathbf{s}) d\mathbf{r} \tag{2.26}$$

where the function $F(s)$ is:

$$F(\mathbf{s}) = \frac{1 + 0.19s\sinh^{-1}(7.79s) + (0.27 - 0.15e^{-100s^2})s^2}{1 + 0.19s\sinh^{-1}(7.79s) + 0.004s^4} \tag{2.27}$$

and a scale density gradient s is:

$$s = \frac{|\nabla n|}{2k_F n} \tag{2.28}$$

where $k_F = (3\pi^2 n)^{1/3}$ is the Fermi wave vector for a homogeneous electron gas with density n.

Compared to LDA, GGA gives better results for binding energy calculations. However there are some cases that GGA over-corrects the problems in LDA leading to under-binding[129, 130].

2.2.3 Pseudopotentials

Calculation of $v(\mathbf{r})$ by including all electron wave functions is an expensive and time consuming process [131]. The physical and chemical properties of materials are mostly determined by valence electrons. Thus in order to obtain a faster but still an accurate algorithm, the frozen core approximation is introduced in which only the effects from the valence electrons are taken into account and the effects of core electrons are replaced by a pseudopotential with a pseudo-wavefunction Ψ^{PS} [132]. According to its definition, this wavefuntion mimics the all electron wavefunction beyond the core radius while removing the nodes within the core region (Figure 2.1). Pseudopotentials reduce the cost by decreasing the number of Kohn-Sham equations to be solved but introduce the expense of creating the new pseudopotentials that requires large plane wave basis sets for transferability and norm-conserving properties.

Ultra-Soft Pseudopotentials

In order to avoid large basis sets, large cut-off radii leading to less accurate solutions are chosen. Non norm-conserving pseudopotentials were first introduced by Vanderbilt to avoid large basis sets [133]. Within his approximation, the pseudo wavefunctions

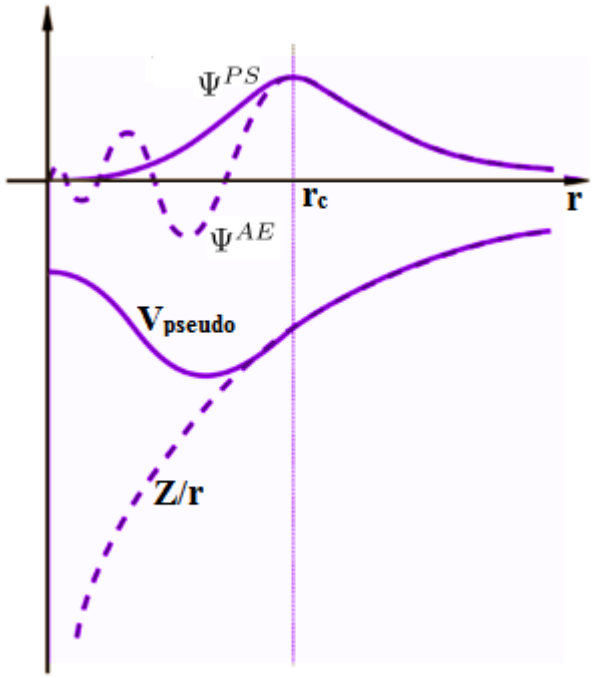

Figure 2.1: All electron and pseudo potential and wavefunction

are equal to the all electron wavefunctions outside the cutoff radius, whereas inside the cutoff radius they are as smooth as possible where localized augmentation charges are introduced to make up for the charge deficit caused by relaxing the norm-conserving constraints [132]:

$$\langle \Psi^{PS} | 1 + N^{PS} | \Psi^{PS} \rangle = \langle \Psi^{AE} | \Psi^{AE} \rangle. \tag{2.29}$$

Here Ψ^{AE} is the all-electron wavefunction and N^{PS} is the nonlocal charge augmentation operator. Using the pseudo-wavefunctions, the *ultrasoft pseudopotentials*(US-PP) and the charge density within US-PP approach become:

$$V_{US} = V_{loc}(\mathbf{r}) + \sum_{lm} D_{lm} |\beta_l\rangle\langle\beta_m| \tag{2.30}$$

$$n(\mathbf{r}) = \sum_i |\psi_i(\mathbf{r})|^2 + \sum_i \sum_{lm} \langle\psi_i|\beta_l\rangle Q_{lm}(\mathbf{r}) \langle\beta_m|\psi_i\rangle \tag{2.31}$$

where Q_{lm} are the augmentation charges that are defined by the charge difference between the all-electron and pseudo wave functions and $|\beta_l\rangle$ are the projectors.

Projected Augmented Wave Method

A similar approach, relaxing the norm-conserving constraint is introudced by Bloch in which a linear transformation connects the pseudo and all electron wave functions as [134]:

$$|\Psi^{AE}\rangle = T|\Psi^{PS}\rangle \tag{2.32}$$

where T is the transformation operator that leads to:

$$|\Psi^{AE}\rangle = |\Psi^{PS}\rangle + \sum_i (|\phi_i^{AE}\rangle - |\phi_i^{PS}\rangle)\langle\beta_i|\Psi^{PS}\rangle \tag{2.33}$$

$|\phi_i\rangle = |\phi_{lm\epsilon}\rangle$ are the partial waves and β_i are the projector functions. This way the all electron wavefunctions can be reconstructed from pseudo wavefunctions by subtracting the real oscillatory part close to an atom and replacing it by a pseudo function as represented schematically in Figure 2.2 [135–137]. Similarly, the electron density and the potential become a combination of three terms as:

$$n(\mathbf{r}) = n_{PS}(\mathbf{r}) - n_{PS}^l(\mathbf{r}) + n_{AE}^l(\mathbf{r}) \tag{2.34}$$

and

$$E = E_{PS} - E_{PS}^l + E_{AE}^l \tag{2.35}$$

where $n_{PS}(\mathbf{r})$ is the pseudo charge density, $n_{PS}^l(\mathbf{r})$ is the compensation charge and $n_{AE}^l(\mathbf{r})$ is the onsite all electron charge density.

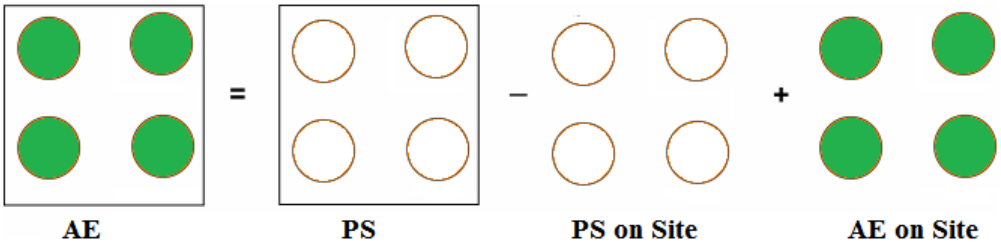

Figure 2.2: Schematic representation of PAW formalism

2.3 Nudged Elastic Band Method

Nudged Elastic Band (NEB) method is used for finding the minimum energy path (MEP) between the initial and final states of a transition[119]. The maximum energy along this path refers to the saddle point energy which determines the migration barrier for the diffusion process. A chain of *images* at the intermediate positions between the end point configurations of the diffusion path denoted by $[\mathbf{R}_0, \mathbf{R}_1, \cdots, \mathbf{R}_N]$, is created and all intermediate images are simultaneously optimized to obtain the MEP as shown in Figure 2.3a.

The NEB method incorporates strong aspects of the Locally Updated Planes (LUP) method [138] and the elastic band methods. In the LUP method, local tangents to the path connecting the images are introduced:

$$\hat{q}_i = \frac{\mathbf{R}_{i+1} - \mathbf{R}_{i-1}}{|\mathbf{R}_{i+1} - \mathbf{R}_{i-1}|} \tag{2.36}$$

and within the hyperplane with normal $\hat{q}_i$, the potential energy of each image is minimized:

$$\frac{\partial \mathbf{R}_i}{\partial t} = -\nabla V(\mathbf{R}_i)[1 - \hat{q}_i \hat{q}_i] \tag{2.37}$$

After every M steps of relaxation according to Eq. 2.37, new $\mathbf{R}_i$ values are obtained and used to recalculate the tangents, $\hat{q}_i$. Since the images are not connected, the LUP method ends up in an uneven distribution of images along the path that can cause a

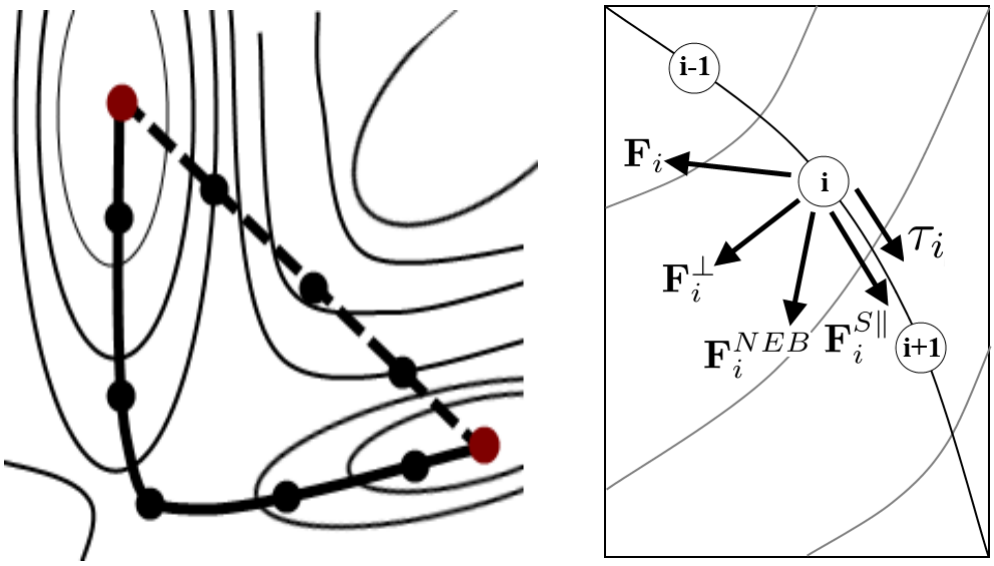

(a) (b)

Figure 2.3: (a) The dashed straight line is the interpolated image before relaxations. The straight line shows the MEP after convergence. (b) Forces that make up F^{NEB}; parallel spring force $F_i^{S\parallel}$ and the perpendicular component of the potential $F_i^{\perp}$. The tangent is defined along the path as the unit vector towards the higher energy neighboring image.

discontinuity in the case of two or more MEPs, between the end points[139]. In elastic band methods, the images are connected with springs, with spring constant k, and an object function is defined as:

$$S(\mathbf{R}_1, \cdots, \mathbf{R}_{N-1}) = \sum_{i=0}^{i=N} V(\mathbf{R}_i) + \sum_{i=1}^{N} \frac{k}{2}(\mathbf{R}_i - \mathbf{R}_{i-1})^2 \tag{2.38}$$

The object function is minimized with respect to the intermediate images while keeping the end points fixed. In LEPS potential[1], the total force on image i is the superposition of the true force, caused by the potential field, and the spring force[140]:

$$\mathbf{F}_i = -\mathbf{F}_i^T + \mathbf{F}_i^s \tag{2.39}$$

where the true force can be obtained by $\mathbf{F}_i^T = -\nabla V(\mathbf{R}_i)$ and the spring force $\mathbf{F}_i^s$ is

[1]London-Eyring-Polanyi-Sato(LEPS) Potential, an elastic band method

given as:

$$\mathbf{F}_i^s = k_{i+1}\left(\mathbf{R}_{i+1} - \mathbf{R}_i\right) - k_i\left(\mathbf{R}_i - \mathbf{R}_{i-1}\right) \tag{2.40}$$

The drawback of this method is that if the spring force is relatively small compared to the parallel component of the true force to the path, the images around the saddle point will shift towards the end points and if the spring force is chosen higher, the saddle point will be overestimated because of the perpendicular component of the spring force.

In the NEB method, different from Eq. 2.36, the local tangents are defined by:

$$\tau_i = \begin{cases} \tau_i^+ & \text{if } V_{i+1} > V_i > V_{i-1} \\ \tau_i^- & \text{if } V_{i+1} < V_i < V_{i-1} \end{cases} \tag{2.41}$$

where $\tau_i^+ = \mathbf{R}_{i+1} - \mathbf{R}_i$, $\tau_i^- = \mathbf{R}_i - \mathbf{R}_{i-1}$ and $V_i = V(\mathbf{R}_i)$ is the energy of image i [141]. If both of the adjacent images are lower or higher in energy than image i, the tangent is the weighted average of τ_i^+ and τ_i^-, where the weight is determined by the energy of adjacent images. If the energy of image i is greater or smaller than both the adjacent images; $V_{i+1} < V_i > V_{i-1}$ or $V_{i+1} > V_i < V_{i-1}$, then the minimum and the maximum energy differences are defined as:

$$\begin{aligned} \Delta V_i^{max} &= max\left(\left|V_{i+1} - V_i\right|, \left|V_{i-1} - V_i\right|\right) \\ \Delta V_i^{min} &= min\left(\left|V_{i+1} - V_i\right|, \left|V_{i-1} - V_i\right|\right) \end{aligned} \tag{2.42}$$

which can be used to obtain the new normalized tangent estimate $\hat{\tau}_i = \tau_i / \left|\tau_i\right|$ where

$$\tau_i = \begin{cases} \tau_i^+ \Delta V_i^{max} + \tau_i^- \Delta V_i^{min} & \text{if } V_{i+1} > V_{i-1} \\ \tau_i^+ \Delta V_i^{min} + \tau_i^- \Delta V_i^{max} & \text{if } V_{i+1} < V_{i-1} \end{cases} \tag{2.43}$$

Moreover, to overcome the problems encountered in LEPS, the perpendicular component of the spring force and the parallel component of the true force to tangent are

removed, and only the parallel component of the spring force and the perpendicular component of the true force to the tangent are applied on the images as shown in Figure 2.3b. Then, the total force acting on image i becomes:

$$\mathbf{F}_i^{NEB} = \mathbf{F}_i^{T\perp} + \mathbf{F}_i^{S\parallel} \tag{2.44}$$

where $F_i^{T\perp}$, the perpendicular component of the true force, and $F_i^{S\parallel}$, the parallel component of the spring force, are given as:

$$\mathbf{F}_i^{T\perp} = -\nabla V(\mathbf{R}_i) + \nabla V(\mathbf{R}_i) \cdot \hat{\tau}_i \hat{\tau}_i \tag{2.45}$$

$$\mathbf{F}_i^{S\parallel} = k\left(|\mathbf{R}_{i+1} - \mathbf{R}_i| - |\mathbf{R}_i - \mathbf{R}_{i-1}|\right)\hat{\tau}_i \tag{2.46}$$

Several modifications have been made to the NEB method to improve the accuracy of the MEP. Climbing Image Nudged Elastic Band (CINEB) is a modification to the NEB method, in which the image possessing the highest energy after several relaxations is forced to converge uphill to the saddle point[142]. The image is forced to maximize its energy along the band and to minimize it in all other directions. This is done by removing the spring force, $\mathbf{F}_i^s$, on this image and adding the inverted component of the true force parallel to the tangent, $-F_i^{T\parallel}$,:

$$\begin{aligned} \mathbf{F}_{imax}^{CINEB} &= \mathbf{F}_i^{T\perp} - \mathbf{F}_i^{T\parallel} \\ &= -\nabla V(\mathbf{R}_{imax}) + 2\nabla V(\mathbf{R}_{imax}) \cdot \hat{\tau}_{imax} \hat{\tau}_{imax} \end{aligned} \tag{2.47}$$

where *imax* refers to the image with the highest energy. In order to improve the resolution around the saddle point, variable spring constants are used. Lower spring constants are used to connect low energy images and stronger spring constants are used

around the saddle point by:

$$k_i = \begin{cases} k_{max} - \Delta k \left(\frac{E_{max} - E_i}{E_{max} - E_{ref}} \right) & \text{if } E_i > E_{ref} \\ k_{max} - \Delta k & \text{if } E_i < E_{ref} \end{cases} \tag{2.48}$$

where $E_i = max\{E_i, E_{i-1}\}$ is the higher energy of the two images connected by spring i, E_{max} is the maximum value of E_i for all the images and E_{ref} is a reference value for the energy[142].

2.4 Supercell Method

The Direct Supercell Method is utilized to calculate the phonon frequencies. It is based on the observation that the planar force constants can be expressed as a linear combination of the inter atomic force constants, where the planar force constants for a high symmetry direction can be determined using super cells[120]. With this method, not only harmonic but anharmonic effects can also be investigated.

A pair of atoms, positioned at unit cells associated with lattice vectors $\mathbf{R_i}$ and $\mathbf{R_j}$ (Figure 2.4), create a potential energy $\phi(\mathbf{R_i} - \mathbf{R_j})$[143]. If the atoms α and β are displaced by $u^{\alpha}(\mathbf{R_i})$ and $u^{\beta}(\mathbf{R_j})$, then the total potential energy of the crystal becomes:

$$U = \sum \phi(\mathbf{R_i} - \mathbf{R_j} + u(\mathbf{R_i}) - u(\mathbf{R_j})) \tag{2.49}$$

Expanding the total energy using the Taylor's approximation about the equilibrium position, and removing the higher-order terms, the potential energy within the harmonic approximation can be written as:

$$U = U^{eq} + U^{harm} \tag{2.50}$$

where U^{eq} is a constant representing the potential at equilibrium and U^{harm} is the harmonic potential due to displacements.

$$U^{harm} = \frac{1}{2} \sum_{\mathbf{R_i},\mathbf{R_j},\alpha,\beta} \mathbf{u}^{\alpha}(\mathbf{R_i}) \cdot \mathbf{C}^{\alpha\beta}(\mathbf{R_i} - \mathbf{R_j}) \cdot \mathbf{u}^{\beta}(\mathbf{R_j}) \tag{2.51}$$

$\mathbf{C}^{\alpha\beta}(\mathbf{R_i} - \mathbf{R_j})$ is the force constant matrix connecting atom α in the cell $\mathbf{R_i}$ and atom β in the cell $\mathbf{R_j}$.

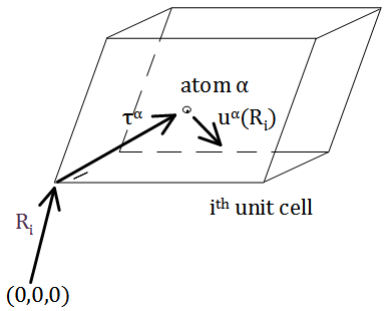

Figure 2.4: The vector R_i describes the position of the unit cell i with respect to the origin (0,0,0). τ^{α} is the position vector of atom α in the unit cell i and $u^{\alpha}(\mathbf{R}_i)$ is the vector representing the displacement of atom α from the equilibrium.

The equation of motion for this system can be written as:

$$M_{\alpha}\ddot{\mathbf{u}}^{\alpha}(\mathbf{R_i}) = -\sum_{\beta,\mathbf{R_j}} \mathbf{C}^{\alpha\beta}(\mathbf{R_i} - \mathbf{R_j})\mathbf{u}^{\beta}(\mathbf{R_j}) \tag{2.52}$$

where M_{α} is the mass of atom α. Using an ansatz to define the displacement $\mathbf{u}^{\alpha}$ in terms of a plane wave in momentum space:

$$\mathbf{u}^{\alpha}(\mathbf{R_i}) = \frac{1}{\sqrt{M_{\alpha}}}\mathbf{u}^{\alpha}(\mathbf{q})e^{i(\mathbf{qR_i}-\omega t)} \tag{2.53}$$

and substituting the second derivative of Eq. 2.53 into Eq. 2.52, the equation of motion

can be rewritten as:

$$-\omega^2 \mathbf{u}^{\alpha}(\mathbf{q}) + \sum_{\beta} \sum_{\mathbf{R}} \frac{1}{\sqrt{M_\alpha M_\beta}} \mathbf{C}^{\alpha\beta}(\mathbf{R}) e^{i\mathbf{q}\cdot(\mathbf{R}+\tau^{\alpha}-\tau^{\beta})} \mathbf{u}^{\beta}(\mathbf{q}) = 0 \tag{2.54}$$

where $\mathbf{R}$ is the vector connecting atom α in cell i to atom β in cell j and $\tau^{\alpha(\beta)}$ is the position vector of atom $\alpha(\beta)$ in the unit cell $i(j)$. Defining a *dynamical matrix*:

$$\mathbf{D}^{\alpha\beta}(\mathbf{q}) = \sum_{\mathbf{R}} \frac{1}{\sqrt{M_\alpha M_\beta}} \mathbf{C}^{\alpha\beta}(\mathbf{R}) e^{i\mathbf{q}\cdot(\mathbf{R}+\tau^{\alpha}-\tau^{\beta})} \tag{2.55}$$

Eq. 2.54 can be rewritten in terms of the dynamical matrix as:

$$-\omega^2 \mathbf{u}^{\alpha}(\mathbf{q}) + \sum_{\beta} \mathbf{D}^{\alpha\beta}(\mathbf{q}) \mathbf{u}^{\beta}(\mathbf{q}) = 0 \tag{2.56}$$

The one dimensional planar force constants along high symmetry directions, $\lambda^{\alpha\beta}(n)$, can be calculated from the Hellmann-Feynman forces [144]. The force on atom α in the n^{th} layer due to the collective displacement of β atoms in the m^{th} layer can be given with respect to the one dimensional planar force constants as:

$$F^{\alpha}(n) = -\sum_{m,\beta} \lambda^{\alpha\beta}(n-m) \cdot \mathbf{u}^{\beta}(m) \tag{2.57}$$

After calculating the force constants for both longitudinal and transverse displacements using Eq. 2.57, which are the projections of planar force constants in the polarization directions, the planar force constants can be found by unitary transformations[120]. The planar force constant $\lambda^{\alpha\beta}(n)$ acting on the displaced layer d_n away can be expressed as the sum of force constants:

$$\lambda^{\alpha\beta}(n) = \sum_{\mathbf{R}, \hat{\mathbf{e}}\cdot(\mathbf{R}+\tau^{\alpha}-\tau^{\beta})=d_n} \mathbf{C}^{\alpha\beta}(\mathbf{R}) \tag{2.58}$$

where $\hat{\mathbf{e}}$ is the unit vector normal to the atomic layer. Solving Eq. 2.58, the force constant matrix and thus the dynamical matrix can be obtained. Finally, if $Det\{\mathbf{D}^{\alpha\beta}(\mathbf{q}) - \omega^2\mathbf{I}\} = 0$, the phonon frequencies can be found by solving for the eigenvalues of the dynamical matrix in Eq. 2.56.

2.5 Electron Localization Function

In order to examine the potential correlation between the electronic structures and adhesion, diffusion or grain boundary strengthening phenomena, the electronic density of states (DOS) and the electron localization function (ELF) are calculated. ELF amplifies the bonding features and allows one to analyze the electron distribution on an absolute scale. The ELF is defined and calculated as:

$$ELF = \frac{1}{1 + \left(\frac{D(\overrightarrow{r})}{D_h(\overrightarrow{r})}\right)^2} \tag{2.59}$$

with

$$D\left(\overrightarrow{r}\right) = \frac{1}{2}\nabla_{\overrightarrow{r}}\nabla_{\overrightarrow{r}'}\rho\left(\overrightarrow{r}, \overrightarrow{r}'\right)\Big|_{\overrightarrow{r}=\overrightarrow{r}'} - \frac{1}{8}\frac{\left|\nabla n\left(\overrightarrow{r}\right)\right|^2}{n\left(\overrightarrow{r}\right)} \tag{2.60}$$

and

$$D_h\left(\overrightarrow{r}\right) = \frac{3}{10}\left(3\pi^2\right)^{\frac{2}{3}} n(\overrightarrow{r})^{\frac{5}{3}} \tag{2.61}$$

where ρ is the first order reduced density matrix, $D(\overrightarrow{r})$ is the von Weizscker kinetic energy functional corresponding to the ground state kinetic energy density of a non-interacting system at density $n\left(\overrightarrow{r}\right)$, and $D_h\left(\overrightarrow{r}\right)$ is the kinetic energy density of a uniform electron gas with a spin density equal to the local value of $n\left(\overrightarrow{r}\right)$. ELF values are closer to 1 for high electron localization, and 1/2 for the regions with a valence charge distribution similar to the homogeneous electron gas [145].

Chapter 3

Theoretical Methodology

3.1 Work of Adhesion

The characteristics of interface and bonding properties can be described by the work of adhesion W_{ad}. The work of adhesion is defined as the energy per unit area, needed to separate/pull the system apart to its constituents. The work of adhesion is defined as:

$$W_{ad} = \frac{E_{BC} + E_{TGO} - E_{BC/TGO}}{A} \tag{3.1}$$

where E_{BC}, E_{TGO} and $E_{BC/TGO}$ are the total energies of the bond coat, TGO and the interface, respectively. Previously, using *ab initio* calculations, the work of adhesion of Al_2O_3/NiAl interface is calculated as 2.82 Jm^{-2} or 0.661 Jm^{-2} by various authors [17, 47]. The difference between results can stem from the difference in the way the models are created and the machines used for calculations. Thus, instead of a quantitative analysis, it is best to conduct a qualitative comparison between studies.

3.2 Diffusion Theory

Diffusion is a result of the constant thermal motion of atoms, molecules, and particles, which causes atoms to move from areas of high to low concentration. Fick's laws of

diffusion provide the necessary equations to find the diffusion coefficient, D.

3.2.1 Fick's Laws of Diffusion

In a three dimensional system, considering a flux of diffusing particles with a concentration c(x_i,x_j,x_k,t), Fick's first law in a three dimensional, isotropic medium is given by:

$$J = -D\nabla c \tag{3.2}$$

Eq. 3.2 suggests that, in the presence of a concentration gradient $\frac{\partial c}{\partial x}$, a flux density (number of atoms/moles traversing unit area per unit time), J, in the opposite direction is established and a diffusion process begins in order to balance the concentration [146]. When the flux varies with time, i.e. for the time dependent case, the *equation of continuity* for diffusion becomes:

$$\frac{\partial J}{\partial x} = -\frac{\partial c}{\partial t} \tag{3.3}$$

where the number of diffusing particles are conserved. And finally, substituting Eq. 3.2 into Eq. 3.3, Fick's second law is obtained as:

$$\frac{\partial c}{\partial t} = \frac{D\partial^2 c}{\partial x^2} \tag{3.4}$$

in which, D is called as the diffusion coefficient and has the dimensions of m^2s^{-1}.

When the system is not isotropic, physical and chemical properties depend on the direction. Thus in an anisotropic media, the diffusivity term becomes a symmetric tensor and for each direction, a unique diffusion coefficient is used.

$$D = \begin{pmatrix} D_1 & 0 & 0 \\ 0 & D_2 & 0 \\ 0 & 0 & D_3 \end{pmatrix} \tag{3.5}$$

where D_1, D_2 and D_3 are called the *principal diffusion coefficients*.

The diffusion coefficient can be expressed in terms of the principal diffusion coefficients for an arbitrary direction in an anisotropic medium (Figure 3.1),. If the angles θ_1, θ_2, θ_3 with respect to the principal axes are given, the diffusion coefficient for an arbitrary direction becomes [147]:

$$D = cos\theta_1^2 D_1 + cos\theta_2^2 D_2 + cos\theta_3^2 D_3 \tag{3.6}$$

For uniaxial crystal systems that has a crystal axis different from the other two axes, $D_1 = D_2 \neq D_3$, the diffusion coefficient reduces to:

$$D = D_1 \sin^2\Theta + D_3 \cos^2\Theta \tag{3.7}$$

where Θ is the angle between the crystal axis and the diffusion direction. As for cubic materials, the diffusion is the same in all axes and the diffusion coefficient is a scalar quantity: $D_1 = D_2 = D_3 = D$.

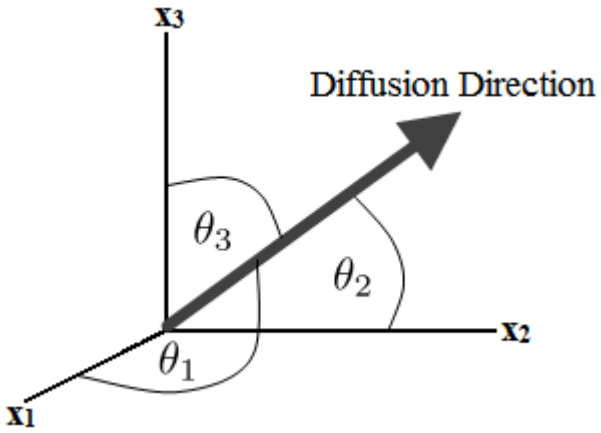

Figure 3.1: Diffusion direction in a single-crystal with principal diffusion axes x_1, x_2, x_3

3.2.2 Atomic Theory and Jump Processes

Diffusion occurs by individual jumps of atoms within bulk materials, along dislocations, grain boundaries and interfaces or at surfaces. For a bulk material, in which all jumps are well defined, there are eight possible diffusion mechanisms [148]: ring, exchange, interstitial, interstitialcy, crowdion, vacancy, divacancy, and relaxation; from which the most frequently encountered mechanisms are vacancy, divacancy and interstitial.

In most solids, diffusion of a tracer or an impurity atom is mainly vacancy mediated. If there is a vacant lattice site in the structure, one of its neighboring atoms jump onto that site, leaving its initial site vacant. The successive jumps that an atom makes are not independent from each other. After the atom jumps to a vacant site, its next jump depends on the probability of having a vacancy at a non-random nearest neighbor site [149]. The vacancy concentration increases with increasing temperature and leads to divacancy formation. For loosely packed crystal structures, the interstitial mechanism is preferred. The interstitial atom, which is usually smaller in size compared to the host atoms, makes uncorrelated jumps from one interstitial site to another.

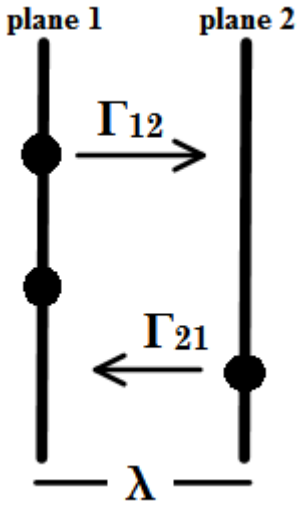

Figure 3.2: Diffusion planes

Considering a unidirectional diffusion of atoms between planes 1 and 2 with inter-

planar spacing λ as in Figure 3.2, the net flux from plane 1 to 2 is given as:

$$J = j_{12} - j_{21} = n_1\Gamma_{12} - n_2\Gamma_{21} \tag{3.8}$$

where Γ_{ij} is the jump frequency from plane i to plane j and n_i is the number of diffusing atoms per unit area on plane i. Relating n_1 and n_2 to volume concentrations of diffusing atoms and applying the Taylor expansion, the net flux can be rewritten in terms of the concentration gradient as:

$$J = -\lambda^2\Gamma\frac{\partial c}{\partial x}. \tag{3.9}$$

Substituting Eq. 3.9 into Eq. 3.2, the diffusion coefficient is obtained as,

$$D = \lambda^2\Gamma. \tag{3.10}$$

Atoms make a completely random walk when there is no correlation between successive jumps. In an isotropic medium, where displacement in each direction is the same; i.e. X=Y=Z=R, Einstein's random walk equation can be applied as [146]:

$$D = \frac{\langle X^2\rangle}{2t} + \frac{\langle Y^2\rangle}{2t} + \frac{\langle Z^2\rangle}{2t} = \frac{\langle R^2\rangle}{6t} \tag{3.11}$$

The jump frequency, Γ, is defined as the average number of jumps, $\langle n\rangle$, in time t. Expressing $\langle R^2\rangle = \langle n\rangle d^2$, where d is jump length, the diffusion coefficient can be rewritten as:

$$D = \frac{1}{6}\Gamma d^2, \tag{3.12}$$

where the total jump frequency, Γ, depends on the probability of vacancy formation at a site near the diffusing atom, CZ, and the probability of a successful jump, v:

$$\Gamma = CZv \tag{3.13}$$

Here C is the concentration of vacancies adjacent to the tracer atom, Z is the coordination number and v is the atom jump frequency [150].

Examples

Body Centered Cubic (BCC)-Based Structure: For a BCC structure, the coordination number Z is 8 while the distance between two nearest neighbors is $d = (a\sqrt{3})/2$ where a is the unit cell length. Substituting Z and d into Eq. 3.12, the diffusion coefficient for a BCC structure is obtained as:

$$D = \frac{1}{6} Cv8 \frac{3a^2}{4} = Cva^2 \tag{3.14}$$

Hexagonal Closed Packed (HCP)-Based Structure: Anisotropy often appears in non-cubic single crystals, and materials. For such uniaxial materials, with their unique axis parallel to x_3-axis: $D_1 = D_2 \neq D_3$, the diffusion coefficient is expressed as in Eq. 3.7., thus two different jump frequencies are necessary for hexagonal structures: Γ_1 for basal plane jumps, and Γ_2 for out of basal plane jumps [146]. There are six in-plane and six out-of-plane jumps on the x-y surface, so for a HCP structure the diffusivity on the x-y plane becomes:

$$D_x = \frac{1}{2}\left[2\Gamma_1 a^2 + 4\Gamma_1 \frac{a^2}{4} + 4\Gamma_2 \frac{a^2}{4} + 2\Gamma_2 .0\right] \tag{3.15}$$

Along the z-axis there are only 6 jumps leading to a diffusion equation:

$$D_z = \frac{1}{2}\Gamma_2 6 \frac{c^2}{4} = \frac{3}{4}\Gamma_2 c^2 \tag{3.16}$$

where c is the unit cell length along z-axis.

Formation

A vacancy is formed when an atom from the bulk structure moves to the surface, leaving its initial position vacant. The energy needed to generate that vacancy is known as the formation energy, ΔG_F and is defined as the energy difference between the systems with and without a defect [55, 84]:

$$\Delta G_F = \frac{\Delta E_d^f - \frac{N_d}{N}\Delta E_{AB}^f}{|N - N_d|} \tag{3.17}$$

For an alloy containing x A and y B atoms, ΔE_d^f and ΔE_{AB}^f are the formation energies of the alloy system with and without a defect, respectively. N is the total number of atoms in the ideal structure and N_d is the total number of atoms in the defective supercell. The formation energy of a perfect structure, ΔE_{AB}, is given as:

$$\Delta E_{A_xB_y}^f = E\left(A_xB_y\right) - xE\left(A\right) - yE\left(B\right) \tag{3.18}$$

where E(A) and E(B) are the energies of the pure A and B atoms. Similarly, the formation energy of an alloy containing an additive, D, or an interstitial, Z, is calculated as:

$$\Delta E_{A_{x-1}B_yD}^F = E_{A_{x-1}B_yD} - (x-1)E(A) - yE(B) - E(D) \tag{3.19}$$

$$\Delta E_{A_xB_y+Z}^F = E_{A_xB_y+Z} - xE\left(A\right) - yE\left(B\right) - E(Z) \tag{3.20}$$

When there is a vacancy in the structure substituting an A atom, the defect formation energy, ΔE_d^f, is expressed as:

$$\Delta E_{A_{x-1}B_y}^f = E_{A_{x-1}B_y} - (x-1)E\left(A\right) - yE\left(B\right) \tag{3.21}$$

If there are two or more different types of defects present in the alloy, instead of summing up the individual formation energies, the steps given above are followed for the alloy with the *defect cluster*; the formation energy of the alloy with the defect cluster is calculated and substituted as ΔE_d^f in Eq. 3.17. By this way, the binding energy between defects is taken into account. The vacancy concentration, C, also depends on the vacancy formation energy as:

$$C = \exp\left(-\frac{\Delta G_F}{k_B T}\right) \tag{3.22}$$

where k_B is the boltzmann constant.

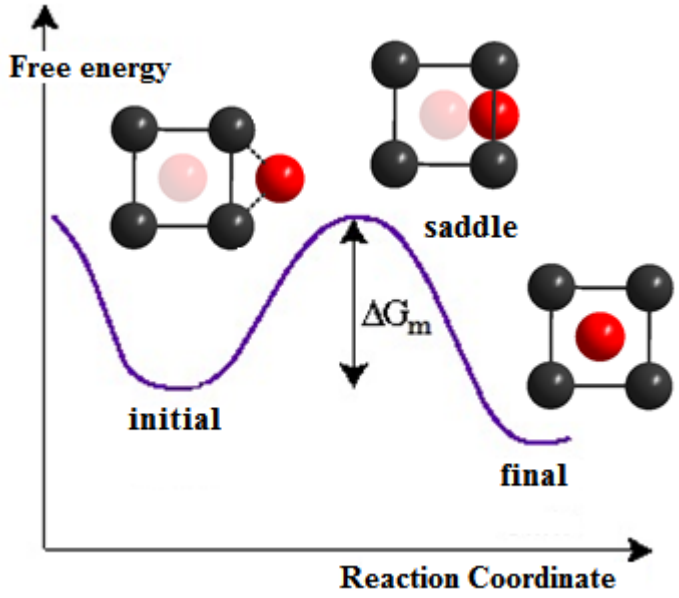

Figure 3.3: Atom Diffusion path

Migration

An atom has to have the migration energy ΔG_m to pass through the energy barrier while diffusing from an initial to a final position (Figure 3.3). The jumping frequency

depends on this migration energy and is given as:

$$v = \tilde{v}\exp\left(-\frac{\Delta G_m}{k_B T}\right) \tag{3.23}$$

where $\tilde{v}$ is the vibrational frequency in the direction of diffusion. Treating migration as a many-body problem, Vineyard derived an expression for the migration pre-factor $\tilde{v}$ [151]. For a system with N atoms and 3N-dimensional configuration space, the vibrational frequency is defined as:

$$\tilde{v} = \frac{\sum_i^{3N-3} w_i^{initial}}{\sum_i^{3N-4} w_i^{saddle}} e^{-\frac{\Delta S_M}{k_B}} \tag{3.24}$$

where w_i is the normal vibrational frequencies and ΔS_M is the migration entropy. The denominator of the jump frequency contains one less vibrational frequency at the saddle point since one vibrational degree of freedom is converted into a translational degree of freedom due to the motion along the reaction path [87]. The entropy term in pre-factor $\tilde{v}$ can be ignored, when the diffusing atom does not cause large distortions as at 0 K. With increasing temperature, however, the diffusing atom causes large distortions, which makes it unrealistic to ignore the entropy. Thus it can be approximated as the vibrational entropy difference between the stable and the saddle points which is calculated by the harmonic transition state theory. Considering only phonon contributions to the energy within the high temperature limit, $hw/k_B T \ll 1$, the vibrational entropy of a series of harmonic oscillators containing N atoms is calculated as:

$$S^{vib} = -k_B \sum_i^{3N-3} \ln\left(\frac{hw_i}{k_B T}\right) + 3Nk_B, \tag{3.25}$$

where, w_i are normal vibrational frequencies, h is the Plank constant and T is the reference temperature.

Correlation

In reality, some diffusion mechanisms possess correlated jumps. When jumps are correlated, the atom has a higher probability of tracing its path back. To express this correlation properly, a correlation factor, f, for each structure must be added to the diffusion equation.

$$D = f\frac{1}{6}\Gamma d^2 \tag{3.26}$$

The correlation factor f=1 for direct interstitial diffusion, where there is no interaction between the diffusing atom and its surroundings. However if there exists an interaction such that some specific sites are forbidden for the diffusing atom, the correlation factor is f<1. The latter is true for vehicle assisted diffusions and for some interstitial diffusions in which the successive jumps are not independent from each other. The correlation factor f for correlated jumps is given by:

$$f = \frac{1 + \langle cos\theta \rangle}{1 - \langle cos\theta \rangle}, \tag{3.27}$$

where θ is the angle between two successive jumps. The correlation factor can also be expressed as the ratio of the actual diffusivity of a tagged atom, D^*, and a hypothetical uncorrelated diffusivity, D_{random}; $f = \frac{D^*}{D_{random}}$. Finally, combining the above equations the overall diffusion coefficient is expressed as:

$$D = D_0 e^{-\frac{Q}{k_B T}}, \tag{3.28}$$

where the pre-exponential term is $D_0 = f\frac{1}{6}Z\tilde{\nu}d^2$ and $Q = \Delta G_M + \Delta G_F$ is called the activation energy.

3.2.3 Diffusion in Alloys

For alloys in the form of AB, the Γ of the vacancy depends on the nature of the atom with which it exchanges. There are two different jump frequencies Γ_A and Γ_B for alloys. In the case of non-homogeneous dilute alloys, the self-diffusion coefficient of the solvent atom varies with the solute concentration, N_B, as [146]:

$$D_{A*}^{AB} = D_{A*}^{A}[1 + b_1 N_B + b_2 N_B^2 \ldots] \tag{3.29}$$

while the diffusion coefficient for the solute atoms can be calculated as:

$$D_{B*}^{AB} = D_{B*}^{A} \tag{3.30}$$

In homogeneous ordered alloys, the formation of a vacancy destroys the order and forms anti-site defects A_B and B_A. High formation energy of these defects suggests complicated diffusion mechanisms.

For B2-CsCl type alloys, in general, vacancy-type defects mediate the diffusion. The B2 structure consists of two primitive cubic sublattices. In the completely ordered state of a stoichiometric B2 compound, A atoms occupy one sublattice while B atoms occupy the other [147]. If the ordering energy of AB compound is very high, sublattice diffusion of each component via the second nearest-neighbor jumps is conceivable. The most discussed diffusion mechanisms for B2 structure are the next nearest neighbour (NNN) vacancy jumps, the six jump vacancy cycles (6JC's), the antistructural bridge mechanism (ASB) and the triple defect mechanism (TD). However when the size of the diffusing atom is small compared to host atoms, interstitial mechanism is also preferred for diffusion.

Next Nearest Neighbour Vacancy Jumps (NNN): The NNN mechanism is the simplest mechanism for a vacancy to move from one site to another in the same

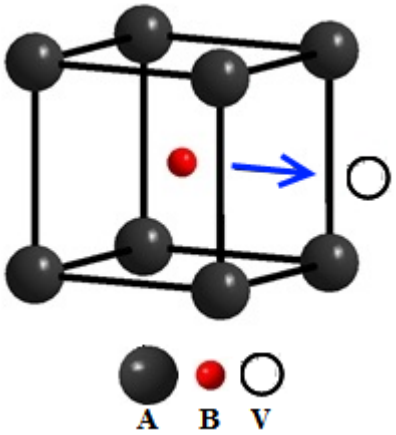

Figure 3.4: Next nearest neighbour diffusion

sublattice. As shown in Figure 3.4, it requires the formation of a vacancy, and it only consists of NNN jumps. The saddle point occurs when the tracer atom (A) passes through the plane consisting of four B atoms.

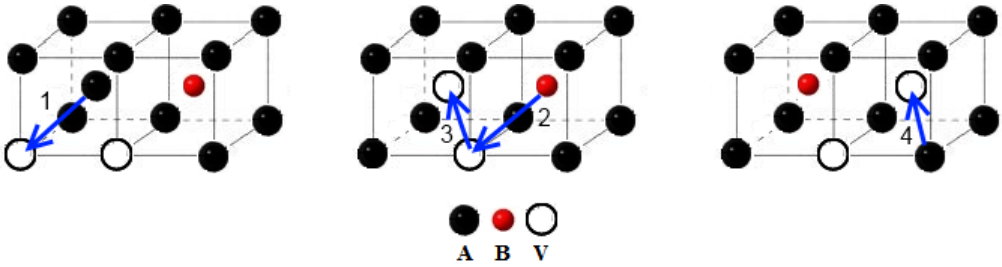

Figure 3.5: Triple defect diffusion

Triple Defect Mechanism (TD): In the TD mechanism, proposed by Stolwijk *et. al.* [149] for B2 type intermetallic compounds, there are four NN jumps starting with a Triple-defect cluster composed of 2 vacancies and 1 anti-site as seen in Figure 3.5. The following reaction is followed during a Triple-defect mechanism:

$$V_A + V_B \rightleftharpoons 2V_A + A_B \tag{3.31}$$

As seen from Eq. 3.31, instead of forming equal numbers of vacancies on both sublattices, two vacancies on one sublattice and an anti-site atom on the other sublattice

appears. According to this equation, Triple-defect formation is favored in inter-metallics with high formation enthalpies of V_B vacancies.

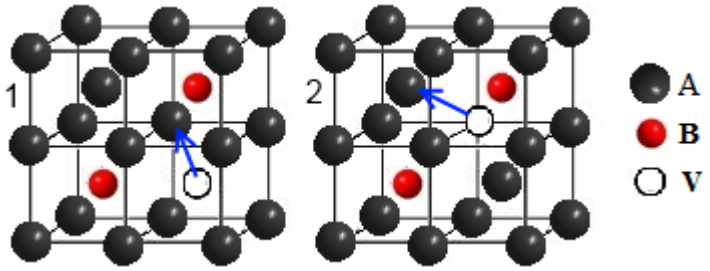

Figure 3.6: Antistructural Bridge Mechanism

Antistructural Bridge Mechanism (ASB): ASB mechanism that is first proposed by Kao and Chang [152] and later studied by Belova and Murch [153], requires a sufficient concentration of anti-site atoms. Such a deviation from the stoichiometric composition and increase in disorder is mainly observed at high temperatures. As shown in Figure 3.6, in two NN jumps the vacancy and the antisite atom exchange their positions [147].

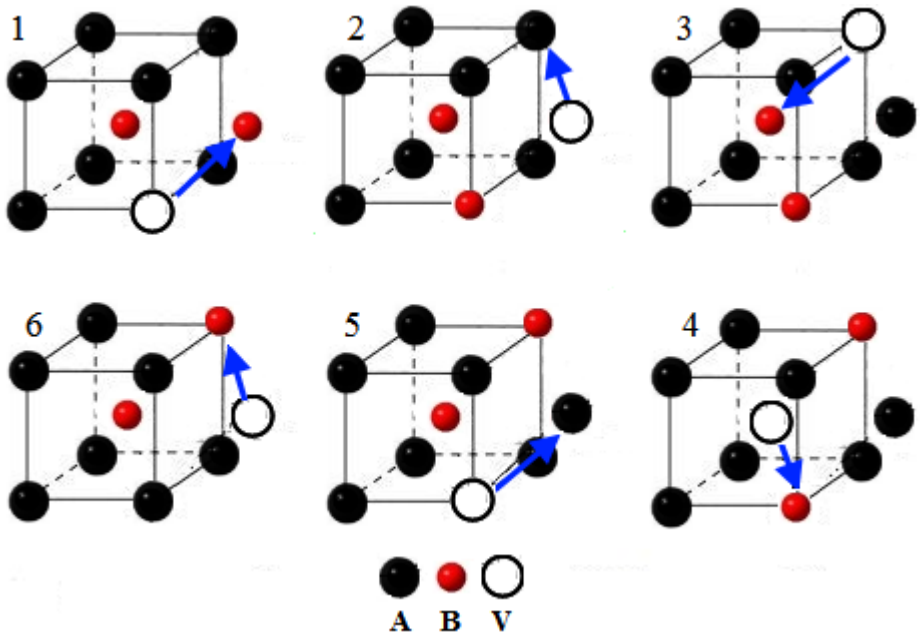

Figure 3.7: Six Jump Cycle

Six Jump Cycle (6JC): The 6JC is a mono-vacancy mediated diffusion. The cycle

forms from six successive jumps between nearest neighbour sites for the displacement of a vacancy between the two sublattices. In the end of the cycle the order is re-established. Figure 3.7 shows a 6 jump cycle. Due to high formation energies, there are correlations in this kind of mechanism. Elcock and McCombie [154] showed:

$$\frac{D_{A*}}{D_{B*}} = \frac{[V_\alpha]\, w_6^\alpha + 2\,[V_\beta]\, w_6^\beta}{2\,[V_\alpha]\, w_6^\alpha + [V_\beta]\, w_6^\beta} \tag{3.32}$$

where $[V_i]$ is the mole fraction of vacancies on the i^{th} sublattice and ${w_6}^i$ is the frequency of completion of a cycle beginning and ending on an i^{th} sublattice site. Since both atoms participate in the cycle the diffusivities of both components cannot be very different [147]. In a highly ordered state, the ratio of the diffusivities, D_A/D_B, lies within the limit: 1/2.034 ¡D_{A*}/D_{B*}¡2.034.

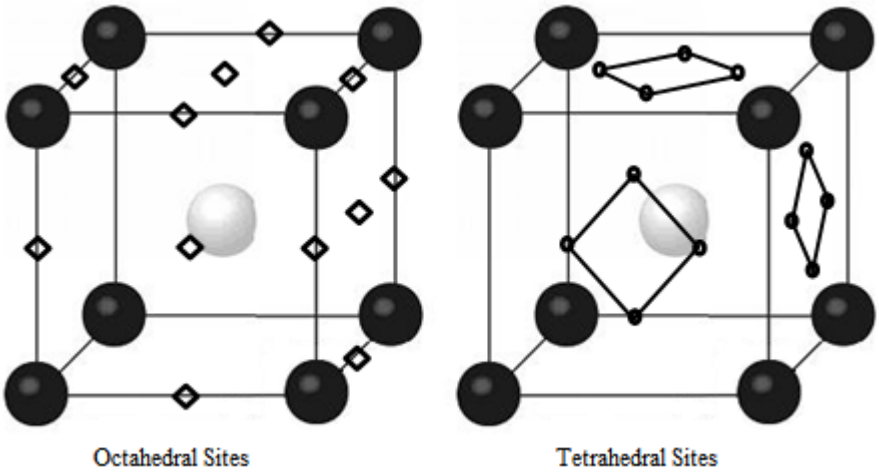

Figure 3.8: Interstitial sites: a)octahedral b)tetrahedral

Interstititial Diffusion: In a B2 structure, there are two different sites that an interstitial atom can occupy, tetrahedral and octahedral as shown in Figure 3.8. Depending on the formation energy, the atom chooses one of the two possible sites. For interstitial diffusion, since the tracer atom diffuses from one interstitial site to another, there is no need for formation of a vacancy.

3.3 Fracture Toughness

Stress is defined as the force per unit area, and when a force is applied to a material, it is said to be in a state of stress. In crystals, stresses depend on the direction and are expressed by a stress tensor σ_{ij}. The distortions of the crystal are proportional to the applied stress and the material returns to its ideal state once the applied stresses are removed, provided that the material is subjected to stresses below the elastic limit. Elastic limit defines the maximum stress that can be applied to a material without causing irreversible deformation. Above the elastic limit, the material becomes elastically unstable and undergoes plastic deformation. The stress value at this onset is called the ideal strength. Compared to brittle materials that fail at early stages of irreversible deformations, ductile materials can undergo large plastic deformations [155].

Fracture toughness is an intrinsic property of a material describing the ability to resist fracture when there is a pre-existing flaw such as a crack or a void. It is one of the most important characteristics of a material used in component design since low fracture toughness values can cause deformation and failure when materials are subjected to high stress. The three different types of fracture mechanisms, called mode I, II and III are shown in Figure 3.9 from which the most commonly studied ones are I and II. Mode I is the tensile opening in which a tensile stress is applied normal to the crack plane and Mode II is the sliding mode where a shear stress is applied parallel to the crack plane. In order to explain the failure and relate the applied stress to the fracture toughness of materials, different methods are introduced.

Up to a critical crack length, the crack will grow only if a stress is applied to the system. However, after the crack reaches a critical length (that is: the available energy for crack extension is greater than or equal to work required for crack growth) the failure starts and the crack grows spontaneously. Griffith proposed [156] the energy balance approach to calculate the stress and fracture toughness. The strain energy

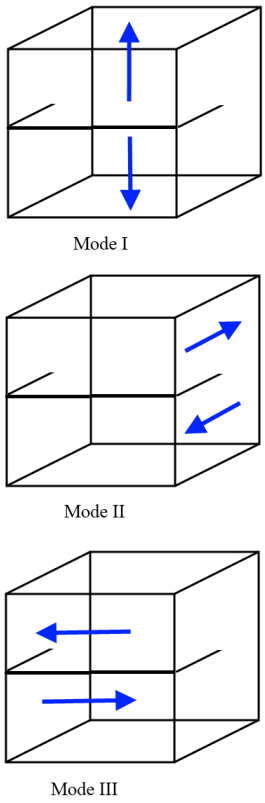

Figure 3.9: Stress modes

released per unit thickness as the crack grows in terms of the crack length a is given as:

$$G = -\frac{\sigma^2}{2E}\pi a^2 \tag{3.33}$$

where E is the Young's Modulus. While forming a crack, the energy absorbed by the material is the energy released during the breaking of the bonds [157]. If the energy release rate is above a critical value (G_c) a spontaneous crack growth will initiate. Griffith [156] equated G_c to the total surface energy S:

$$S = 2\gamma_s a \tag{3.34}$$

The factor 2 represents the two surfaces created by the crack and γ_s is the surface

energy. Thus spontaneous crack growth will start when:

$$2\gamma_s - \frac{\sigma_f^2}{E}\pi a = 0 \tag{3.35}$$

and the critical stress is derived from Eq. 3.35 as:

$$\sigma_f = \sqrt{\frac{2E\gamma_s}{\pi a}} \tag{3.36}$$

However, because Griffith worked with very brittle materials, his approach failed in obtaining the critical stress values for ductile materials. Irwin and Orowan [158, 159] proposed that for ductile materials, during crack formation, the vast majority of the released strain energy is consumed by plastic flow at the crack tip instead of forming new surfaces as in brittle materials. Thus the concept of surface energy alone is not enough to provide an accurate model for ductile materials and the energy required for crack growth is much larger than the surface energy. To include the plastic deformations, Irwin and Orowan modified the critical strain energy release rate, G_C:

$$G_c = \gamma_s + \gamma_p \tag{3.37}$$

where γ_p is the plastic work per unit area as defined by Irwin [158]. Using the newly defined critical strain energy release rate, the critical stress can be rewritten as:

$$\sigma_f = \sqrt{\frac{EG_c}{\pi a}} \tag{3.38}$$

For mode II, sliding, the shear stress as a function of the shear displacement is obtained from the first derivative of the total energy versus the shear displacement, x. However several different approaches have been proposed within the DFT framework for modeling mode I, cleavage type of cracks. The ideal brittle cleavage decohesion is

modeled by rigidly separating the two planes of a crystal to obtain the change in the total energy of the system with respect to the separation distance. The DFT results are then fit into the universal binding energy relation (UBER) that includes the non-linear changes in structure during cleavage decohesion as:

$$E\left(x\right) = -G_c\left[\left(1+\frac{x}{l}\right)\exp\left(-\frac{x}{l}\right)-1\right] \tag{3.39}$$

where x is the applied separation and l is the critical separation distance. The critical cleavage stress is obtained by calculating $dE(x)/dx$ at the critical opening distance, l,:

$$\sigma_c = \frac{G_c}{el}. \tag{3.40}$$

Here G_c and l depend on the orientation of the cleavage plane, and σ_c is the maximum tensile stress perpendicular to the cleavage plane. Within ideal brittle cleavage using UBER, the positions of the atoms are kept fixed throughout calculation and as $x \to \infty$, it may converges to zero energy with a negative curvature which is not realistic for all materials.

The UBER relation is not applicable to the relaxed cleavage where the atoms are allowed to relax during calculations after applying a rigid separation between the planes. By introducing relaxations, the structure is expected to heal as long as the applied separation is smaller than the critical limit. Above this critical separation, the bonds holding the two planes will break, the crack remains open and the atoms adjacent to the crack relax to form structurally relaxed surfaces. Thus Lazar [160] derived a cohesion relation for relaxed structures. The author combined two approaches in his ideal elastic cleavage relation by introducing a critical opening (l_C) as in UBER, and assuming elastic relaxations up to a critical opening as in Nguyen and Ortiz approach. By taking the second order term in the Taylor expansion of UBER, the total energy

for $x \leq l_C$ is derived as:

$$E(x) = \frac{G_c x^2}{{l_C}^2} \tag{3.41}$$

For crack sizes $x \geq l_C$ they set the total energy as $E(x) = G_c$ and finally calculate the critical stress from the first derivative of the total energy $\sigma_c = dE(x)/dx$ at $x = l_c$ as:

$$\sigma_c = \frac{2G_c}{l_c} \tag{3.42}$$

Thus, by introducing a critical opening below which a material can heal by elastic relaxations, they derive a convenient way to calculate the critical stress independent of the number of planes, N. A simpler approach is also applied by Kang *et. al.* [161]. Instead of fitting an equation to the energy vs. separation, similar to mode II cracks, the stress as a function of the opening is obtained from the first derivative of the total energy vs. the cleavage opening, x.

Several approaches have been introduced to elucidate the mechanical behavior of materials: a ductility condition is defined using the shear modulus, μ, Burger's vector, $\mathbf{b}$, and the surface energy, γ_s by Rice and Thompson [162]:

$$\frac{\mu \mathbf{b}}{\gamma_s} > 7.5 - 10 \tag{3.43}$$

Later, in order to account for ledge formation, Zhou *et. al.* [163] introduced a new criterion for the ductility as:

$$\frac{\gamma_{\mu s}}{\mu \mathbf{b}} < 0.014 \tag{3.44}$$

where $\gamma_{\mu s}$ is the maximum shear energy. Another approach that is using a *ductility parameter* which is independent of the shear modulus and Burgers vector, A, is introduced as the ratio of critical cleavage stress (σ_c) to the critical shear stress (τ_c):

[161]:

$$A = S\frac{\sigma_c}{\tau_c} \tag{3.45}$$

where S is the Schmidt factor that is defined as:

$$S = cos(\theta)cos(\alpha) \tag{3.46}$$

where θ is the angle between the applied load direction and the slip plane normal and α the angle between the applied load direction and the slip direction. If $A < 1$ the material is considered brittle and it is considered ductile for $A > 1$. Finally, a similar but simpler approach, using the energy instead of the stress is defined by Wang *et. al.* [164]:

$$D = \frac{G_c}{\gamma_{\mu s}} \tag{3.47}$$

where they consider materials with $D < 1$ as brittle.

Chapter 4

Effects of Additives and Impurity on Adhesive Behaviour of NiAl(110) / Al_2O_3(0001) Interface: An *ab initio* Study

4.1 Introduction and Theory

A combination of atomic-scale calculations together with semi-empirical formula is shown to provide essential guidance in the development of next generation TBCs. Recently, the effects of S, Pt and Hf on the β-NiAl(110)/Al_2O_3(0001) interface [17], and S, Pt, Hf and Hf+S co-doping on the γ-Ni(111)/AlO(0001) interface [46] are studied using density functional theory (DFT) calculations. To our knowledge, however, there are no systematic research and data available on effects of co-doping with two REs, Pt with an RE, and Pt with S on an β-NiAl(110)/Al_2O_3(0001) interface. In this work, we initially studied the effects of individual S, Pt, Hf, Zr, Cr and Y atoms on the interface adhesion, and then we investigated possible synergistic and antagonistic effects of co-doping with these elements using DFT calculations. This will enable us to examine and reveal how and why certain elements accelerate the interface failure, while others improve the interface adhesion in terms of electronic structures at the atomic scale.

The spin-polarized DFT total energy calculations are carried out using the Vienna

Ab initio simulation package (VASP) using a plane-wave basis set [118]. The projector augmented wave (PAW) potentials are used to describe the interactions of valence electrons with the ion and core electrons for all elements [137] where Ni $4s^2 3d^8$, Al $3s^2 3p^1$, Pt $6s^1 5d^9$, Hf $6s^2 5d^2$, S $3s^2 3p^4$, Zr $5s^2 4d^2$, Cr $4s^1 3d^5$,O $2s^2 2p^4$ and Y $5s^2 4d^1$ electrons are treated as valence. The Perdew-Wang generalized gradient approximation (GGA) is used to calculate the electron exchange and correlation energy [127]. The Brillouin zone integration is performed using a gamma point centered 3 x 7 x 1 Monkhorst Pack grid that yields 11 irreducible k-points [165]. The occupation of electronic states is determined according to first order Methfessel-Paxton scheme with a smearing width of 0.2eV.

The periodic supercell model of the coherent NiAl/Al_2O_3 interface is constructed from three Al-O_3-Al layers laid on the top of five Ni-Al layers [17]. Each Ni-Al layer is made up of five adjacent NiAl(110) unit cells, and each Al-O_3-Al layer is made up of three adjacent Al_2O_3(0001) unit cells along the $[1\bar{2}10]$ direction as shown in Figure 4.1. The NiAl(110) slab contains a total of 25 Al and 25 Ni atoms, and the Al_2O_3(0001) slab has 27 O and 18 Al atoms. The periodic repetitions of supercell geometry along the z-axis are separated by 12Å of vacuum to eliminate interactions between periodic cells, and the Al_2O_3 slab is cut to have an Al truncated surface since it is shown to be its most stable termination [16, 17, 166]. The calculated bulk NiAl lattice constant of 2.891Å, which is in good agreement with the experimental value of 2.887Å, yielded a lattice misfit of 0.5% between NiAl and Al_2O_3 surfaces, demonstrating a reasonable coherent interface model. The two bottom layers of the NiAl model are kept fixed, without allowing relaxations, throughout the calculations.

Initially the two slabs are placed to ensure that most of the Al atoms from the oxide are placed over the Ni-Ni bridge sites on the NiAl(110) surface [17]. In order to find the equilibrium interface separation of NiAl(110)/Al_2O_3(0001) slabs, the total energy calculations of the supercell model are implemented with a full relaxation scheme of

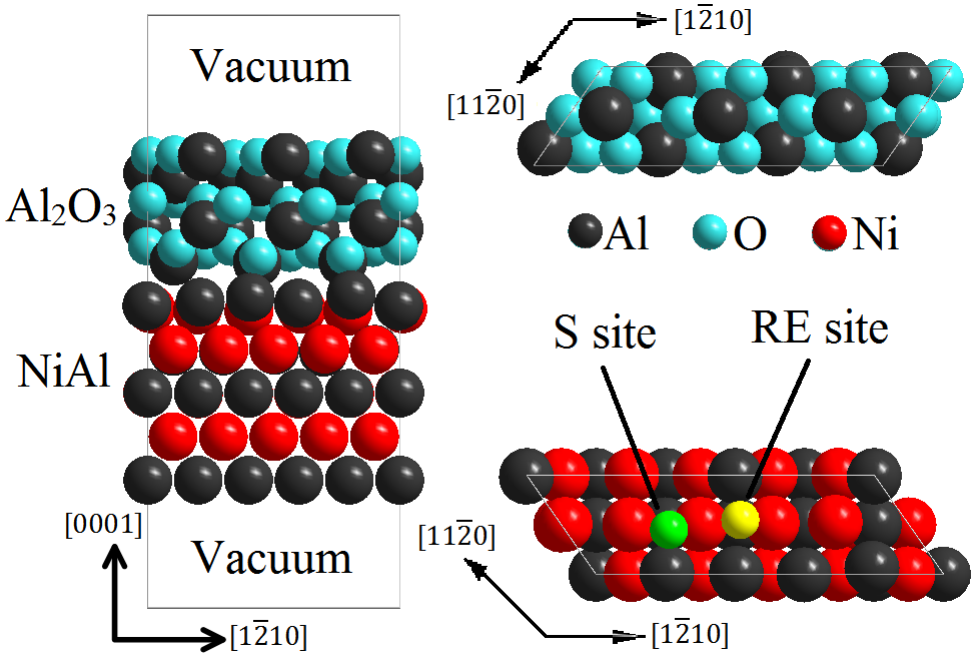

Figure 4.1: The atomic geometry of the clean interface. The red, blue and black atoms represent Ni, O and Al respectively. Yellow and Green atoms show the preferred locations of reactive elements and sulphur distributed at the interface.

atomic positions as a function of the interface separation d which is defined as the distance between the Al atoms located at the top layer of NiAl and the bottom layer of Al_2O_3. At d= 1.67 Å, the maximum work of adhesion W_{ad} of 0.832 J/m^2 is obtained. This interface is defined as the clean interface, and used as a baseline for comparison to identify the effects of alloying additives or impurity on the interface adhesive behaviour. It is noticed that although the current procedure of finding the equilibrium separation differs from ref. [17], the calculated separation of Ni-Al_{Oxide} of 2.334 Å is quite close to the Ni-Al_{Oxide} separation of 2.32 Åassumed in [17] as an initial input to construct the interface. Interface relaxations are performed in steps. First relaxation is done along the direction that is normal to the interface. Secondly a full relaxation, until the forces on the relaxing atoms (all except the two bottom layers of NiAl) are less than 0.07 eV/Å is implemented. Thirdly, the conjugate gradient minimization algorithm is changed to the quasi-Newton algorithm and the atoms are allowed to relax until

all forces are less than 0.05 eV/Å. As a final step, the atomic positions in all doping schemes are fully relaxed until the interatomic interactions are less than 0.01 eV/Å.

To examine the potential effects of elements on the interface, Pt, S, Hf, Zr, Cr and Y are individually placed into the relaxed clean interface as shown in Figure 4.1. In the case of single element doped interfaces, only one dopant or impurity atom is added; while for the co-doped interfaces, two different doping atoms are placed at the interface. For the Pt doped or Pt co-doped interfaces, one Ni atom at the interface is substituted by one Pt atom since Pt is shown to prefer to occupy the Ni sites in NiAl [54]. Finally, the work of adhesion of each interface is calculated in order to assess the effects of additives and impurities on the interface adhesion and the ELF is utilized to examine the potential correlation between the electronic structures and the interface adhesion.

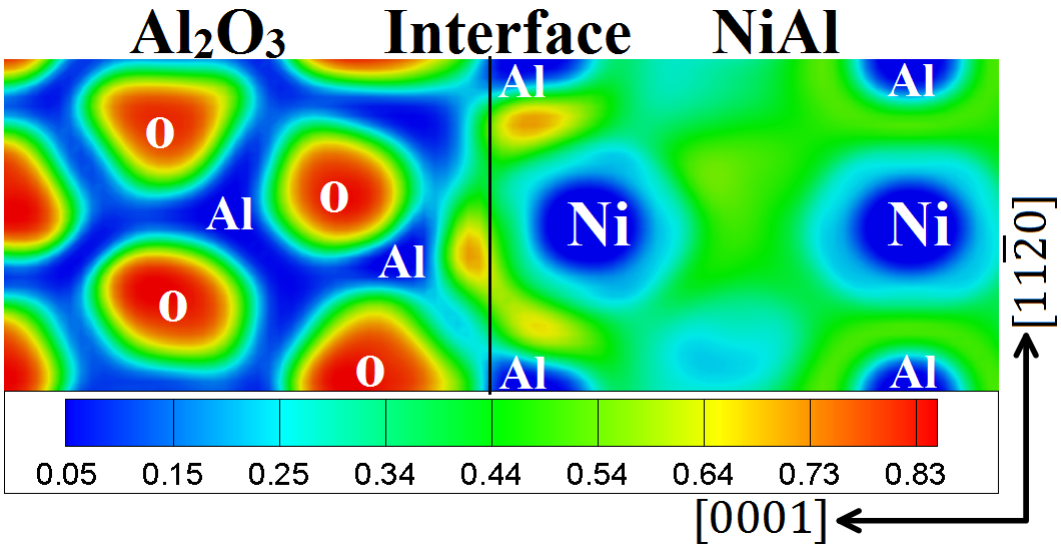

Figure 4.2: The ELF cross section of the clean interface

4.2 Results and Discussion

To reveal atomic-scale mechanisms associated with the interfacial properties, the ELF of the clean interface, illustrated in Figure 4.2, is first examined. It is found that Ni atoms adjacent to the interface move downward into the bulk NiAl, while Al atoms

Segregant "A"	W_{ad} (J/m^2)	+ Segregant "B"		
		Hf	**Cr**	**S**
None	0.832, 0.661[17], 4.8[45], 2.82[47]			
S	0.266, 0.181[17]			
Pt	0.845, 0.672[17]	1.764	1.407	0.355
Y	1.049	3.155	0.784	
Cr	1.412	0.691		0.518
Zr	1.707	3.106		
Hf	1.76, 2.056[17]			0.749

Table 4.1: The interfacial work of adhesion W_{ad} values for all doping schemes

from NiAl move towards the Al_2O_3 resulting in a rippling behaviour at the NiAl layer adjacent to the interface, consistent with previously reported experimental observations [13, 29, 31–33]. The electron localization between the Ni and Al_{Oxide} atoms display a covalent type bonding, while the distribution of electrons between the Al_{NiAl} and O atoms implies formation of an ionic Al_{NiAl}-O bond across the interface. These two types of bonds, i.e., covalent type Ni-Al_{Oxide} and ionic type Al_{NiAl}-O, constitute the dominant bonding across the clean NiAl(110)/Al_2O_3(0001) interface, which in turn governs the interface adhesion W_{ad}.

To examine the effects of REs, Pt and S on the interface adhesion and associated bonding characteristics, the NiAl/Al_2O_3 interface is modeled by initially inserting one S atom or an individual RE atom at the clean interface between two slabs as shown in Figure 4.1. The S atom is placed on top of a 2Ni-Al site, and the REs are sited on top of a Ni-Ni bridge, since these locations are determined as their preferred adsorption sites in [49]. Table 4.1 and Figure 4.3 demonstrates the calculated work of adhesion values, W_{ad}, and Table 4.2 lists all atomic separations across the interface for all doping schemes scrutinized.

Separation (Å)	**Segregants "A+B"**								
	Hf+S	**Cr+S**	**Pt+S**	**Hf+Pt**	**Cr+Pt**	**Hf+Cr**	**Y+Cr**	**Y+Hf**	**Zr+Hf**
Ni-Al$_{oxide}$	2.34(3)	2.42(3)	2.41(2)	2.32(3)	2.39(4)	2.42(4)	2.41(3)	2.21(3)	2.28(3)
Al$_{NiAl}$-O	1.98(1)	1.91(1)	1.86(3)	1.85(3)	1.84(4)	2.96(1)	1.97(1)	3.27	3.26
A-B	2.75	2.12	2.38	2.95	2.93	1.93	2.52	3.65	3.38
A-O	1.98(4)	2.00(3)	0	2.10(2)	2.04(3)	1.93(4)	2.14(4)	2.08(4)	2.03(4)
A-Al$_{oxide}$	2.9(1)	2.62(4)	2.58(1)	2.82(2)	2.69(1)	2.82(2)	2.88(2)	2.76(1)	2.82(1)
A-Ni	2.55(1)	2.71(1)		2.58(1)	2.3(1)	2.61(1)	2.5(2)	2.57(1)	2.43(1)
A-Al$_{NiAl}$	0	2.41(1)		2.76(4)	2.59(3)	2.85(1)	2.78(1)	0	2.83(1)
B-O	2.79(3)	2.5(2)	2.59(2)	0	0	1.95(2)	1.83(2)	1.98(4)	1.97(4)
B-Al$_{oxide}$	2.35(1)	2.68(1)	2.78(2)	2.46(1)	2.48(1)	2.52(1)	2.72(1)	2.97(1)	2.93(1)
B-Ni	2.18(1)	2.15(2)	2.07(1)			2.19(2)	2.54(2)	2.58(2)	2.58(2)
B-Al$_{NiAl}$	2.37(2)	2.15(1)	2.3(2)			2.42(2)	2.4(2)	0	0

Separation (Å)	**Segregant "A"**						
	Clean	**S**	**Pt**	**Hf**	**Cr**	**Zr**	**Y**
Ni-Al$_{oxide}$	2.33(4)	2.37(3)	2.35(3)	2.34(5)	2.38(5)	2.35(4)	2.41(3)
Al$_{NiAl}$-O	1.97(5)	1.89(4)	1.94(4)	1.88(3)	1.84(6)	1.85(3)	1.95(1)
A-O		2.54(1)	0	2.04(3)	2.07(2)	2.17(2)	2.09(4)
A-Al$_{oxide}$		2.79(2)	2.46(1)	2.79(2)	2.72(2)	72.85(2)	2.78(3)
A-Ni		2.1(2)	N/A	2.63(2)	2.34(2)	2.58(2)	2.58(2)
A-Al$_{NiAl}$		2.28(3)	N/A	2.84(1)	2.58(3)	2.72(3)	2.77(1)

Table 4.2: Atomic separation between the Ni-Al$_{oxide}$ and O-Al$_{NiAl}$ atoms at the interface, and the dopant with their first three closest atoms for doped structures. The numbers in the brackets specify the number of that specific type of bond across the interface

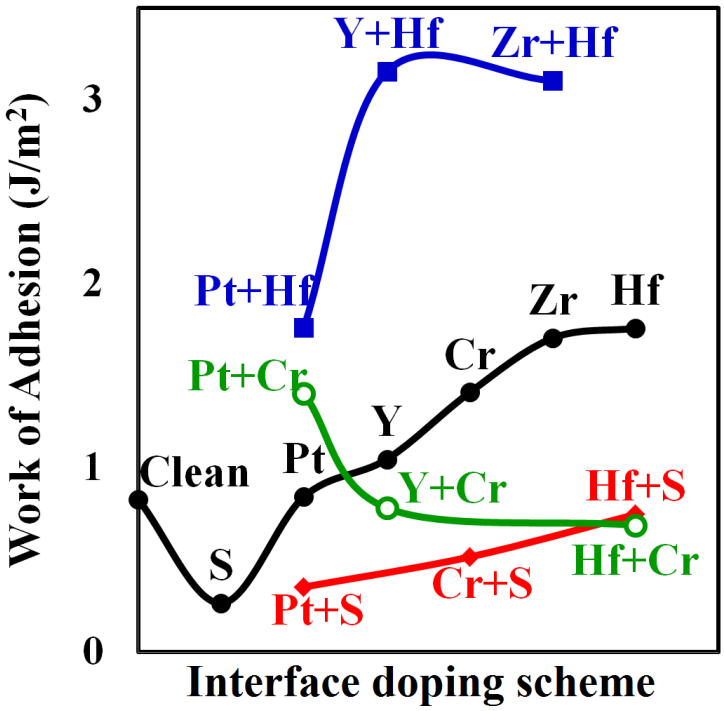

Figure 4.3: The interface work of adhesion, W_{ad} trends

4.2.1 Effects of Sulfur and Additives

After relaxations, Sulfur segregate towards the NiAl surface rather than the oxide (Figure 4.4 (c)) and its presence at the interface degrades the work of adhesion significantly, in qualitative agreement with previous reports [17, 45, 48]. It is noted from Table 4.2 that although the bond length of Al_{NiAl}-O in the vicinity of S shrinks slightly compared to the clean interface, the number density of both Al_{NiAl}-O and Ni-Al_{Oxide} bonds are reduced. According to the density of states of the Ni that is adjacent to the S atom, the valence electrons of Ni considerably shift downward, away from the Fermi level after S segregation (Figure 4.5). This indicates that S is more negatively polarized which is further confirmed by the ELF around the S site in Figure 4.4 (c). The negative polarization of S results in a repulsive interaction between S and its nearest O atoms, and this interaction is responsible for weakening the interface adhesion. This repulsive interaction is also noticed from the flattened shape of the ELF between S and O. These

bonding features determine the interfacial adhesion.

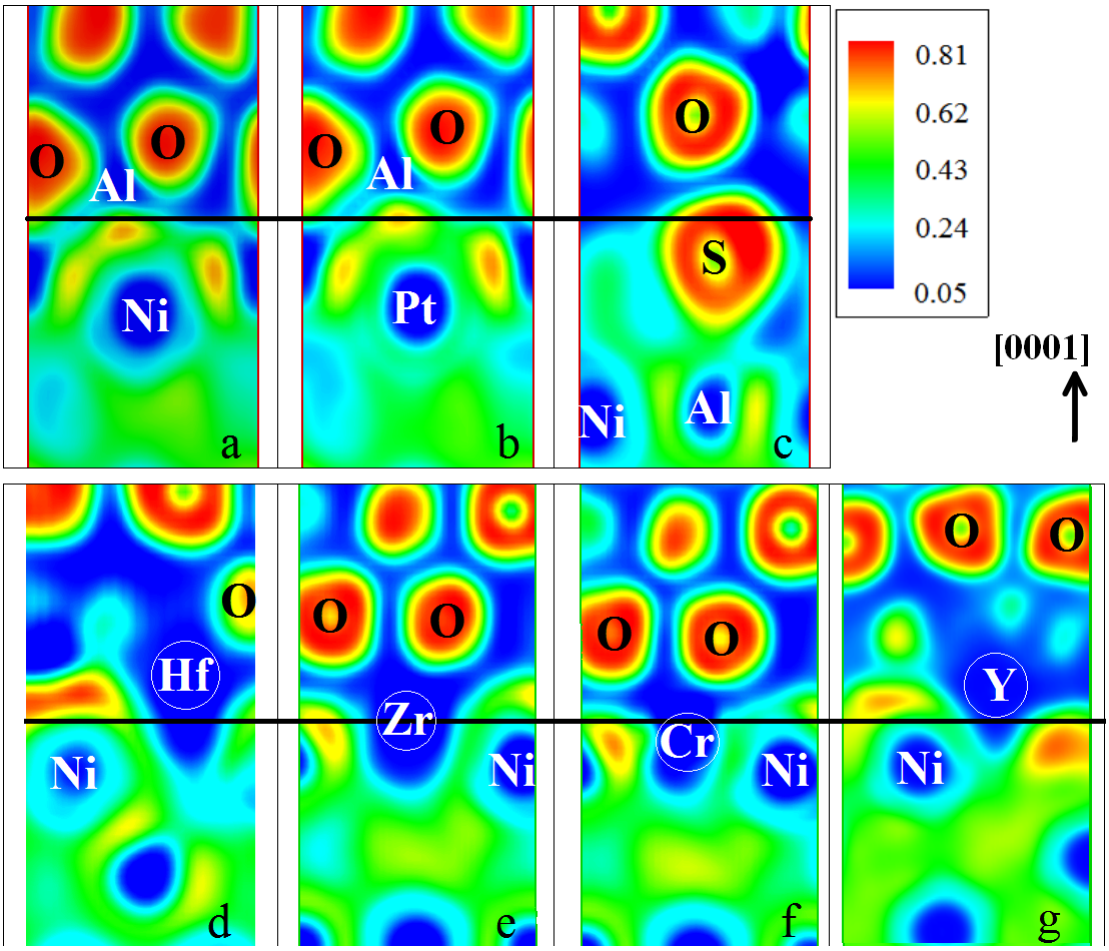

Figure 4.4: ELF of the single element doped and the clean $NiAl/Al_2O_3$ interfaces. a)clean interface b)Pt doped c) S segregated d) Hf doped e) Zr doped f)Cr doped g) Y doped

In the case of Pt-doped interface, the interfacial adhesion W_{ad} is enhanced by ˜1.5% of the clean interface, which suggests that Pt behaves in a similar way as the Ni atom that it has substituted at the $NiAl/Al_2O_3$ interface. By a comparison of ELF illustrated for both clean and Pt-doped interfaces in Figure 4.4(a) and (b), similar bonding characteristics are observed around Pt and Ni atoms with slightly higher electron localization between Pt and its surrounding Al atoms, which is responsible for this modest increase in the work of adhesion. To evaluate the effects of RE addition on the W_{ad} of $NiAl/Al_2O_3$ interface, two doping sites are considered such as the interface inter-

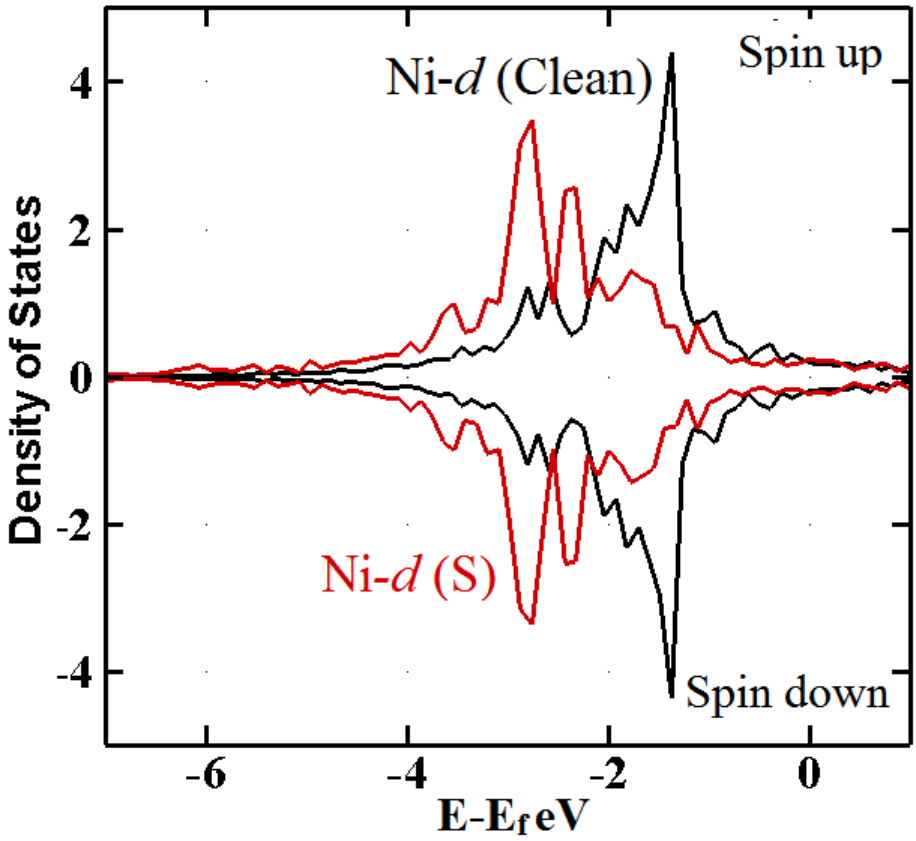

Figure 4.5: Ni density of states at the clean and S-containing interface where E_F is the Fermi level

stitial and the lattice substitution. For instance, Hf is initially placed at an interface interstitial site between the NiAl and Al_2O_3 slabs. It is reported [167] that Hf prefers to substitute for Al in the bulk NiAl; therefore Hf is placed to substitute for one Al atom adjacent to the interface as the second doping scheme. A larger W_{ad} value is obtained when Hf is doped at an interfacial interstitial between the two slabs. This doping strategy is also employed by ref. [17]. Therefore only the interface interstitial model is considered for REs distribution at the interface in this research.

Doping Hf to the clean interface results in a significant enhancement in W_{ad}. It is determined from the Hf-doped interface geometry that Hf prefers to segregate towards the Al_2O_3 side, consistent with experimental observations [63, 68]. It is interesting to note from the ELF in Figure 4.4(d) that Hf forms ionic bonds with O atoms while

forming intermetallic bonds with Ni at the same time. This new peculiar mixed bond characteristic is responsible for the W_{ad} enhancement. In addition, the number density of Ni-Al_{Oxide} bonds is slightly increased and the bond lengths of Al_{NiAl}-O are shrunk to some extent due to the presence of Hf at the interface, which possibly increases the strength of the Al_{NiAl}-O bonds. Therefore, it is this peculiar mixed bond combined with the strengthening of Al_{NiAl}-O bonds that result in the enhancement of the W_{ad}.

It is reported experimentally [61, 63] that Zr is capable of enhancing the oxides/metal scale adhesion. In the Zr-doped interface, a similar bond characteristics as in the Hf-doped interface is observed (Figure 4.4(e)). A peculiar mixed O-Zr-Ni bond is formed across the interface, and the bond lengths of Al_{NiAl}-O shrunk after addition of Zr to the interface. According to Table 4.2, the Zr-Ni bond in the Zr-doped interface is shorter than the Hf-Ni in the Hf-doped interface, while the length of the Al_{NiAl}-O bonds in the Zr-doped interface is larger than its counterpart in the Hf-doped interface. This difference in bond lengths result in a smaller increase in W_{ad} than the Hf-doped structure.

It is reported that Cr addition to the bond coat increases the oxide growth rate, and thus may reduce the TBC lifetime. It is also reported that at high temperatures, Cr_2O_3 is not stable, with a potential tendency of being vaporized into gas state that in turn deteriorates adhesion strength of the interface. It is not clear, however, if Cr is capable of increasing the interface adhesion when it resides at the interface between NiAl and Al_2O_3. To examine the effects of Cr doping on the interface, Cr is placed into the interface interstitial between NiAl and Al_2O_3 slabs. It is observed that unlike Hf and Zr-doped interfaces, Cr positions midway between these slabs, but still increases the W_{ad} compared to the clean interface. Similar to the Hf and Zr-doped interfaces, a mixed O-Cr-Ni bond forms across the interface, and the Al_{NiAl}-O bond lengths decrease. As a result, these bonding characteristics lead to an increased W_{ad}.

Although the addition of Y to the bond coat is reported to increase the lifetime

of TBCs [75], the underlying atomic level mechanisms are unclear. To understand its positive effects at the microscopic level, Y is also doped into the NiAl/Al_2O_3 interface. According to Table 4.2 and Figure 4.4(g), similar to the Hf (Zr or Cr)-doped interfaces, a mixed O-Y-Ni bond formation is determined. However the Ni-Al_{Oxide} bonds stretch and their number density drop slightly. It is also observed that although the Al_{NiAl}-O bond length remains the same, its number density reduces significantly. Formation of the mixed bond induces an increase in the W_{ad} but due to the reduction in the number density of Al_{NiAl}-O and Ni-Al_{Oxide} bonds, a smaller increase, compared to the Hf, Zr and Cr-doped interfaces, is achieved in Y-doped interface.

4.2.2 Mitigating detrimental effects of S by additives

It is shown above that the addition of Pt and REs is capable of strengthening Al_2O_3/NiAl scale adherence. Therefore, it is expected that these elements could mitigate, to some extent, the detrimental effects induced by S that segregates to the interface [50, 51, 60, 63]. Pt, Hf and Cr are doped at the interface with an initial position adjacent to the S atom, and then the atomic geometry is allowed to relax fully. The calculated work of adhesion values that are listed in Table 4.1 shows that doping Pt, Hf or Cr to the interface is capable of mitigating the harmful effects of S; however their positive effects are not significant enough to compensate negative effects S compared to the clean interface in terms of W_{ad}. In this research, the doped interfaces with Pt and REs with impurity S are referred as the *X+S interface* hereafter, where X = Hf, Cr and Pt.

In the case of Hf+S interface, the bond length of Ni-Al_{Oxide} and Al_{NiAl}-O remains almost unchanged, while the number density of Al_{NiAl}-O bonds per unit area is significantly reduced from 5 to 1 due to the presence of S at the interface. This number density reduction leads to a considerable drop in W_{ad}, reflecting the serious negative

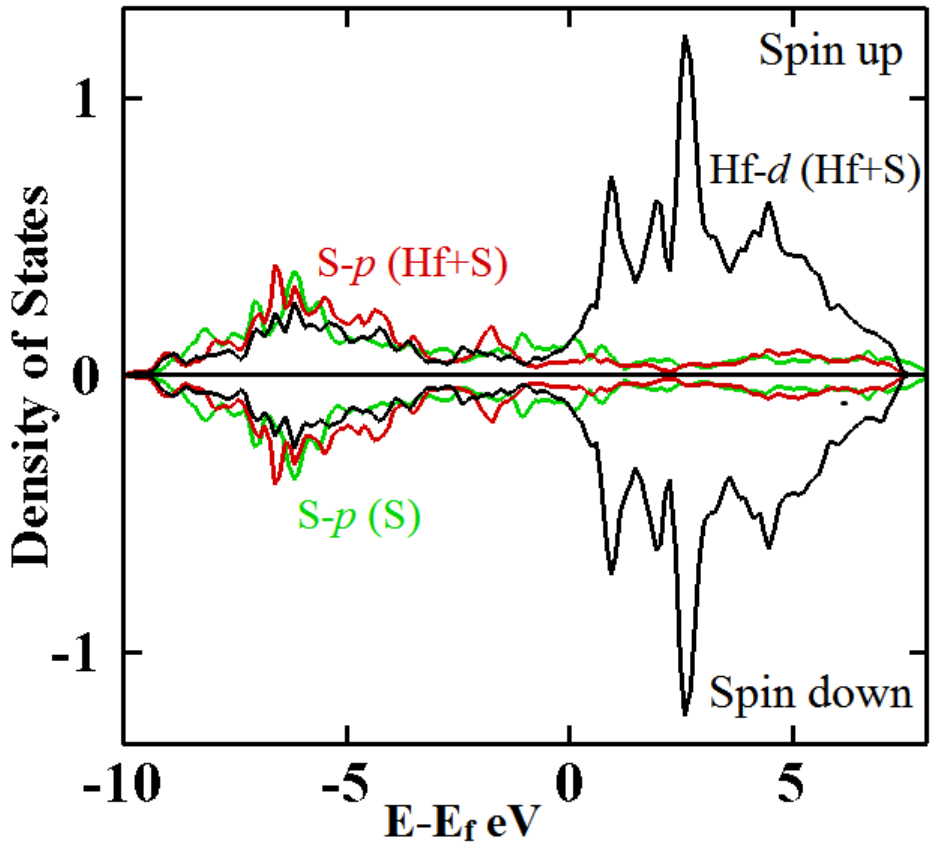

Figure 4.6: DOS of S p-obitals in pure S and Hf+S doped interface, DOS of Hf in Hf+S doped interface.

effects of S. The peak value of S p-orbitals at Hf+S interface shifts downward relative to its peak at the pure S doped interface, indicating a charge transfer from Hf to S atom (Figure 4.6), leading to a highly polar covalent Hf-S bond formation. As similar to the Hf-doped structure, in the Hf+S interface a mixed O-Hf-Ni bond forms across the interface as presented in the ELF in Figure 4.7. This bond is responsible for the increase in the W_{ad} compared to a purely S segregated interface. In addition, S at this interface forms additional highly polar covalent type of bonds with Al_{Oxide}, and forms weak covalent bonds with both Ni and Al from the NiAl side, Figure 4.7. These bridging bonds across the interface contribute positively in increasing the W_{ad}. Therefore the net effect of the bonding characteristics in the Hf+S interface on W_{ad} is similar to the clean interface in terms of the W_{ad} values.

In the case of Cr+S interface, the number of Al_{NiAl}-O bonds is reduced significantly due to the presence of S, which in turn decreases the W_{ad}. The positioning of Cr between NiAl and Al_2O_3 slabs leads to formation of both ionic Cr-O and intermetallic Cr-Al_{NiAl} bonds with a small number density. As in the Cr-doped interface, this mixed bond formation gives rise to the enhancement of W_{ad} to some extent. The S atom is found to form weak covalent bonds with Cr (from ELF) and with Ni and Al from the NiAl slab. No S-Al_{Oxide} bond formation is determined to link the slabs as in the Hf+S interface. Therefore, compared to Cr, Hf is more successful in mitigating Ss' detrimental effect of reducing the W_{ad}. In the Pt+S interface case, the Ni-Al_{Oxide} bonds stretch, and the number density of bonds reduce because of S segregation. These two features definitely cause a drop in the W_{ad}. Across the interface an intermetallic Pt-Al_{Oxide} bond is determined. Similar to the Cr+S interface S forms bonds with Ni, Al and Pt from the NiAl side, while no S-Al_{Oxide} interaction is observed, therefore no extra bridging bonds that links NiAl to Al_2O_3 is detected. These bond characteristics demonstrate that Pt's function in mitigating the detrimental effect of S is limited compared to Hf, which is confirmed from W_{ad} values in Table 4.1.

4.2.3 Pt +X interfaces

To examine a possible synergistic effect of Pt with Hf (or Cr) at the interface, one Hf (Cr) atom is placed at the interface adjacent to Pt that is substituting a Ni atom. The results, however, show that co-doping Pt with Hf (Cr) induces a slight change in the work of adhesion W_{ad} compared to that of the single Hf (Cr) doped interfaces. This demonstrates that no synergistic effect exists between Hf (Cr) and Pt at the interface.

Unlike the single Hf doped interface, instead of moving towards the oxide, Hf at the Pt+Hf interface moves horizontally away from Pt and stretches the Hf-Pt separation to 2.95Å (Table 4.2). By a comparison of atomic geometries of Hf and Pt+Hf interface

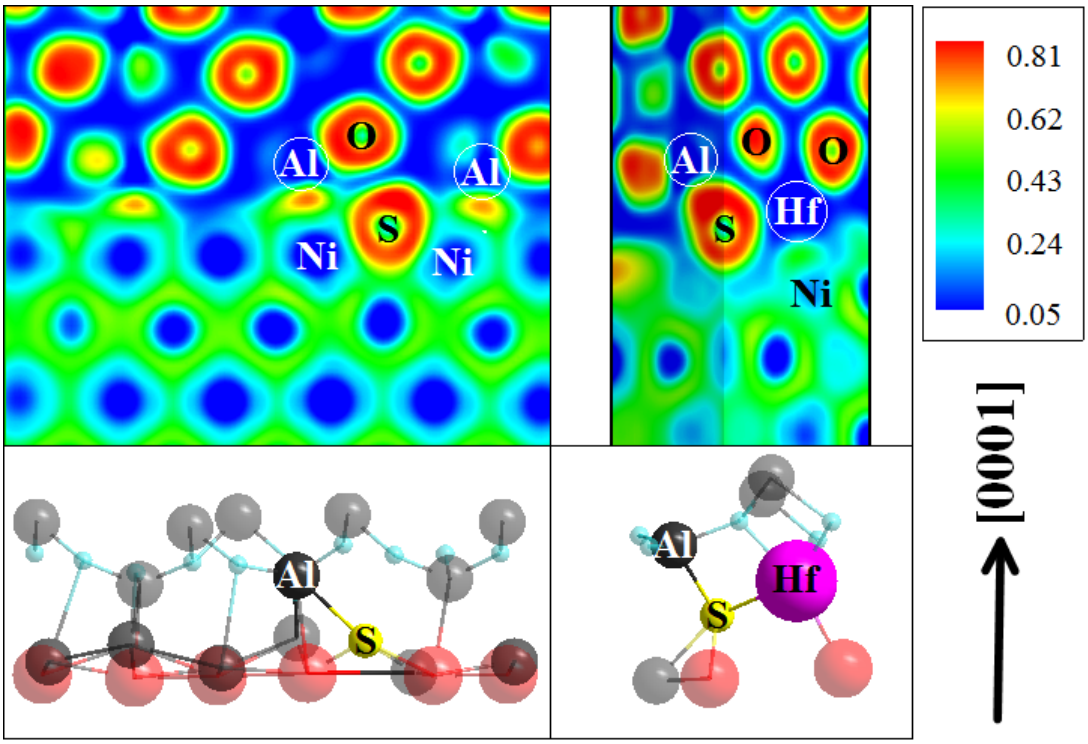

Figure 4.7: ELF and the atomic geometry of 1) Pure S doped interface 2) Hf+S doped interface

(Figure 4.8), one can see that this horizontal displacement also stretches the Hf-O separation, therefore reducing the number of Hf-O bonds. Hf still forms bonds with both Ni and Al_{NiAl} but the geometry of NiAl adjacent to the interface changes; an Al atom from NiAl side moves towards the oxide, shortening and strengthening the Al_{NiAl}-O bond. Furthermore, the DOS plot in Figure 4.9 for Hf+Pt interface does not show a hybridization between Hf and Pt d-states and ELF figure shows a similar localization to that of the single Hf doped interface, which indicates that Pt acts in a similar manner to a Ni atom (Figure 4.10). Hence, it is suggested that the weakening of Hf-O bonds is compensated by the shortening of the Al_{Oxide}-O bonds, and formation of both Hf-Al_{NiAl} and Hf-Ni bonds, which in turn keeps the W_{ad} unchanged compared to the pure Hf doped interface.

Similar to the Hf+Pt interface, the Cr atom in the Cr+Pt interface shown in Figure 4.10 deviates from Pt, stretching the Cr-Pt separation to 2.94Å, which is much greater

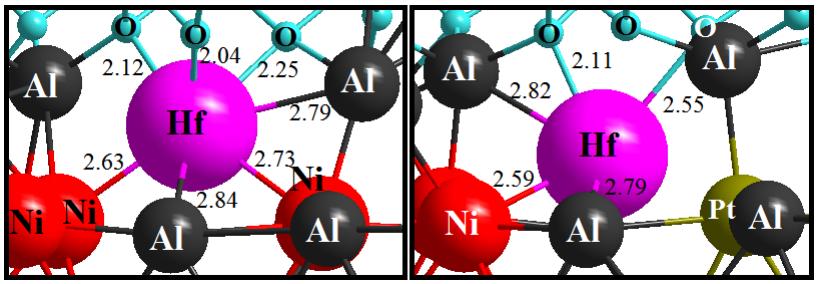

Figure 4.8: Atomic geometry of pure Hf and Hf+Pt doped interfaces

compared to the Cr-Pt bond length (2.56Å) in bulk CrPt crystal [168]. Moreover, as seen in Table 4.2, the shortest bond length of both Al_{Oxide}-O and Ni-Al_{Oxide} equals to that in the single Cr-doped interface, resulting in a W_{ad} close to that of a single Cr-doped interface.

4.2.4 RE+RE doped interfaces

To examine the effect of interactions between REs on the oxide adhesion, a pair combination of REs such as (Y, Hf), (Zr, Hf), (Hf, Cr) and (Y, Cr) are initially placed at the interface at nearest adjacent sites to each other. Except for Hf+Cr and Y+Cr doped interfaces, a synergistic effect on increasing W_{ad} is observed between the pairs of REs. For (Y, Hf) and (Zr, Hf) doped interfaces, no rippling behaviour is observed at the topmost layer of NiAl. Therefore, unlike the single RE doped interfaces, no Al_{NiAl} atom at those (Y, Hf) and (Zr, Hf) doped interfaces moves towards the oxide. Consequently, the Al_{NiAl}-O separation significantly stretches, and in turn makes a lesser contribution to the interface adhesion, whilst the Ni-Al_{Oxide} bond lengths alter slightly compared to that of the clean interface.

The work of adhesion W_{ad} of the (Y, Hf) and (Zr, Hf) doped interfaces are evaluated and is found three times larger than the work of adhesion of the clean interface which signifies a synergistic effect between these REs. To reveal the mechanism associated with this enhancement of oxide adhesion to NiAl, the interactions between these dopant

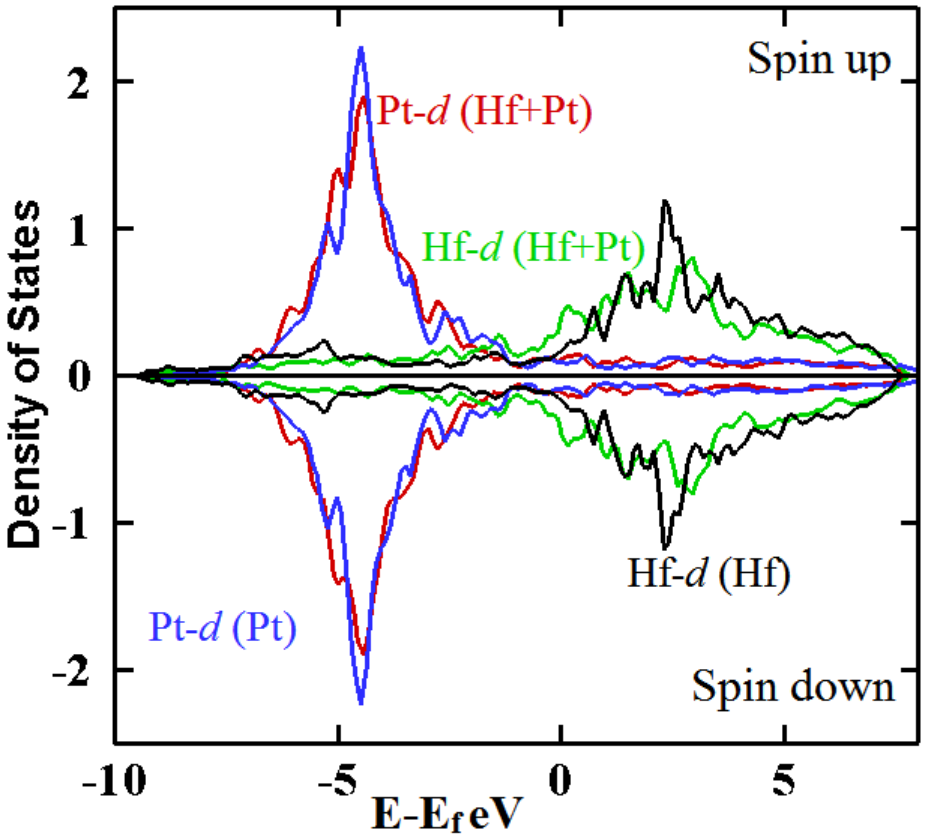

Figure 4.9: DOS of Pt p-orbitals in pure Pt and Pt+Hf doped interfaces and DOS of Hf in pure Hf and Pt+Hf doped interfaces.

atoms are analyzed via the bond length, DOS and ELF plots. In the (Y, Hf) and (Zr, Hf) doped interfaces, a mixed type O-Hf-Ni bond with a bond length close to that of the Hf mixed bonds in the single Hf doped interface is formed across the interface with a high number density, as seen Table 4.2 and ELF in Figure 4.11. Another mixed bond, O-Y(Zr)-Ni, is also formed with both a close bond length and a number density to its counterpart in the single RE doped interface. These additional bonds together make the dominant contribution to the considerable enhancement of W_{ad}. In addition, by a comparison with the single RE doped interface, a downward shift in O p-orbitals can be observed in Figure 4.12 for both Hf+Zr and Hf+Y interfaces, indicating an extra charge transfer from the second RE to the O atom, promoting a combined ionic Y(ZR)-O-Hf bond formation between REs and O. In addition, according to the ELF

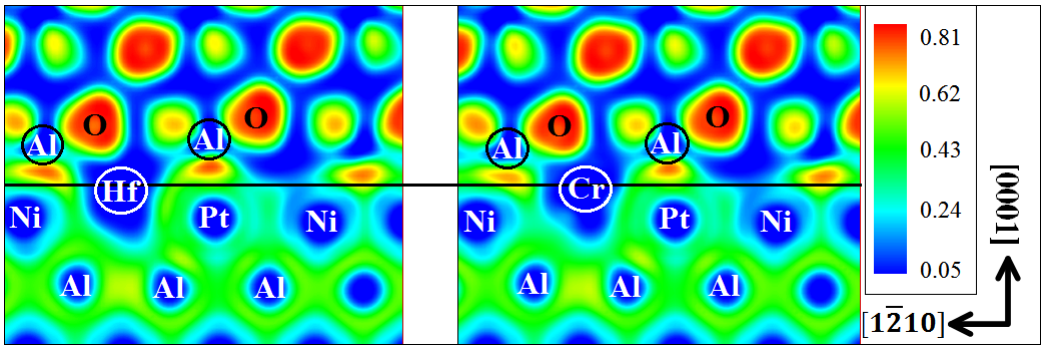

Figure 4.10: Cross section of the ELF for Hf+Pt and Cr+Pt doped interfaces.

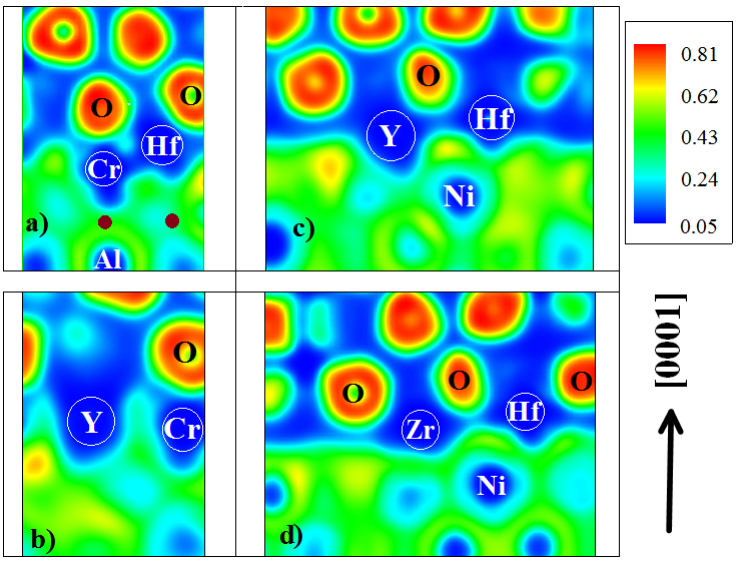

Figure 4.11: Cross section of ELF for a) Cr+Hf doped b) Cr+Y doped c) Cr+Zr doped d) Y+Hf doped interfaces. ELF is cut through the plane passing through both atoms. Brown circles indicate background atoms.

plots in Figure 4.11, the electron delocalization around both Hf and Zr(Y) followed by increasingly localized electrons around O atoms also signifies a charge transfer to the O atoms. As a result, the additional increase in the work of adhesion can be attributed to the formation of strong, ionic RE-O-RE bonds across the interface.

In contrast, an antagonistic effect on interface adhesion in (Hf, Cr) and (Y, Cr) doped interfaces is identified. The calculated W_{ad} is close to that of the initial clean interface, indicating an entire cancellation of enhancement that is obtained in pure Hf, Y and Cr doped interfaces. The number density and bond length of mixed O-Hf(Y)-

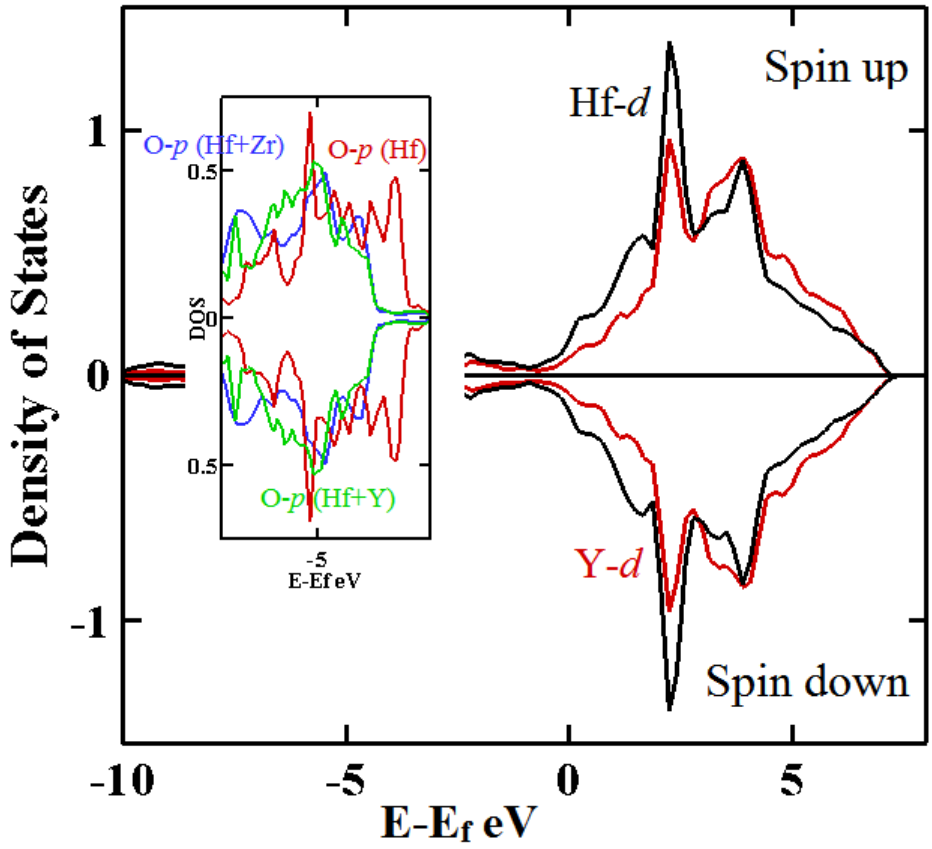

Figure 4.12: DOS of Y and Hf d-orbitals in Y+Hf doped interfaces and O p-orbitals in Hf doped, Hf+Y doped and Hf+Zr doped interfaces.

Ni bond in both (Hf, Cr) and (Y, Cr) interface are found at the same level as in the (Y, Hf) and (Zr, Hf) interfaces. However, it is observed that the number density of Al_{NiAl}-O bonds are considerably reduced, which results in a lesser contribution to the W_{ad}. Consequently the reduction in Al_{NiAl}-O bond density is complemented by O-Hf-Ni bonds. In principle, mixed types of bonds such as Cr-O and Cr-Ni could be formed based on the bond length distribution. The results, however, show that Cr does not induce an extra downward shift in O p-states (Figure 4.13), which indicates that there is no additional charge transfer to oxygen upon Cr addition, thus no ionic bonds form between Cr and O atoms as occurs in the single Cr doped interface. In addition, there is no electron hybridization between Hf and Cr d-states below the Fermi energy, and both Cr $3d$ and Hf $5d$-states show lower amplitudes compared to those at the single RE

doped interface. Furthermore, as seen from the ELF for the (Hf, Cr) interface shown in Figure 4.11, although the Hf-Cr separation is relatively small compared to other RE-RE separations, there is no electron localization around Cr or between Cr and Hf, which implies that there is no bond formation between these atoms. Therefore, the net result is that W_{ad} value is close to that of the clean interface due to no O-Cr-Ni bond formation and the drop of Al_{NiAl}-O bond number density. Similar results are also obtained for Y+Cr doped interface as shown in Figure 4.11 and Figure 4.14.

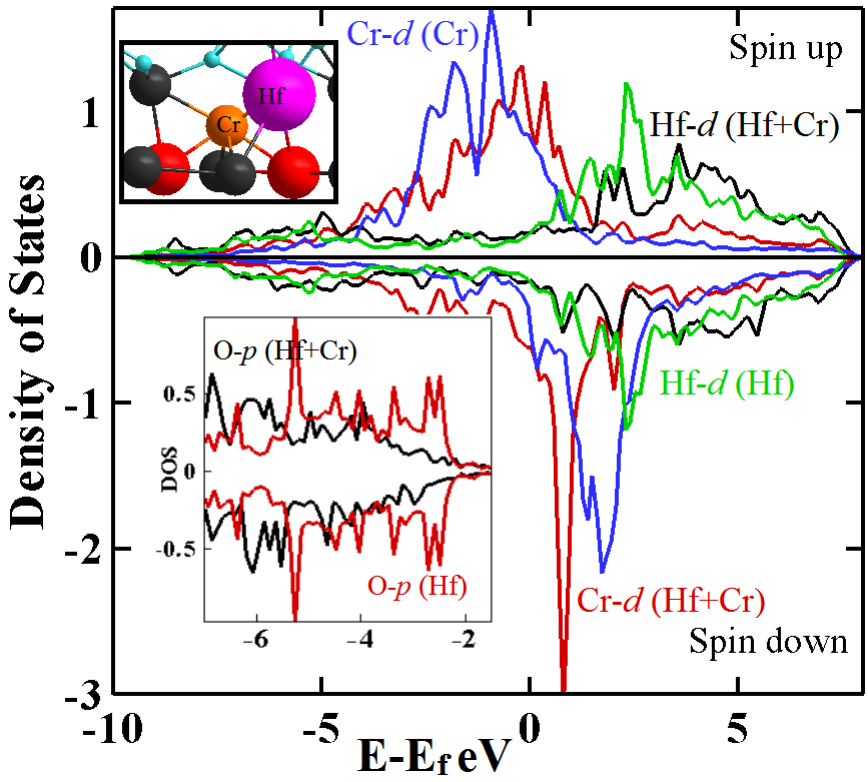

Figure 4.13: DOS of Hf and Cr d-orbitals in pure Hf, pure Cr and Hf+Cr doped interfaces. Atomic geometry of the Hf+Cr doped interfaces. O p-orbitals in Hf and Hf+Cr doped interfaces

It is found experimentally that Cr+Hf addition to TGO/bond coat interface has an overall negative effect on the work of adhesion and thus reduces the coating lifetime [68]. Although there are several factors that are responsible for this failure, decreased W_{ad} induced by the de-bonding of Cr-O and drop of bond number density are the

factors responsible as revealed by *ab initio* density functional theory calculations.

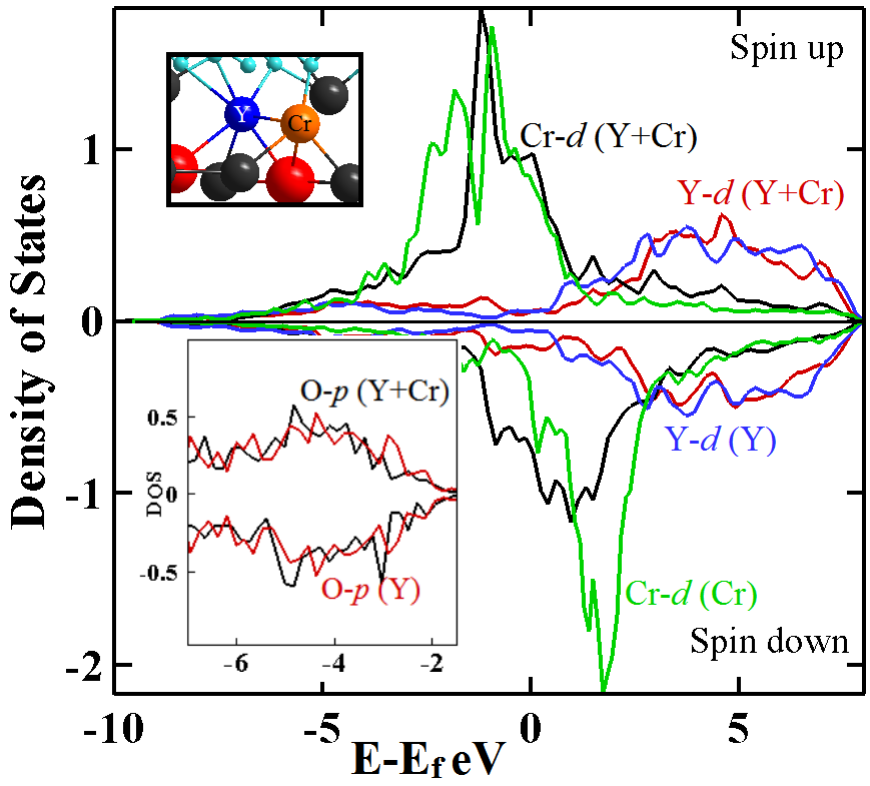

Figure 4.14: DOS of Y and Cr *d*-orbitals in pure Y and pure Cr doped interfaces. Atomic geometry of the Y+Cr doped interface and the O *p*-orbitals in Y and Y+Cr doped interfaces.

4.3 Conclusion

Using *ab initio* density functional theory, the effects of Pt, S and REs Hf, Y, Cr and Zr on the interface adhesion of NiAl(110)/Al_2O_3(0001) are evaluated with the purpose of elucidating the underlying atomic-scale mechanisms. Four schemes are implemented to simulate possible dopant combinations at the interface: (1) Single element, (2) S+Hf (Pt and Cr), (3) Pt+Hf (Cr), and (4) RE+RE. First, the Ni-Al_{Oxide} and Al_{NiAl}-O bonds are identified as the two dominant bonds that govern the W_{ad} for the clean interface. In agreement with previously reported theoretical and computational work [17, 38–48], presence of S at the interface is shown to significantly degrade the interface strength,

W_{ad}, due to the de-bonding of Ni-Al_{Oxide} and Al_{NiAl}-O bonds across the interface and the O-S repulsion. Even though experimentally Pt is suggested to improve the inteface adhesion, concurring with previous calculations [54–57], in this work Pt is not determined to improve the interface adhesion. For the single RE-doped interfaces, the formation of the mixed type O-(Hf, Y, Zr and Cr)-Ni bonds are responsible for the enhancement of the W_{ad}. Such increase in work of adhesion is expected for Hf, Y and Zr since experimentally these elements are shown to improve the TBC lifetime. However previously Cr is found to reduce the TBC lifetime by increasing the oxide growth rate. Such disagreement could stem from the fact that the simulations can only determine the adhesive trends and cannot include the effects of oxide growth or long term high temperature exposures.

The REs are known to alleviate the detrimental effects of S and improve the adhesion of the oxide to the bond coat [43, 44, 64–66]. In agreement, in this work, for the X+S interface with X = Hf, Cr or Pt, the O-Hf(Cr)-Ni bonds across the interface are determined to be responsible for the enhancement of the W_{ad}, thus is capable of mitigating the detrimental effect of S to some extent. As no O-Pt-Ni bond is formed across the interface, Pt addition is not as effective as Hf or Cr in alleviating the harmful effects of S. For the Pt+Hf(Cr) doped interface, no synergistic effect between Pt and Hf(Cr) is identified. For the RE+RE interfaces, although the Al_{NiAl}-O bonds are stretched, a synergistic effect between REs is determined for (Zr, Hf), (Y, Hf) interfaces and formation of strong O-Hf(Y,Zr)-Ni and Y(Zr)-O-Hf bonds across the interface is found responsible for this increase. In contrast an antagonistic behaviour between the REs of (Hf, Cr) and (Y, Cr) doped interfaces is identified, in which no O-Cr-Ni or Cr-O-Y(Hf) mixed bond formed across the interface and the number density of Al_{NiAl}-O largely dropped, decreasing the work of adhesion.

In agreement with experimental data that suggests Y is less effective in reducing the oxide growth [75, 76], the calculated W_{ad} of the Y doped interface in this study is

weaker than the Hf or Zr doped interfaces. Furthermore concurrent with experimental observations suggesting co-doping Y with Hf or Zr is more efficient than purely Y, Hf or Zr doped structures [77–79], an increased adhesion is determined for the (Y,Hf) and (Hf,Zr) co-doped interfaces.

Chapter 5

Effects of Additives on Sulphur diffusion in NiAl

5.1 Introduction and Theory

Few experimental studies related to S diffusion focused on the effects of Pt and the possible diffusion mechanism of S segregation in bulk NiAl. It is proposed that S diffusion in NiAl is taking place via interstitial mechanism and the effects of Pt on its diffusion is temperature dependent [38, 94]. While, at high temperatures (T>900^{o}C), Pt is observed to reduce the S segregation rate, at temperatures below 900^{o}C, presence of Pt is observed to increase the S diffusion rate in NiAl [94]. In addition, in a recent composition dependent study, Pt is observed to reduce S segregation to the surface in both Ni-rich and stoichiometric NiAl [50].

So far temperature dependent S diffusion in bulk NiAl with the presence of an additive has never been studied using theoretical methods. It is important to understand the atomic level mechanisms taking place during the diffusion of S in NiAl, and effects of additives on S diffusion since its segregation to NiAl/Al_2O_3 interface is detrimental and greatly reduces the TBC lifetime. In this study, first-principles density functional theory calculations are performed in order to investigate the site preference of S, clarify the effects of additives on S diffusion at the atomic level, and obtain temperature dependent diffusion coefficient of S in clean, Pt or Hf doped NiAl. Atomic level char-

acterization of S diffusion, and the understanding the role of Hf and Pt in this process will provide guidance for future research.

Spin-polarized density functional theory (DFT) is employed using the Vienna *Ab initio* simulation package (VASP) using a plane-wave basis set [118]. The Perdew-Wang generalized gradient approximation (GGA) is used to calculate the electron exchange and correlation energy [127]. The projector augmented wave (PAW) potentials are used to describe the interactions of valence electrons with the ion and core electrons for all elements [137] where Ni $4s^2 3d^8$, Al $3s^2 3p^1$, Pt $6s^1 5d^9$, Hf $6s^2 5d^2$, and S $3s^2 3p^4$, electrons are treated as valence.

For eliminating the segregants' interaction with its mirror periodic images, the formation energy of 55 and 129 atom supercells are calculated and a 55 atom supercell is found large enough to isolate the diffusing particles in periodic images for interstitial diffusion. Similarly, for the vacancy mediated diffusion calculations, 53 atom supercell is determined to isolate diffusing atom interactions between periodic images. For the 55(53) atom supercell, the Brillouin zone integration is performed using a gamma point centered 6 x 6 x 6 Monkhorst Pack grid that yields 54 irreducible k-points [165]. The occupation of electronic states is determined according to first order Methfessel-Paxton scheme with a smearing width of 0.2eV. A kinetic energy cutoff of 350 eV is used for all calculations.

In order to calculate the stoichiometric lattice constant of NiAl, starting with the experimental value of 2.887 Å, the atomic positions and the volume of the structure is allowed to relax. The calculated value of 2.891 Å, which is in excellent agreement with experimental values, is used for all subsequent diffusion calculations. All atom positions are allowed to relax until the forces on the ions are less than the threshold energy of 0.01 eV/Å for formation energy calculations, and 0.03 eV/Å for diffusion calculations since Marino *et. al.* [58] showed that reducing the threshold has a negligible impact on the calculated migration barrier.

The migration energy, which is the total energy difference between the saddle point and the energy of the initial stable point, is calculated using the climbing nudged elastic band method (CINEB) [119, 140–142]. For the diffusion path with both initial and final minima are known, a series of images are generated by a linear interpolation between the end states. The images, which are connected by imaginary springs, are permitted to relax until the Hellmann-Feynman forces on atoms are less than the threshold value. Finally by inverting the forces on the highest energy image, the highest energy image is made to climb along the minimum energy path (MEP) to obtain the saddle point.

In order to calculate the formation energy, the total energies of the bulk and modified NiAl are minimized with respect to the atomic positions until the resultant forces are smaller than the threshold value. Finally, the phonon frequencies are calculated with a displacement of ± 0.05Å at the Γ point using the *fitfc* utility in the Alloy Theoretic Automated Toolkit (ATAT) package [121] that utilizes the direct force constant supercell approach [120]. The electron localization function (ELF) is calculated for examining the relationship between the electronic structure and diffusion.

5.2 Results and Discussion

β-NiAl has an ordered B2-CsCl, body centered cubic (BCC) type structure and it consists of two interpenetrating Ni and Al simple cubic sub-lattices. As shown in Figure 5.1, at stoichiometric composition, the Al atoms occupy the corner sites (β-sites) and the Ni atoms occupy the body-centered sites (α-sites) of the unit cell. There are two distinct interstitial sites that an interstitial atom can occupy; tetrahedral (Figure 5.1(a)-blue) and octahedral (Figure 5.1(a)-red).

In a previous study, the preferred adsorption sites for Hf and Pt atoms in NiAl are determined as Al and Ni substitutional sites, respectively [169]. On the other hand, due to its smaller radius and higher diffusion rate compared to Ni and Al atoms, it is

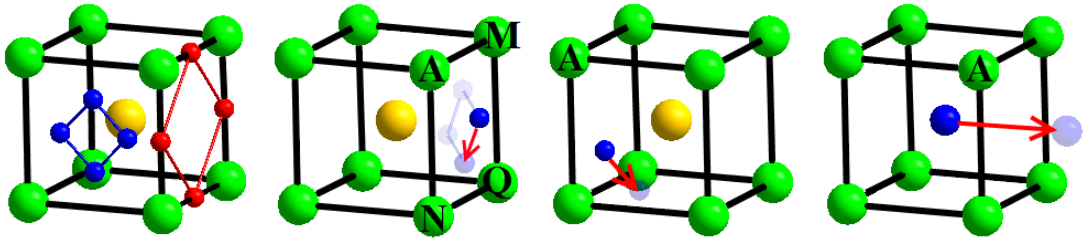

Figure 5.1: Stoichiometric NiAl; Al atoms occupy the corner sites (β-sites) and Ni atoms occupy the body-centered sites (α-sites), a) tetrahedral interstitial sites in blue and octahedral interstitial sites in red. b) Atom A represent the atom that is being substituted. Diffusion within a sublattice plane, 2NN to 2NN diffusion with respect to atom A c) 2NN to 3NN diffusion with respect to atom A (bonding away) d) NNN diffusion, NN to NN diffusion with respect to atom A.

S site	$\mathbf{E}_f$**(eV)**
$\mathbf{S}_t$ **(NiAl)**	3.95
$\mathbf{S}_o$**(NiAl)**	4.84
$\mathbf{S}_{Al}$**(NiAl)**	2.32
$\mathbf{S}_{Ni}$**(NiAl)**	2.48

Table 5.1: Formation energy of S containing NiAl alloys

proposed that S would prefer to occupy interstitial sites [38]. The formation energy of a NiAl alloy containing an S at the tetrahedral and octahedral interstices is calculated, and the tetrahedral-site is determined as the preferred interstice for an interstitial S atom (Table 5.1). Throughout this paper, for convenience, the atoms on the diffusion plane of S will be referred as $X_{A,M,N,Q}$ according to Figure 5.1(b).

5.2.1 Interstitial S diffusion

There are two different sublattice planes where an S atom can diffuse on: *i)* the Ni-sublattice plane (NSP) in which all atoms on the diffusion plane are Ni atoms and *ii)* the Al-sublattice plane (ASP). These two cases correspond to different sets of nearest neighbour configurations around S, and since interaction of S with its immediate surroundings plays a major role in determining the migration energy, its diffusion on NSP

and ASP, are modeled separately.

NSP jump

The interstitial S diffusion on NSP involves diffusion of an S atom from one tetragonal site, on top of a Ni-Ni bridge, to another as demonstrated in Figure 5.1. The variation of the total energy with displacement for this path, shown in Figure 5.2, reveals a symmetric MEP with a migration barrier of 0.036eV, and the calculation of vibrational frequencies result in a diffusion coefficient of $3x10^{-10}cm^2/s$.

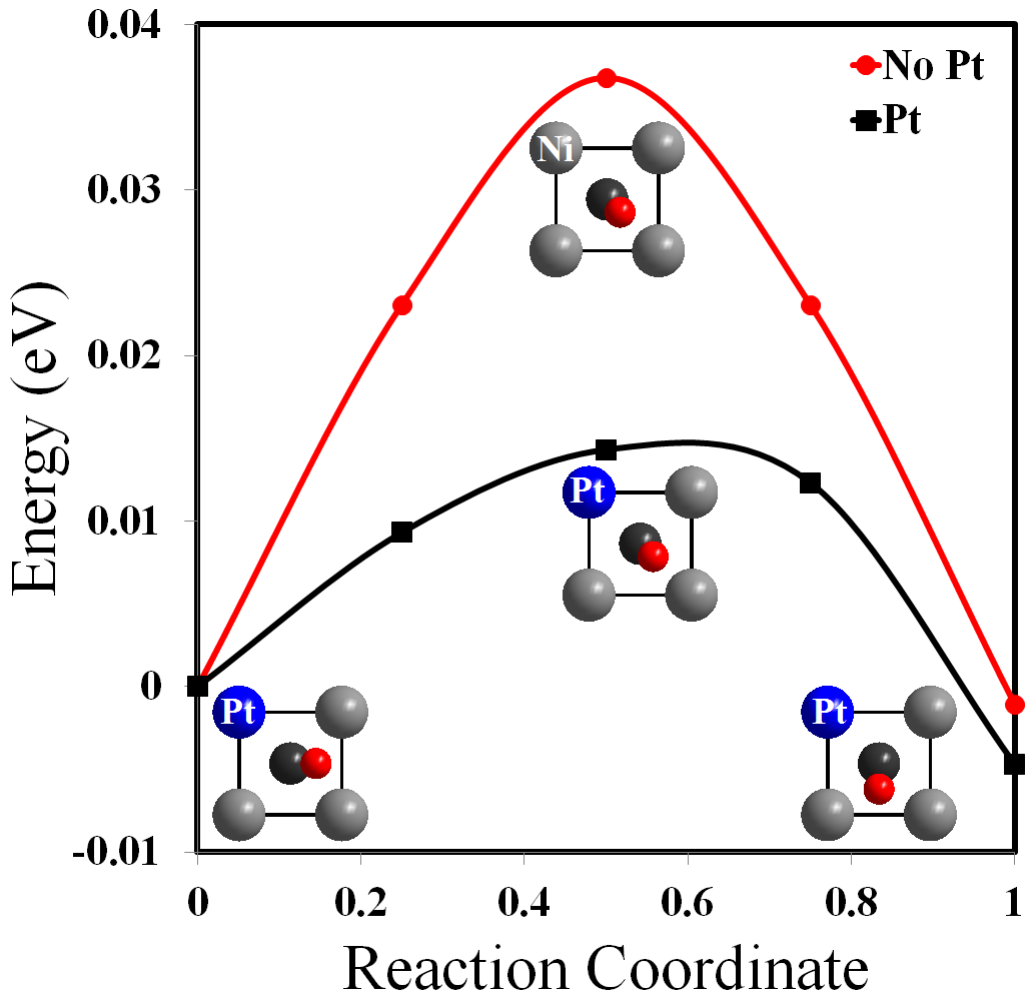

Figure 5.2: Red line is the MEP for S diffusion on NSP and black line is the MEP for S diffusion on NSP with a Pt atom. Blue, black, grey and red colors represent Pt, Al, Ni and S atoms respectively.

The ELF given in Figure 5.3 for the NSP jump reveals a weak Ni^A-S interaction, with S preferentially forming polar covalent bonds with two closest Ni atoms (Ni^M and Ni^Q). At the onset of diffusion, the electron localization between Ni^M and S begins to shift towards the S-Ni^N bond path, and at transition, it is equally distributed along Ni^M-S and Ni^N-S bonds. Changes in atomic separation signify a similar pattern (Table 5.2): Initially there are two groups of Ni-S separations with lengths 2.09 Å ($Ni^{M,Q}$) and 2.60 Å ($Ni^{N,A}$). At transition, Ni^M-S lengthens and Ni^N-S shortens to 2.27 Å while the other two do not undergo a substantial change. In addition, the weaker two of the initial four Al-S bonds elongate and possibly break during transition.

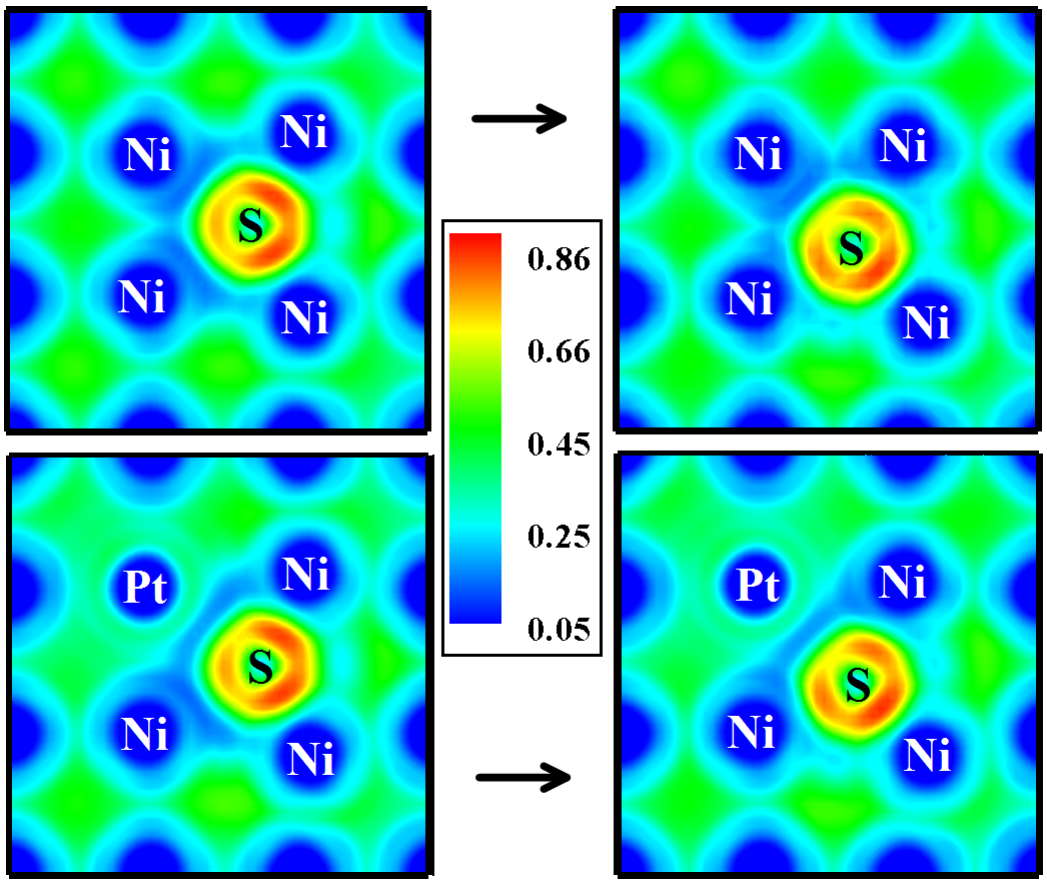

Figure 5.3: Initial and transition state ELF plots for S interstitial diffusion on NSP and NSP with a Pt atom.

ASP jump

Similar to an NSP jump, S hops from one tetrahedral site, on top of an Al-Al bridge, to another during its interstitial diffusion on ASP. As shown in Figure 5.1, the NEB calculations for ASP jump predicts a migration barrier of 0.27 eV, and the frequency calculations reveal a pre-exponential factor,D_o, of 3.4x10^{-9}cm^2/s.

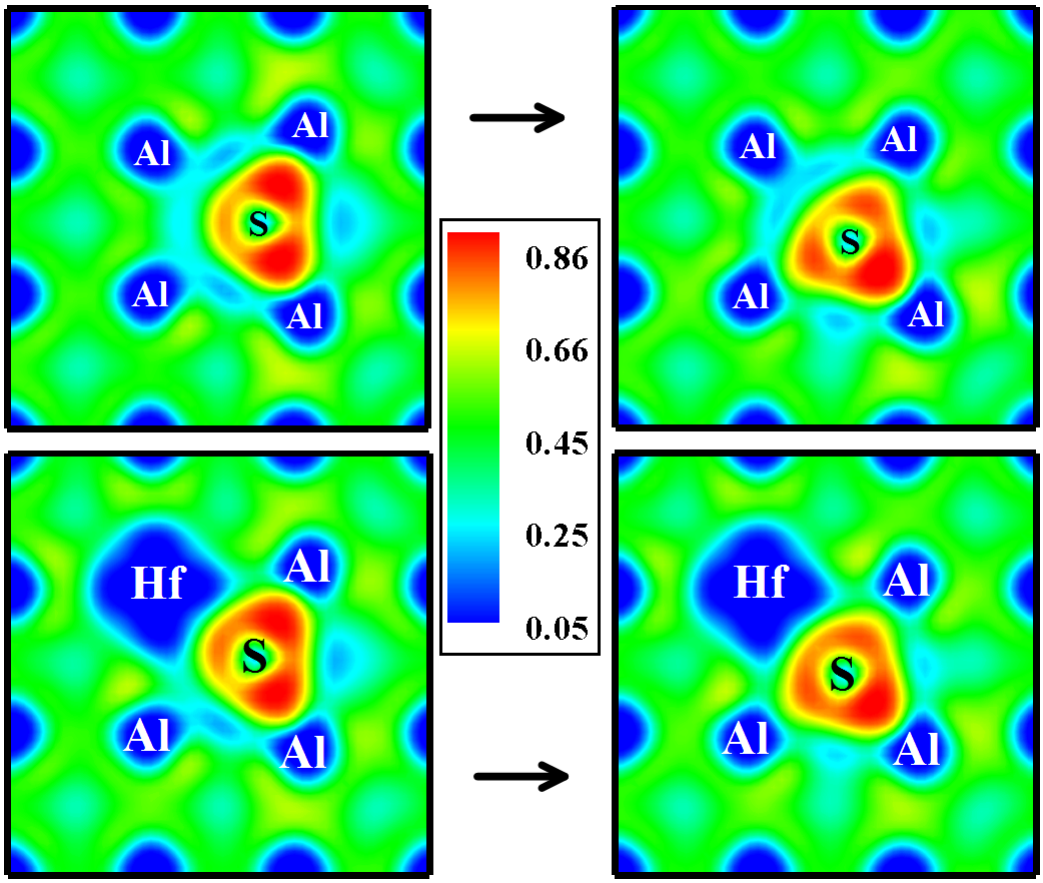

Figure 5.4: Initial and transition state ELF plots for S interstitial diffusion on ASP and ASP with a Hf atom.

A comparable trend to the NSP jump appears in the ELF for the ASP jump evinced in Figure 5.4. At transition, the pronounced electron localization between S and Al^M atoms becomes equally distributed along S-Al^M and S-Al^N bonds, while charge depletion in the form of a boomerang is detected between the Al^A and S. Furthermore, a prominent feature of Al-S bonds is the marked charge carrier localization, surpassing

Bond Type (Å)	**Diffusion Mechanism**						
	NSP(Pt)	**NSP**	**ASP(Hf)**	**ASP(Pt)**	**ASP**	**NNN(Pt)**	**NNN**
0.0:							
S-Ni	2.05, 2.10 2.72	2.09(x2) 2.60	2.10(x2) 2.72(x2)	2.05, 2.10 2.72	2.09(x2) 2.60(x2)	2.20, 2.31 2.37(x2) 2.61(x2)	2.27(x3) 2.81(x4)
S-Al	2.13(x2) 2.60(x2)	2.12(x2) 2.69(x2)	2.14(x2) 2.69	2.13(x2) 2.60(x2)	2.12(x2) 2.70	2.71(x2)	-
S-X	2.87 (Pt)	2.6(Ni)	2.48 (Hf)	2.87 (Pt)	2.70 (Al)	2.77(Pt)	2.27(Ni)
0.5:							
S-Ni	2.01, 2.29 2.32	2.04 2.27(x2)	2.06(x2)	2.05, 2.07 2.97, 2.98	2.06(x2)	2.09 2.20(x2)	2.17(x3)
S-Al	2.12(x2) 2.83(x2) 2.87(x2)	2.12(x2) 2.90(x2) 2.91(x2)	2.13 2.33(x2)	2.11, 2.28 2.34, 2.67	2.10 2.31(x2)	-	-
S-X	2.89(Pt)	2.67(Ni)	2.5(Hf)		2.69(Al)	2.50(Pt)	2.17(Ni)

Table 5.2: S-X separations

that of the Ni-S interaction which might be attributed to the greater electronegativity difference between Al and S atoms. Alteration of Al-S atomic separations from the initial to the transition state further supports the ELF observation (Table 5.2). S-Al^M elongates, S-Al^N shortens and S-Al^{Q,A} remains similar while two S-Ni bonds elongate to the breaking point at the transition state. The higher migration barrier compared to the NSP jump is possibly due to the stronger Al-S interaction.

Effects of Hf on S diffusion

In order to probe the effects of Hf atom on S diffusion, in an ASP one of the closest Al atoms to the interstitial S atom is replaced by an Hf atom, creating an initial Hf-

S separation of 1.6Å. Such a small separation caused an instability, and the S atom relaxed from on top of an Hf-Al bridge to the nearest tetrahedral site on top of an Al-Al bridge. Thus as a starting point, instead of the first nearest tetrahedral (NT) site to Hf, the S atom is placed at Hfs' second nearest tetrahedral (2NT) site, relaxing to an initial Hf-S separation of 2.47Å. Then, the S atom is diffused to another 2NT site of Hf. The calculated migration barrier for this path coupled with the pre-exponential factor derives a diffusion coefficient that is 10 times lower than D_S in pure NiAl, as depicted in Figure 5.5.

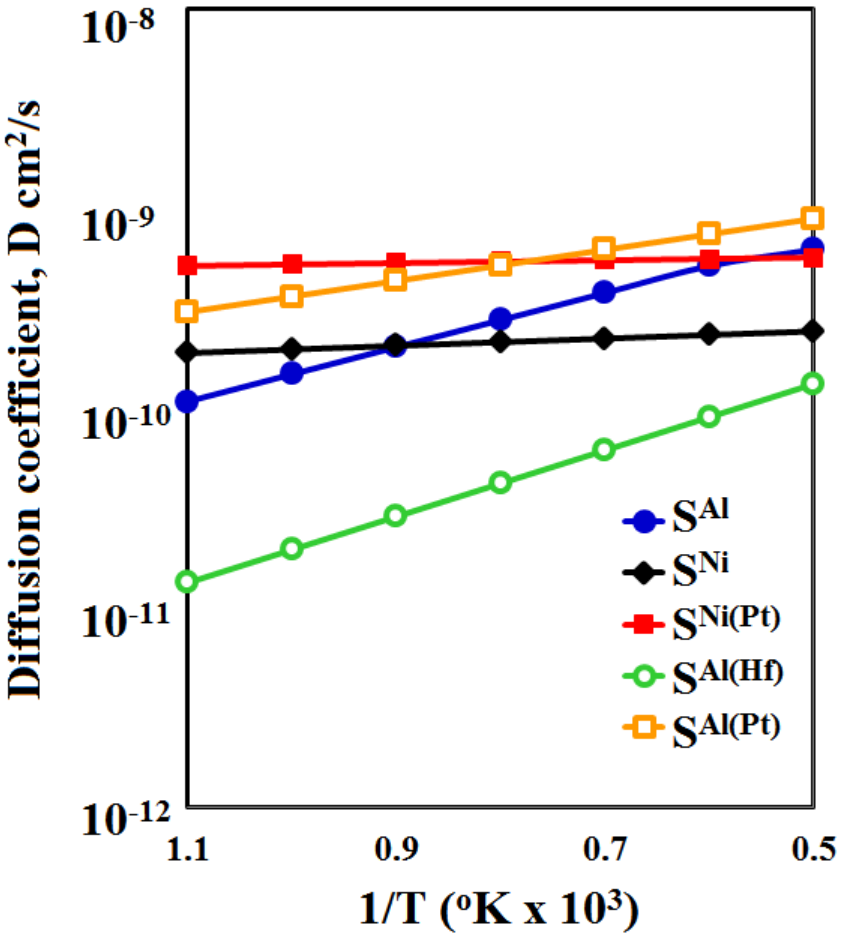

Figure 5.5: Diffusion coefficient vs $1/T(^oKx10^3)$ for S interstitial diffusion. The Diffusion coefficient axis given in log scale and the Temperature axis is inverted.

In addition to the previously observed strong $Al^{M(Q)}$-S bonds in pure NiAl, the ELF

plot for S diffusion in NiAl(Hf) displays additional electron localization (ELF>0.4) between Hf and S. During transition, similar to pure NiAl, transfer of electron population from the Al^M-S bond path to between Al^N and S atoms is detected, however, unlike Al^A-S, no electron depletion is spotted along the Hf-S bond path. When the atomic separations are compared with that of the pure ASP, all Al-S and the shortest Ni-S bond lengths remain comparable except for the Hf-S separation that is observed to be much shorter than the Al^A-S; a further evidence of a stronger interaction. Similarly, at the transition state, two Ni-S bonds break while Al^N-S bonds get shorter and Al^M-S bonds elongate in accordance with the charge transfer as observed in the ELF plot.

In order to further observe the extent of Hf-S interaction and identify the gettering ability of Hf, a model is created examining the diffusion of an S atom from the 2NT to 3NT site of Hf as depicted in Figure 5.1. However, after initial relaxations of the end configuration, S relaxed to the 2NT site of Hf, demonstrating that the structure with the S atom at the 3NT site of Hf is not stable because of the strong Hf-S attraction. Such strong interaction proves the gettering ability of Hf and explains the reduced S concentration at the oxide/bond coat interface. Thus it can be concluded that the overall reduction in diffusion rate of S is governed by the strong Hf-S interaction.

Effects of Pt on S diffusion

One of the possible *positive effects* of Pt is its ability to stop S from diffusing to the oxide/bond coat interface. To verify this proposition, a nearest neighbour Ni atom to S on a NSP is replaced by a Pt atom. However this initial configuration is proven unstable due to the Pt-S interaction that caused the S atom to displace towards the 2NT site of Pt, increasing the Pt-S separation to 2.86 Å. Thus diffusion of S from a 2NT to another 2NT and to a 3NT site is calculated to thoroughly elucidate the effects of Pt on S diffusion.

The results given in Table 5.3 clearly demonstrate that the addition of Pt accelerates

the interstitial S diffusion in NiAl. For the 2NT-2NT diffusion path, the symmetric MEP reveals a migration barrier of 0.014eV that is lower compared to the migration barrier for a pure NSP jump as shown in Figure 5.2. Combined with the pre-exponential factor of $6.2x10^{-10}$ the resulting diffusion coefficient for S in the proximity of a Pt atom is greater for the whole temperature range as depicted in the Arrhenius plot Figure 5.5.

From the ELF figure, no increased electron localization is observed between Pt and S, on the contrary, Pt repels the S atom, causing it to displace towards Ni^Q. As the S atom diffuses to its saddle point, the electron localization between Ni^M and S gets weaker concurrent with the increased carrier population between Ni^N and S atoms, while any localization indicating a positive interaction between Pt and S still cannot be determined. The atomic separation supports the ELF observations: At the initial configuration, Pt repels (Figure 5.3) the S atom, increasing their atomic separation to 2.87Å compared to the Ni^A-S bond length of 2.6Åin pure NSP-jump. Once the diffusion initiates, at the midpoint of the path, S displaces towards Ni^N, without changing its separation with Pt.

A similar conclusion is drawn for the S diffusion from a 2NT to a 3NT site of Pt, which is to be compared with an ASP jump. As depicted in Figure 5.1(c), one of the Ni atoms in the NSP is replaced with a Pt atom, and the S atom is made to segregate away, on an ASP. Figure 5.6 illustrates the asymmetric MEP with the low migration barrier that is a consequence of the repulsive Pt-S interaction, and Figure 5.5 displays the overall diffusion coefficient which is higher than D_S^{ASP} over the full temperature range. Even though such a diffusion path is unsymmetric and may not be stable, it is studied for comparison purposes with the S diffusion from Hfs' 2NT to 3NT site.

Due to its greater electronegativity, Pt is proposed to gain an electron from its surrounding Ni and Al atoms, and become an anion creating repulsive Ni-Pt and Al-Pt interactions [55]. In line with this observation, there is a repulsive interaction between the Pt and S anions, that is evident from the ELF plots for both the NSP(Pt) and

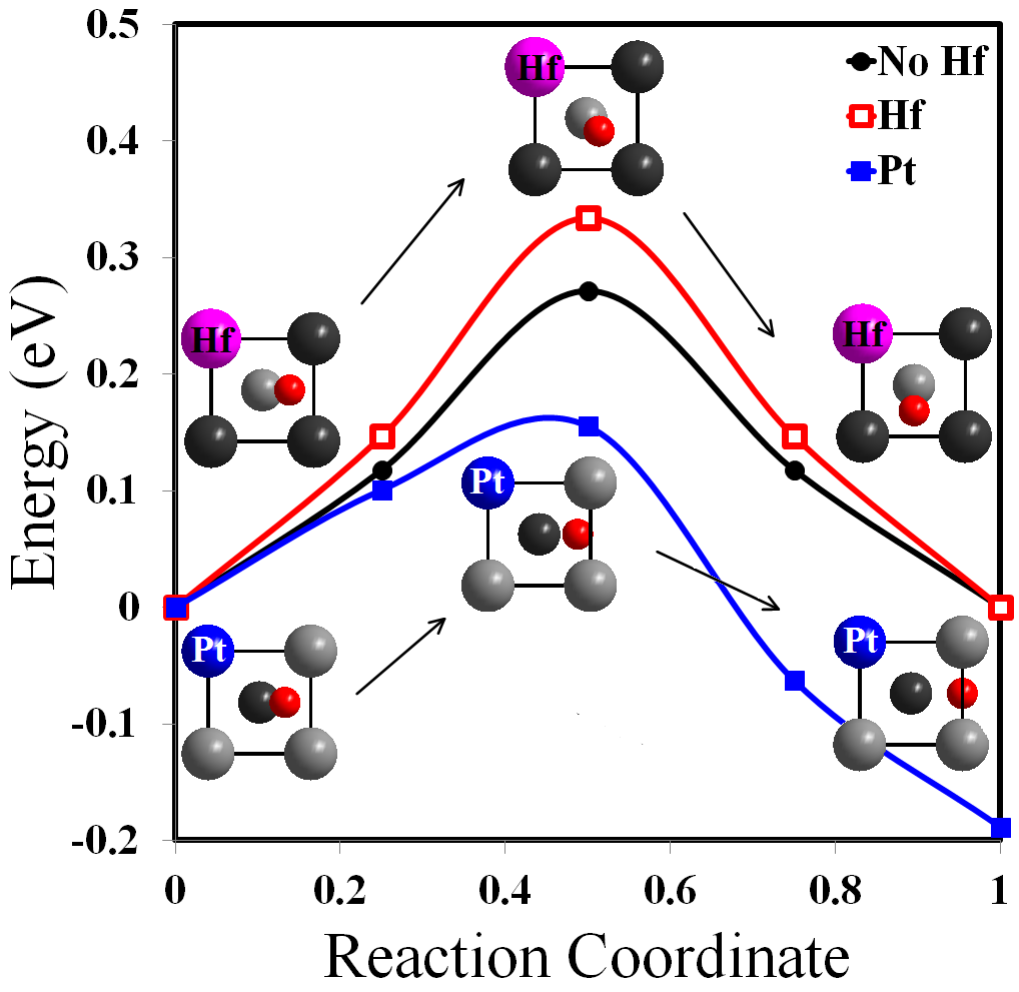

Figure 5.6: Black line is the MEP for S diffusion on ASP, blue line is the MEP for S diffusion away from a Pt atom on an ASP, and red line is the MEP for S diffusion on ASP containing a Hf atom. Blue, black, grey, pink and red colors represent Pt, Al, Ni, Hf and S atoms respectively.

the ASP(Pt) jumps. The interstitial configuration dictates short Pt-S separation that allows the repulsive behaviour, consequently accelerating the S diffusion in the vicinity of Pt.

As expected, our calculations predict a reduced S diffusion rate in Hf doped NiAl alloys. Owing to its gettering ability, Hf forms stronger bonds with S compared to the Al atom that it has replaced, and stops S from diffusing away by reducing the S diffusion rate as long as they interact. However surprisingly, Pt is determined to speed

	$\mathbf{E}_m$**(eV)**	$\mathbf{E}_f$**(eV)**	**Q(eV)**	$\mathbf{D}_o$**(cm2/s)**
NiAl (Ni-Plane)	0.036	-	0.036	$3x10^{-10}$
Ni(Pt)Al	0.014	-	0.014	$6.2x10^{-10}$
NiAl (Al-plane)	0.27	-	0.27	$3.4x10^{-9}$
NiAl(Hf)	0.33	-	0.33	$8.6x10^{-9}$
Ni(Pt)Al - away	0.155	-	0.155	$2.2x10^{-9}$
NiAl - NNN	0.48	1.25	1.73	$0.15x10^{-1}$
Ni(Pt)Al -NNN	0.68	1.20	1.88	$0.95x10^{-2}$
NiAl[1]			2.26	1.5
NiAl[2]			2.91	8.4
Ni(Pt)Al[3]			0.41	$2.5x10^{-10}$

Table 5.3: Migration, formation, activation energy and the pre-exponential factor for all types of S diffusion.

up the S diffusion since it repels and does not form a bond with S, unlike the Ni atom that it has substituted. Finally, the calculated activation energies (0.036 eV and 0.27 eV) and the pre-exponential factors for jumps on pure NSP and ASP are found much lower than the experimentally obtained values for S diffusion in NiAl [38, 94]. Such a difference between the calculated and the experimental data is likely an indication that S diffuses via a different mechanism in NiAl. To ensure its most favourable diffusion mechanism, the vacancy mediated S diffusion in NiAl is further examined.

5.2.2 Vacancy mediated S diffusion

At higher temperatures, deviations from the ideal NiAl structure are observed due to formation of point defects in NiAl alloy. Vacancies and antisite atoms constitute these point defects: A vacancy is the absence of an atom on its sublattice that is denoted as V_{Ni} and V_{Al} for Ni and Al vacancies, respectively, and an antisite atom forms when a Ni(Al) atom resides on an Al(Ni)-site symbolized by $Ni_{Al}(Al_{Ni})$.

In order to determine the most favourable substitutional site of S, the formation energy of NiAl containing an S atom substituting a Ni or an Al atom is calculated independently. As given in Table 5.1, formation of an S atom at an Al site is found

more favourable. Thus as the vacancy mediated diffusion, a symmetric next nearest neighbour (NNN) jump for S in which the S atom jumps from one Al sublattice site to another is considered.

NNN S diffusion in NiAl

The NEB calculation for the NNN S jump in NiAl predicts a migration barrier of 0.48eV. The resulting activation energy of 1.73eV is much closer to the experimentally reported value (2.26eV) by Rivoaland *et. al.* [38], compared to the activation energies obtained for its interstitial diffusion. Combining the calculated pre-exponential factor with the activation energy in Eq. 3.28, yields the following expression for NNN S diffusion:

$$D_S^{NNN} = 0.015\ x\exp\left(-\frac{1.73}{k_B T}\right)\ (cm^2/s) \tag{5.1}$$

The diffusion coefficient given in Eq. 5.1 is presented in Figure 5.7. At 1000^oC, it is calculated as $2x10^{-9}cm^2/s$ which is in very good agreement with recent experimental data of $1x10^{-9}cm^2/s$ ref. [93].

At the initial state, after relaxations, the S atom is displaced towards four Ni atoms neighbouring the vacancy, as seen in Figure 5.8. During transition, S is equidistant from these four Ni atoms, forming equal bonds, as determined from the electron localization between S-Ni's. In agreement with the information gathered from ELF, atomic separations also suggest displacement of S towards the vacancy, reducing four Ni-S separations to 2.27Å and increasing the other four to 2.81Å from the unrelaxed Ni-S separations of 2.5Å. During transition, the shortest four Ni-S bond lengths reduce to 2.17Å while the other four break off. At any stage during the segregation of S, no bond formation between S and any Al atom is observed.

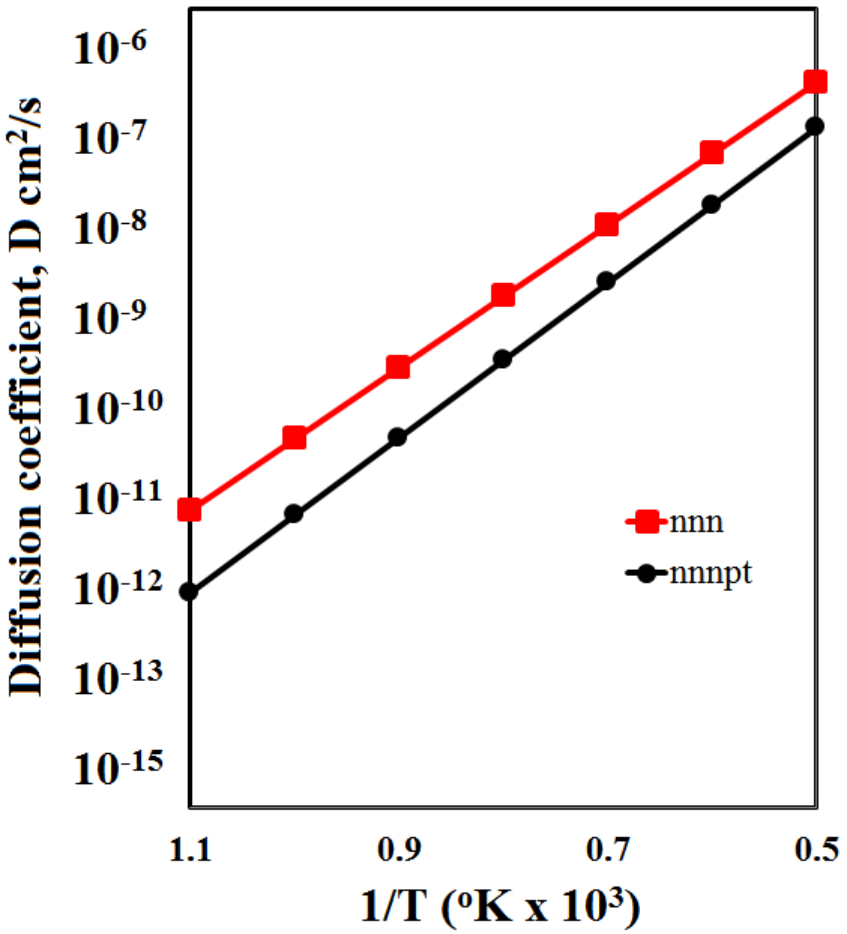

Figure 5.7: Diffusion coefficient vs 1/T($^oKx10^3$) for S vacancy diffusion. The Diffusion coefficient axis given in log scale and the Temperature axis is inverted.

NNN S diffusion in Ni(Pt)Al

In order to observe the effects of Pt on NNN S diffusion, the Ni atom (denoted by Ni^A) which is a nearest neighbour to both S_{Al} and V_{Al} is replaced by Pt. Presence of Pt increases the overall activation energy by 0.15eV and slightly decreases the pre-exponential factor (Table 5.3) leading to a diffusion coefficient:

$$D_S^{NNN(Pt)} = 0.0095\ x\exp\left(-\frac{1.88}{k_BT}\right)\ (cm^2/s) \tag{5.2}$$

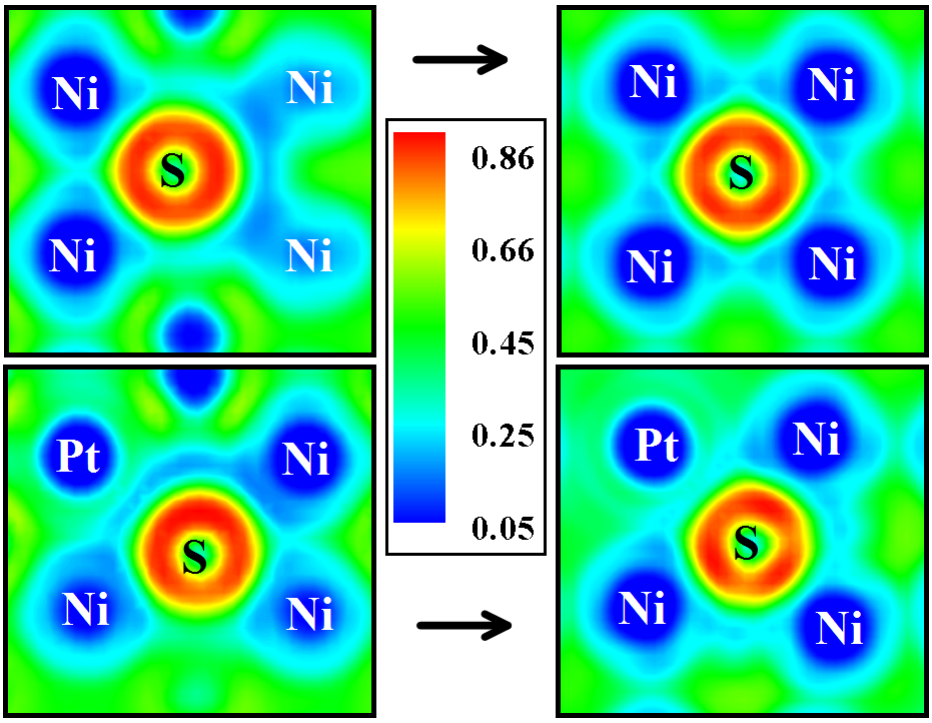

Figure 5.8: Initial and transition state ELF plots for S NNN diffusion in NiAl and Ni(Pt)Al.

The higher activation energy, combined with a lower pre-exponential factor slows down the S diffusion as shown in the Arrhenius plot given in Figure 5.7.

At the initial state, due to the presence of Pt in between the S atom and the vacancy, from the ELF plot given in Figure 5.8, one can see that S does not relax towards the vacancy, and instead, it displaces away from Pt. Such escape behaviour and electron delocalization suggest an initial repulsion between these atoms. At the saddle point, the S atom diffuses through the Ni-plane that contains the Pt atom. It displaces away from Pt towards the opposite Ni atom, disrupting the order at this layer. Even though there is a general repulsive behaviour between Pt and S, the increased electron localization at the transition state in between these atoms can be indicative of a weak S-Pt interaction.

S relaxes away from Pt, elongating its separation from 2.27Å to 2.77Å compared to Ni^{A}-S bond. Due this asymmetric configuration, one of the Ni-S bonds does not form and two additional Al-S bonds with lengths 2.71Åare observed as given in Table 5.2. At the saddle point, the two additional Al-S and three Ni-S bonds get broken off and

the Pt-S bond remains greater compared to its counterpart, Ni^A-S bond in pure NiAl. It can be concluded that the increased migration barrier is due to the repulsive Pt-S interaction since S is diffusing through a Pt containing plane. In this research NNN S diffusion away from Pt is not considered, since this path is not symmetric and at the end point of the S diffusion path, there is no Pt-S interaction due to their greater separation.

At lower temperatures a smaller defect concentration is expected. As temperatures get higher, formation of vacancies and antisite defects become more plausible. Thus, it can be suggested that at lower temperatures S diffuses as an interstitial whereas for high temperatures in which there are enough vacancies for vacancy mediated diffusion, a NNN jump is preferred. This phenomenon is rationalized looking at the Arrhenius plot given in Figure 5.9. At lower temperatures, the S interstitial diffusion coefficient is higher while at temperatures above 840^oC vacancy mediated NNN diffusion is favoured. Such an observation also implies that at lower temperatures Pt would increase the S diffusion rate while at higher temperatures it would slow it down. This conclusion is consistent with the experimental observation made for S diffusion in NiAl which proposed that Pt would increase the S diffusion rate in NiAl at low temperatures and reduce it at temperatures higher than 900^oC [94].

5.3 Conclusion

DFT calculations have been performed to study S diffusion in NiAl to determine the effects of Hf and Pt on the S diffusion rate. Two mechanisms: interstitial and vacancy mediated, have been examined. The S diffusion rate is found to be over three orders of magnitude greater than Ni self diffusion in NiAl. At temperatures below 840^oC, interstitial S diffusion is determined to be preferred over vacancy mediated diffusion whereas above 840^oC the NNN diffusion is favoured.

Hf is known to getter S and form compounds within bulk NiAl, reducing the S concentration at the interface [60, 67]. In agreement, the NEB calculations combined with the harmonic transition state theory predicted that Hf strongly interacts with S, keeping it from diffusing away towards the oxide/bond coat interface. The influence of Pt on S is observed to be mechanism dependent: It accelerates the interstitial S diffusion, which is found to be preferred below 840^oC and reduces the NNN diffusion rate that is shown to be dominant for temperature over 840^oC. Such a conclusion agrees well with experimental observation stating that Pt accelerates S diffusion below 900^o and decelerates it above that temperature [94]. As a final remark, the ELF figures and the atomic separations showed that S atoms do not prefer to be in close proximity to Pt which explains the reduced S concentration at the metal/oxide interface after Pt segregation to the NiAl surface at the oxide/bond coat interface.

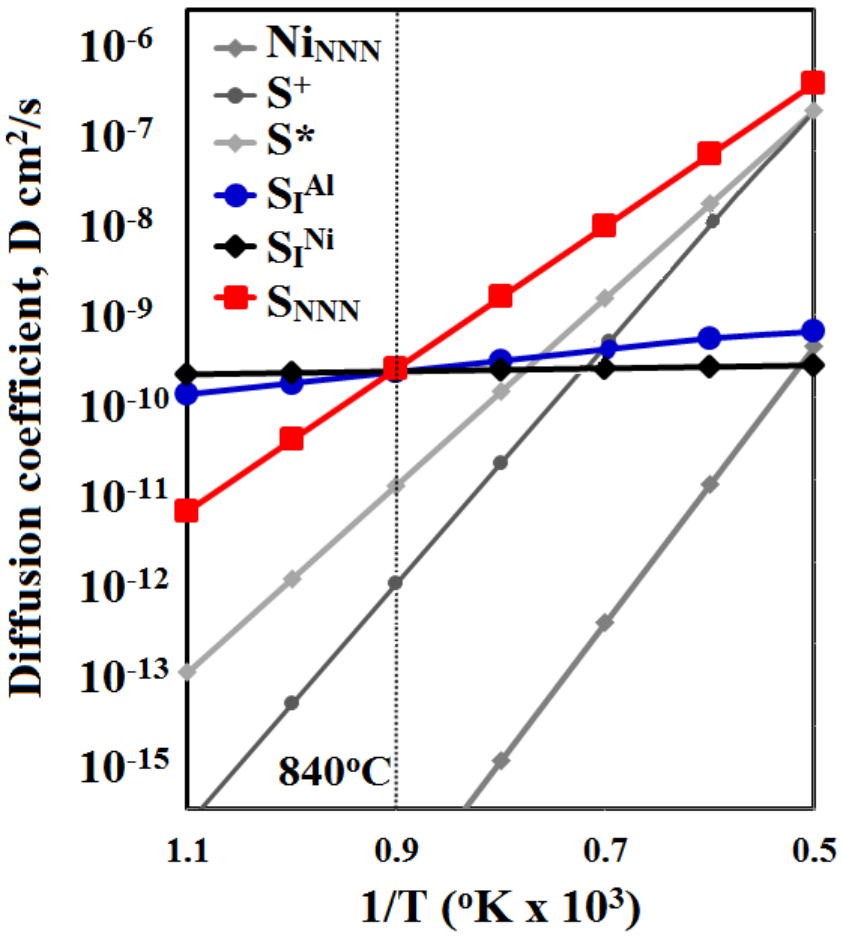

Figure 5.9: A comparison of diffusion coefficient vs 1/T($^oKx10^3$) of interstitial and vacancy mediated S diffusion. The Diffusion coefficient axis given in log scale and the Temperature axis is inverted. S* is the diffusion data obtained by ref. [38] and S^+ is the diffusion data obtained by ref. [94]. The diffusion data provided for NNN Ni diffusion is obtained through DFT calculations

Chapter 6

Investigation of the Effects of Reactive Elements on Σ3 $10\bar{1}0$ twin Al_2O_3 Grain Boundary Sliding and Cleavage: an *Ab initio* Study

6.1 Introduction and Theory

Even though, previously, addition of REs to the Σ11 is shown to improve the sliding barrier, and addition of Y to the Σ3 GB is predicted to improve its tensile strength, no calculation has been carried out studying both the cleavage and sliding mechanisms and assessing the effects of REs on brittleness of Al_2O_3 GBs. In the present work, DFT calculations are employed with a purpose of clarifying the atomic level mechanisms during the sliding and the cleavage fracture of the pure and doped alumina grain boundaries. The change in the sliding barrier and maximum stresses are assessed in the Hf, Zr and Y doped Σ3 $(10\bar{1}0)$ twin Al_2O_3 GB since Hf, Y and Zr are commonly found in bond coats in TBCs and segregate to the alumina grain boundaries from the bond coat. In addition, the ductile and brittle behaviour of these grain boundaries are assessed by using the cleavage and stacking fault energies. Results found in this research will provide a microscopic level insight on the effects of quadrivalent segregants Hf, Zr and trivalent Y on the mechanical properties of Σ3 alumina grain boundary.

Spin-polarized density functional theory (DFT) is employed using the Vienna *Ab initio* simulation package (VASP) with a plane-wave basis set [118]. The Perdew-Wang generalized gradient approximation (GGA) is used to calculate the electron exchange and correlation energy [127] and the projector augmented wave (PAW) potentials are used to describe the interactions of valence electrons with the ion and core electrons for all elements in Hf-doped, Zr-doped and the clean grain boundary structures, while the US-GGA potentials are utilized for the elements of Y-doped structure [137]. The Al $3s^2 3p^1$, Hf $6s^2 5d^2$, Zr $5s^2 4d^2$, O $2s^2 2p^4$ and Y $5s^2 4d^1$ electrons are treated as valence.

The Brillouin zone integration is performed using a gamma point centered 5x3x1 Monkhorst Pack grid that yields 6 irreducible k-points [165]. The occupation of electronic states is determined according to first order Methfessel-Paxton scheme with a smearing width of 0.2eV. A kinetic energy cutoff of 350eV is used for all calculations. The atomic positions are allowed to relax until the forces on the ions are less than the threshold of 0.01eV/Å. To examine the relationship between the electronic structure and sliding, cleavage properties, the electron localization function (ELF) is calculated.

The corundum Al_2O_3 is modeled using 120 atoms that are composed of 48 Al and 72 O atoms. An orthorhombic supercell, defined by the lattice vectors $\boldsymbol{e_1} = [\bar{1}2\bar{1}0]$, $\boldsymbol{e_2} = [0001]$, $\boldsymbol{e_3} = [10\bar{1}0]$ are used to represent the structure. The $\Sigma 3$ Al_2O_3 GB is constructed by rotating one half of the corundum Al_2O_3 180^o around $[10\bar{1}0]$ axis with respect to the other half of the structure, generating a mirror symmetric grain boundary. Following Fabris *et. al.* different rigid body translations are applied to the structure to find the energetically most stable translation of the system, and in agreement, the screw rotation twin is found to be the most stable translational variant corresponding to a translation of $\boldsymbol{T} = \frac{1}{2}\boldsymbol{e_1} + \frac{1}{3}\boldsymbol{e_2}$ [99]. The $\Sigma 3$ Al_2O_3 supercell that has two grains with an orientation relation $\left(10\bar{1}0\right)||(10\bar{1}0)$ and $\left[\bar{1}2\bar{1}0\right]||[1\bar{2}10]$ is shown in Figure 6.1, viewed along the $\left[\bar{1}2\bar{1}0\right]$ direction. The periodic repetitions of the structure along the z-axis are separated by 12Å of vacuum to eliminate interactions between

periodic cells. After relaxations, the dimensions of the supercell is found as a=4.76Å, b=13.03Å, c=24.74Å with a grain boundary area of 62.02Å^2.

Shear stresses are modeled by displacing one grain with respect to another with increments of $\%5|\boldsymbol{e_2}|$ along the full $\boldsymbol{e_2}$ axis. Around the highest energy point finer translations of $\%2|\boldsymbol{e_2}|$ are applied to confirm the highest energy barrier. After each rigid translation, the 30 atom in the vicinity of the grain boundary are allowed to fully relax in all directions until the forces on each are less than 0.01eV/Å. The rest of the supercell remains fixed to mimic a bulk-like Al_2O_3 in order to ensure that the structure does not relax to its global minimum [111]. The energy required to dislocate such two grains with increments of d is called the generalized stacking fault energy $\gamma_{GSF}(x)$ where the point that the energy reaches its maximum is termed the maximum generalized stacking fault energy and symbolized as $\gamma_{\mu s}$. The calculated energies for each increment along the path is scaled relative to the global minimum of the $\gamma_{GSF}(x)$.

The cleavage process is modeled by rigidly cleaving two grains by fractions (f) of the initial grain separation d_0. After each level of separation ($x = fd_0$), two different calculations are carried out: 1) The atoms are allowed to relax in the cleavage direction only (here referred to as r1 model) and, 2) All atomic positions are allowed to relax in 3 dimensions (here referred to as r3 model) until the forces are less than the threshold value. Unlike the sliding process, the atoms further away from the grain boundary region are also allowed to relax. The energy released during the cleavage process is called the decohesion energy $G(x)$, and is described as a function of the interface separation x. For large separations, if the decohesion energy approaches the cleavage energy, G_C which is defied in the limit $G(x)_{x\to\infty} = G_c$, the material cleavages. To obtain the cleavage energy within this limit, an interface separation up to $10d_0$ is applied between the grains, and a 7x3x1 grid that leads to 7 irreducible k-points is utilized for a better accuracy.

Three different approaches are utilized to determine the critical cleavage stress (σ_c)

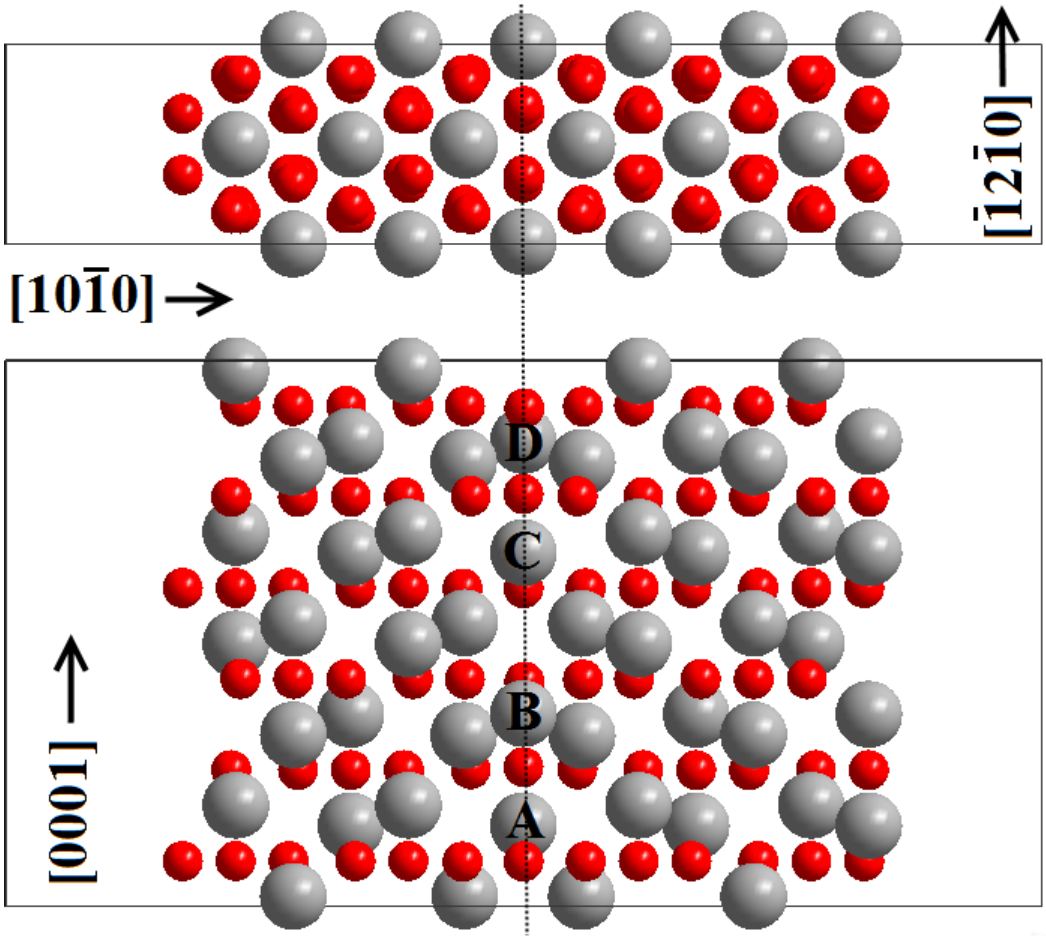

Figure 6.1: Model of the $\Sigma 3$ Al_2O_3 grain boundary viewed along [$\bar{1}2\bar{1}0$] (below) and towards the [0001] (above) direction.

such as: 1) Calculating $dG(l_c)/dx$ of the famous UBER fit, 2) For relaxed processes, fitting the equation defined by Ref. [155] for the decohesion energy and using the slope of these fits at $x = l_c$ or 3) From its definition; calculating the maximum value of the slope of energy-separation curve itself [160, 161, 164, 170, 171]. With the purpose of predicting the mechanical behaviour of the materials under study, ductility conditions and parameters D, and A provided in chapter 3 are examined. However, since in this study the Schmid factor, S, in parameter A is zero, only D is evaluated as the ductility parameter.

In all calculations a single dopant R (R=Y, Hf, Zr) is substituted for an Al atom

	Al	**Hf**	**Zr**	**Y**
$\gamma_{\mu\mathbf{s}}(\mathbf{J/m^2})$	3.85	4.14	3.94	4.12
$\tau_{\mathbf{c}}(\mathbf{G}Pa)$	27.45	30.86	28.79	32.455
$\mathbf{G_c}(\mathbf{J/m^2})$	3.84	4.03	3.98	5.29
$\sigma^*_{\mathbf{c}}(\mathbf{G}Pa)$	36.29	37.83	34.59	47.24
$\sigma_{\mathbf{c}}(\mathbf{G}Pa)$	32.47	40.18	40.57	40.52
D	0.99	0.97	1.35	1.28

Table 6.1: Sliding energy $\gamma_{\mu s}$, cleavage energy G_c, maximum sliding stress τ_c, maximum cleavage stress σ_c, cleavage stress fit $\sigma*_c$ and the ductility parameter D for the clean and Hf, Zr, Y added GBs.

at the grain boundary since previously Y is determined to segregate to Al_2O_3 grain boundaries with a concentration of 2-5Y atoms/nm^2, and substitute for an Al atom [102, 172]. In order to determine their energetically favourable substitutional site, the dopant R atom is doped into A, B, C, D aluminum sites that are identified in Figure 6.1, and then the grain boundary is allowed to fully relax in all directions. For all dopants, the A substitutional site is found the most favourable in agreement with previous computational studies [102]. Once the preferred substitutional site is determined, for all RE-doped grain boundaries, the same relaxation steps as in the undoped grain boundary are applied for sliding and cleavage calculations. For convenience, the undoped grain boundary is symbolized as Al_{GB}, and the Hf_{GB}, Zr_{GB} and Y_{GB} represent the Hf, Zr and Y substituted grain boundaries, respectively.

6.2 Results and Discussion

The grain boundary energy (E_{int}), defined as the energy difference between the bulk alumina (E_{bulk}) and the $\Sigma 3$ grain boundary model (E_{GB}):

$$E_{int} = \frac{E_{GB} - E_{bulk}}{Area} \tag{6.1}$$

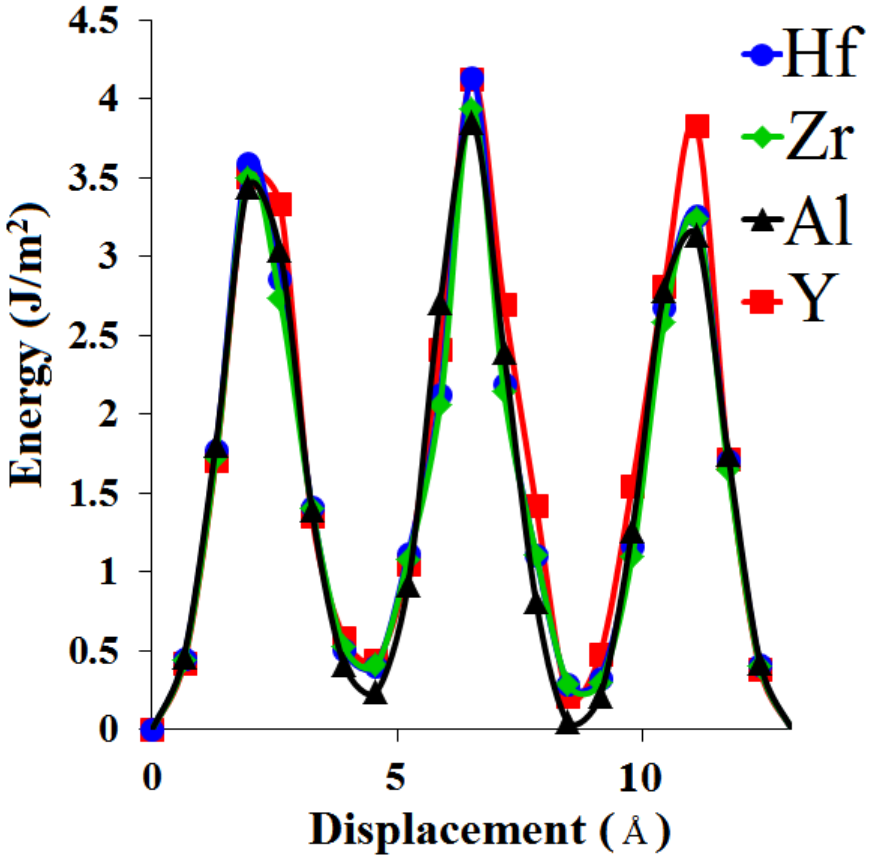

Figure 6.2: Sliding profiles for all grain boundaries.

is calculated as $0.27 J/m^2$, concurrent with previously calculated values of $0.3 J/m^2$ and $0.42 J/m^2$ for the same grain boundary [99, 102]. The interfacial Al atoms in this highly ordered structure are six fold coordinated, identical to the Al atoms in bulk oxide, Figure 6.1. As a result, the main change in bonding characteristics and coordination number stems from the oxygen atoms: While in the bulk oxide, the oxygen atoms are fourfold coordinated, the coordination number of the interfacial oxygen atoms in the $\Sigma 3$ GB varies between three, four and five fold. In addition to altered coordination of oxygen atoms, in agreement with previous calculations, the interface O-Al bonds stretch or contract with new bond lengths ranging from 1.76Å to 2.18Å [99, 102].

6.2.1 Sliding

The GB energy profile relative to displacement for each structure is given in Figure 6.2. For all cases a sliding barrier corresponding to a 50% displacement ($0.5|\boldsymbol{e_2}|$), and two satellite barriers on both sides of the main sliding barrier, at 15% and 85% of the total displacement, are determined. The sliding barrier of $3.85J/m^2$ predicted for the Al_{GB} is consistent with previously calculated sliding barriers of, $4.71J/m^2$ ad $3.23J/m^2$ for the $\Sigma13$ $[1\bar{2}10]$ and $\Sigma11$ Al_2O_3 grain boundaries [111, 117]. Even though, due to its highly ordered structure, the sliding barrier for the $\Sigma3$ GB is expected to be much higher compared to $\Sigma13$, such a discrepancy can be a result of dissimilar relaxation techniques used [111].

The energy barrier for sliding in RE_{GB}'s are predicted as, $4.14J/m^2$, $3.94J/m^2$ and $4.12J/m^2$ for Hf_{GB}, Zr_{GB} and Y_{GB}, respectively (Table 6.1). Comparison of atomic separations across the interface at $0|\boldsymbol{e_2}|$ and $0.5|\boldsymbol{e_2}|$ for these structures along with Al_{GB} are given in Table 6.2. In all cases at $0.5|\boldsymbol{e_2}|$, the number of Al-O and O-Al bonds are reduced, where the Al-O is referred to the bonds formed by interface Al atoms with their surrounding O, while the O-Al are the bonds formed by the interface O atoms with their surrounding Al. In Al_{GB}, the Al_C and Al_A atoms become fivefold coordinated whereas in RE_{GB}'s, instead of the RE that substituted for Al_A, the Al_B atom undergoes a change in coordination number and becomes fivefold coordinated. In addition, at $0.5|\boldsymbol{e_2}|$, unlike in Al_{GB} where the average Al-O separation for the Al_B and Al_D atoms shortens, in RE_{GB}'s the average RE-O and Al_D-O bonds lengthen.

The expected chemical bond length for covalent O-O single and O=O double bonds are 1.47Å and 1.21Å, respectively. However at $0.5|\boldsymbol{e_2}|$ the minimum O-O separations (2.1Å) given in Table 6.2 are much greater than the expected bond lengths. This is a clear indication that there is no covalent bond formation between these atoms. In fact such a separation suggests that these negatively charged O atoms repel each

X:	**Al**		**Hf**		**Zr**		**Y**	
(Å,#):	$0\|\boldsymbol{e_2}\|$	$0.5\|\boldsymbol{e_2}\|$	$0\|\boldsymbol{e_2}\|$	$0.5\|\boldsymbol{e_2}\|$	$0\|\boldsymbol{e_2}\|$	$0.5\|\boldsymbol{e_2}\|$	$0\|\boldsymbol{e_2}\|$	$0.5\|\boldsymbol{e_2}\|$
Al_D-	1.93	1.91	1.89	1.91	1.89	1.90	1.89	1.90
O	(6)	(6)	(6)	(6)	(6)	(6)	(6)	(6)
Al_C-O	1.91	1.85	1.92	1.84	1.92	1.83	1.93	1.84
	(6)	(5)	(6)	(5)	(6)	(5)	(6)	(5)
Al_B-O	1.93	1.91	1.92	1.87	1.92	1.88	1.91	1.89
	(6)	(6)	(6)	(5)	(6)	(5)	(6)	(5)
X_A-O	1.91	1.85	2.04	2.09	2.06	2.08	2.16	2.21
	(6)	(5)	(6)	(6)	(6)	(6)	(6)	(6)
O-Al	1.93	1.90	1.94	1.93	1.95	1.92	1.95	1.94
	(24)	(22)	(24)	(22)	(24)	(22)	(24)	(22)
O-O	(-)	2.1	(-)	2.08	(-)	2.1	(-)	2.1

Table 6.2: Average bond lengths in a sliding process. A,B,C,D refers to atoms specified in figure 1. The numbers in parenthesis specifies the number of bonds.

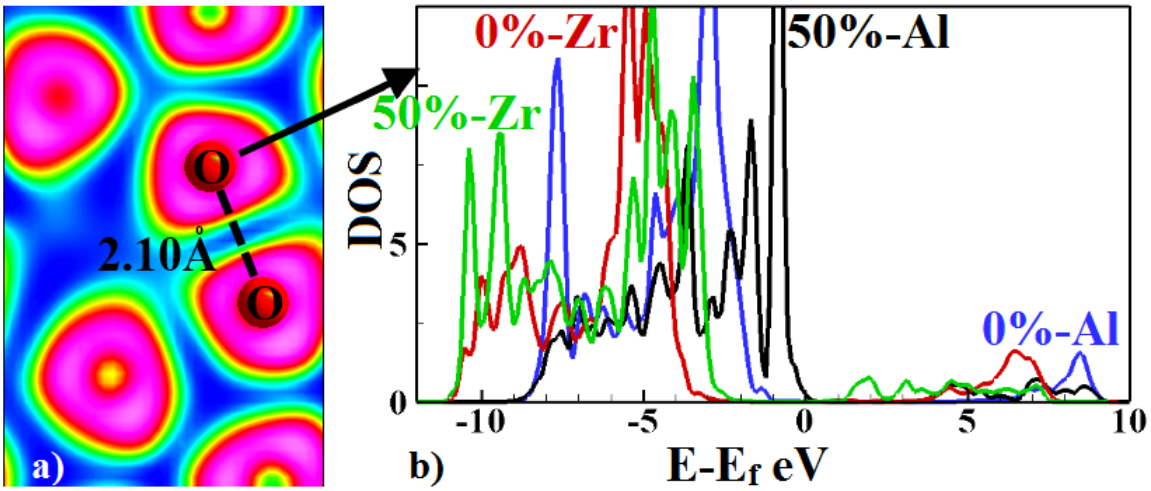

Figure 6.3: a) 50%$\boldsymbol{e_2}$ ELF for Al_{GB}, cut through one of the shortest O-O separation b)DOS of O p-orbitals at 0% and 50% displacement for Al_{GB} and Zr_{GB}.

other with an effective atomic diameter of 2.1Å [173]. This interesting occurrence is also noticeable from the ELF and DOS plots given in Figure 6.3. From the ELF, the circular electron clouds on O atoms are observed to deform and lose their rounded shape along the path of their separation, and from DOS, the broadening of the O p-DOS at $0.5|\boldsymbol{e_2}|$ can be determined. The same figure also reveals a downward shift (away from the Fermi level) in O p-states after Zr addition, indicating a greater charge transfer thus stronger Zr-O bonds compared to Al-O. A similar downward shift is also observed after Hf and Y substitution into the structure as these elements have additional d electron contributions to bonding. It can be concluded that the main causes of the sliding barrier are the breaking of O-Al, Al-O bonds and repulsive O-O interactions whilst the additional increase in the sliding barrier for RE_{GB}'s can be attributed to the stretched Al_D-O and RE-O bonds. Finally, in line with the sliding profiles, the calculated maximum stresses along the sliding path for Al_{GB}, Hf_{GB}, Zr_{GB} and Y_{GB} are 27.45 GPa, 30.86 GPa, 28.79 GPa and 32.45 GPa, respectively.

6.2.2 Cleavage

As mentioned in the methods section, two types of calculations are carried out for the cleavage fracture; r1 and r3 models. A comparison of the energy-separation ($x = fd_0$) data of these two models for Al_{GB}, Y_{GB}, Hf_{GB} and Zr_{GB} are provided in Figure 6.4 along with the UBER fit for the r3 data. As can be seen, when atoms are only allowed to relax along the cleavage axis [155] (r1 model), the total energy increases abruptly and results in a small energy barrier for RE added GB's contrasting the experimental data. A reason for such a contradiction can be the strains generated because of the greater size of REs compared to the Al atom. However an expected gradual increase is determined for the structure that is allowed to relax in all directions (r3 model) and the UBER designed for unrelaxed structures does not fit the r3 data as it is obtained

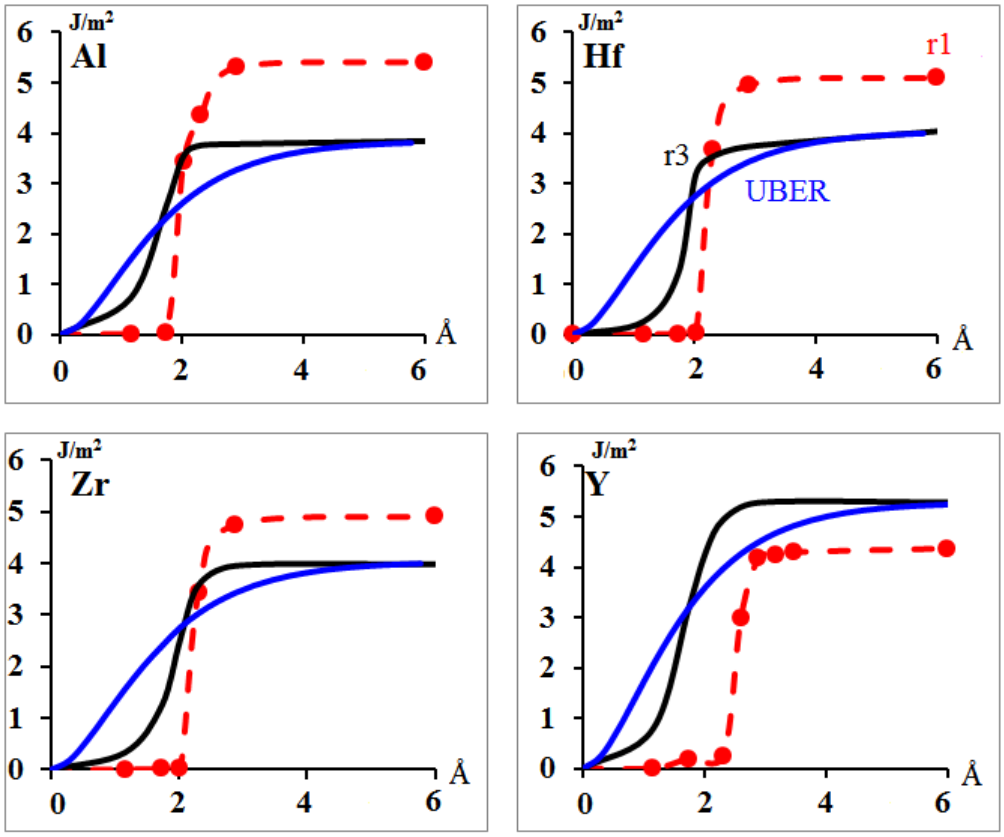

Figure 6.4: Energy per area versus separation for the structures relaxed in all directions (black), the structures with only z-axis relaxations (red) and the UBER fit.

by allowing relaxations in all direction for the whole structure. The maximum cleavage energies for r3 model are found to be $3.84 J/m^2$, $4.03 J/m^2$, $3.98 J/m^2$ and $5.29 J/m^2$ for Al_{GB}, Hf_{GB}, Zr_{GB} and Y_{GB} respectively. The higher cleavage energy for the RE-substituted structures are expected as it is shown in sliding calculations; the RE-O bonds are much stronger, requiring a greater energy to break.

Bond lengths, at openings d_0 and $1.5d_0$ are presented in Table 6.3. For the quadrivalent Hf substituted structures, Al-O and Hf-O bonds across the grain boundary interface contracts at $1.5d_0$. A similar trend, except for the RE-O contraction, is also determined for Hfs' isovalent, Zr containing model. This 'shortening behaviour' is previously observed in Y-doped Al_2O_3 GB tensile tests, and is suggested to be a result of strong

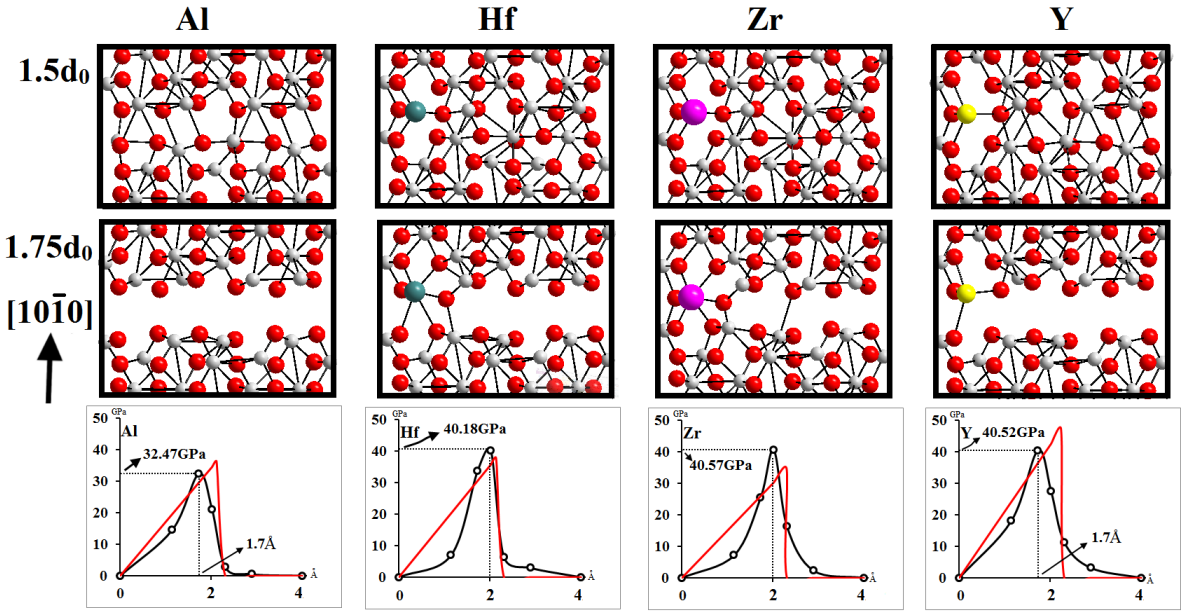

Figure 6.5: Stress vs strain plots along with the fit utilized from ref. [155], and atomic positions of the 1.5 and 1.75 cleaved structures.

Y-O bonds. However, unlike the quadrivalent Hf and Zr, in the trivalent Y_{GB} and Al_{GB} models, at $1.5d_0$, all cross interface bonds stretch and the total number of X-O bonds decrease. Such a difference implies that Y_{GB} and Al_{GB} models reach their critical stress at a smaller opening than $1.5d_0$.

The maximum stresses are calculated using two different methods: 1) From the slope of the energy-opening curve (method-1) 2) Utilizing a fit for relaxed cleavage calculations as suggested by Lazar *et. al.* [155, 160] (method-2). The stress curve obtained from the UBER model is not demonstrated since it did not fit the energy-separation data of the fully relaxed r3 model. When the total energy-separation values are fitted to Eq. 3.41, all models reach their critical stress above an opening of 2.2Å and Zr_{GB} and Hf_{GB} are calculated to have a smaller critical stress than the Al_{GB}. However it is known that addition of reactive elements (Zr, Hf), increases the creep resistance of alumina GBs and the atomic model and separations provided in Figure 6.5 and Table 6.3 reveals that all models are expected to separate before or at 2 Å. Therefore method-

	X (Å):	Al	Hf	Zr	Y
		$3.84 J/m^2$	$4.03\ J/m^2$	$3.98\ J/m^2$	$5.29\ J/m^2$
0	**Al-O:**	1.76(x2), 1.86(x3)	1.76, 1.80, 1.85, 1.86, 1.87	1.77, 1.81, 1.85, 1.86, 1.87	1.78(x2), 1.83, 1.84, 1.89
	X-O:	1.91, 1.99	2.04, 2.14	2.06, 2.17	2.13, 2.29
	# L<2.7Å:	17	16	16	16
1.5	**Al-O:**	1.85(x2), 2.66(x2), 2.67	1.74, 1.76, 1.79, 1.83, 1.86	1.74, 1.81, 1.83, 1.88, 1.89	1.75, 1.81, 2.10, 2.46, 2.47
	X-O:	2.67, 2.71	2.05, 2.13	2.10, 2.18	2.23, 2.38
	# L<2.7Å:	8	20	19	12

Table 6.3: Atomic separations across the grain boundary interface for uncleaved and 1.5d0 cleaved structures and the total number of atomic separations smaller than 2.7Å.

2 neither agrees with the experimental data nor does it follow the atomic separations for the r3 model, because it is derived for structures that are relaxed only along the cleavage axis or nearby the grain boundary interface. Thus, the critical stresses are determined using method-1, as 32.47 GPa, 40.18 GPa, 40.57 GPa and 40.52 GPa for Al_{GB}, Hf_{GB}, Zr_{GB} and Y_{GB} respectively, which is in very good agreement with the maximum stress obtained for pure (31GPa) and Y-substituted (39GPa) $\Sigma 3$ grain boundary in previous tensile calculations [102].

According to the ductility parameter D, Al_{GB}, Hf_{GB} are brittle while Y_{GB}, Zr_{GB} are ductile. However, as expected the ZCT condition predicts a brittle Al_{GB}, Hf_{GB}, Zr_{GB} and Y_{GB} since, like most ceramics, alumina is a brittle material. Figure 6.5 demonstrates the bonding across the grain boundaries at $1.5d_0$ and $1.75d_0$. In agreement with the changes in bond lengths, Y_{GB} and Al_{GB} reach their maximum stresses at smaller openings as their cross interface bonds have already been elongated at $1.5d_0$. Thus it can be suggested that doping alumina grain boundaries with trivalent reactive elements increases the cleavage energy without changing its mechanical behaviour, and doping with quadrivalent reactive elements increases both the cleavage energy and the

ductility of alumina. Such a proposition is in line with experimental observations since Zr and Hf have been observed to increase the ductility of alumina grain boundaries while decreasing the creep rate [174].

6.3 Conclusion

In order to investigate the effects of reactive elements on alumina grain boundaries, sliding and cleavage processes are studied in Hf, Zr, and Y containing structures. Contribution of d electrons in bonding is determined to be the main cause of increased critical sliding and cleavage energies. During sliding, in addition to the energy required to break the bonds, strains generated due to O-O repelling is observed to contribute to the sliding barrier. Unlike previously suggested for $\Sigma 11$ Al_2O_3 GBs, no correlation is observed between the magnitude in increase and the ionic radii. Cleavage models revealed that Hf and Zr added structures reach their maximum stress values at a greater opening compared to un-doped Alumina. Therefore, in line with experimental observations [174], the quadrivalent Hf and Zr atoms are suggested to increase the ductility of Al_2O_3.

The calculated shear stress value of 27.45 GPa for the pure $\Sigma 3$ grain boundary agrees well with the shear stregth of Al_2O_3 (28 GPa) as obtained by nano-indentation tests and the theoretical shear strength of Al_2O_3 that is calculated as 26.2 GPa [175]. Moreover the critical cleavage stress values for the pure (32.47 GPa) and Y-added (40.52 GPa) grain boundaries agree well with the results of previous theoretical tensile tests. (31 GPa for pure and 39 GPa for Y-doped grain boundary) [101]

It is widely accepted that the detailed behaviour of every grain boundary is different. Even though this system constitutes only a small portion of all possible grain boundaries, qualitatively a similar increase in the energy barriers is expected after RE addition due their d electron contribution.

Chapter 7

Conclusion and Future Work

7.1 Conclusion

Different computational tools are utilized in this thesis to investigate the effects of reactive elements (REs) and impurities on thermal barrier coatings. The DFT based VASP package is used to calculate the total electronic energy, the ATAT package is used to calculate vibrational frequencies, DOS and ELF are exploited to investigate the atomic level mechanisms underlying the effects of REs. Through a semi-empirical approach, the mechanical behaviour of alumina grain boundaries and the diffusion in bulk NiAl are studied. The main contributions of this research can be summarised as follows:

- The effects of reactive elements (Hf, Y, Zr, Cr), additive (Pt) and impurity (S) on the adhesion of the β-NiAL/Al_2O_3 interface are elaborated. The main atomic level contribution to the increased adhesion is determined as the formation of a mixed Ni-RE-O bond in single RE-doped and RE+X (X=RE,S,Pt) co-doped interfaces. On the other hand, the deterioration of the adhesion by S is mainly due to the breaking of bonds in the vicinity of S and the O-S repulsion across the interface. In the Hf+X (X=Y,Zr) co-doped interfaces, formation of an ionic Hf-O-RE bond is revealed to contribute to the additional strengthening of the adhesion,

unlike the Cr+X (X=Hf, Y) co-doped interfaces where the Cr atom is found not to participate in an ionic Cr-O-RE bond formation. Finally, in S+X (X=Hf, Cr, Pt) segregated interfaces, Cr and Hf are shown to mitigate the detrimental effects of S to some extent, with Hf promoting additional Al-S formation. However, the addition of Pt is not as effective.

- Since Pt and RE's have been shown to decrease the S concentration at the interface, the interstitial and vacancy mediated diffusion of S in bulk NiAl with the influence of Pt and Hf is studied. During its interstitial diffusion, substituting a Ni atom with Pt is found to decrease the coordination number of S due to Pt-S repulsion, allowing it to diffuse faster, while the substitution of an Hf atom to an Al site is shown to promote a strong Hf-S bond formation, hence decelerating segregation of S. Similarly, the Pt-S repulsion is determined to slow down the vacancy mediated S diffusion. From the Arrhenius plots, a critical temperature, 840°C, is observed below which S diffuses as an interstitial and Pt accelerates the diffusion. Above this temperature, a vacancy mediated diffusion and a decreased diffusion rate are expected after the addition of Pt.

- To further examine the effects of reactive elements on thermal barrier coatings, the alumina grain boundaries containing a RE (Hf, Zr and Y) is examined. Different fits are exploited to determine the maximum sliding and cleavage energies and critical stresses for the undoped and doped grain boundaries. The addition of RE is shown to increase the maximum sliding and cleavage stress due to their d-electron contribution. Furthermore, the comparative study of bond separation and the atomic geometry of these grain boundaries indicated an increased ductility of alumina after the addition of quadrivalent Hf and Zr.

7.2 Suggested Future Work

Based on this work, more research is needed in the following areas:

- A more complicated and realistic model of the $NiAl/Al_2O_3$ interface is currently being generated by K. Chen to include the initial formation of vacancies before the segregation of REs or S to the interface.

- A dynamic investigation of the interface adhesion by including the diffusion of additives and S from the bulk NiAl to the $NiAl/Al_2O_3$ interface can be carried out to determine their preferred segregation sites, changes in the atomic structure and their effects on adhesive trends.

- Other S diffusion mechanisms can be elucidated to determine its most favourable diffusion mechanism and the influence of other elements on its diffusion rate.

- In order to rationalize the effects of quadrivalent and trivalent reactive elements on grain boundary strengthening, effects of other REs on the ductility of the alumina grain boundaries can be investigated.

Bibliography

[1] A. Christensen, E. Asche, and C. E.A, "Atomic level properties of thermal barrier coatings:characterization of metal ceramic interfaces," in *Chemical Dynamics in Extreme Environments* (R. Dressler, ed.), World Scientific, 2001.

[2] D. Clarke and C. Levi, "Materials design for the next generation thermal barrier coatings," *Ann. Rev. of Mater. Res.*, vol. 33, p. 383, 2003.

[3] P. Wright and A. Evans, "Mechanisms governing the performance of the thermal barrier coatings," *Current opinion in solid state and Materials Science*, vol. 4, no. 3, p. 255, 1999.

[4] R. Hashaikeh, "Fabrication of thermal barrier coating using electrochemical methods," Master's thesis, McGill University, 2000.

[5] N. M. Meta, *in situ untersuchung der nitridierung von β und δ zirconium-scandium-oxiden*. PhD thesis, Eberhard-Karls-Universitt Tbingen, 2007.

[6] H. Xu, S. Gong, Y. Zhang, and C. Zhang, "Experimental and computational study on hot fatigue process on thermal barrier coatings bt eb-pvd," *Intermetallics*, vol. 13, no. 3-4, 2005.

[7] G. Newaz, S. Nusier, and Z. Chaudhury, "Damage accumulation mechanisms in thermal barrier coatings.," *J. Eng. Mat. Tech.*, vol. 120, p. 149, 1998.

[8] B. Pint, "Experimental observations in support of the dynamic-segregation theory to explain the reactive-element effect," *Oxidation of Metals*, vol. 45, no. 1/2, 1996.

[9] V. Tolpygo and D. Clarke, "Surface rumpling of (ni,pt)al bond coat induced by cyclic oxidation," *Acta. Mater.*, vol. 48, p. 3283, 2000.

[10] F. Stephens P.J. ad Devlin, C. Chabalowski, and M. Frisch, "*Ab Initio* calculation of vibrational absorption and circular dichroism spectra using density functional force fields.," *J. Phys. Chem*, vol. 98, no. 45, p. 11623, 1994.

[11] Kresse,G. and Schmid,M. and Napetsching,E. and Ahishkin, M. and Kohler, L. and Varga, P., "Structure of the ultrathin aluminum oxide film on nial(110)," *Science*, vol. 308, p. 1440, 2005.

[12] Y. Lykhach, V. Moroz, and Y. M., "Formation of epitaxial $al_2o_3/nial(110)$ films: aluminium deposition," *App. Surf. Sci.*, vol. 241, p. 250, 2005.

[13] X. Torrelles, F. Wendler, O. Bikondoa, H. Isern, W. Mortiz, and G. Castro, "Strucutre of the clean nial surface and the $al_2o_3/nial$ interface by measurements of crystal truncation rods.," *Surf. Sci.*, vol. 487, p. 97, 2001.

[14] R. Jaeger, H. Kuhlenbeck, H.-J. Freund, M. Wuttig, W. Hoffmann, R. Franchy, and H. Ibach, "Formation of a well-ordered aluminium oxide overlayer by oxidation of nial(110)," *Surf. Sci.*, vol. 259, no. 3, p. 235, 1991.

[15] A. Stierle, F. Renner, and R. Streitel, "X-ray diffraction study of the ultrathin al_2o_3 layer on nial(110)," *Science*, vol. 303, no. 5664, p. 1652, 2004.

[16] E. Jarvis and E. Carter, "Metallic character of the al_2o_3(0001)-($\sqrt{3}x\sqrt{3}$)r $\pm$ 9° surface reconstruction," *J. Phys. Chem.*, vol. 105, p. 4045, 2001.

[17] K. Carling and E. Carter, "Effects of segregating elements on the adhesive strength and structure of the α-al_2o_3/β-nial interface," *Acta Mater.*, vol. 55, p. 2791, 2007.

[18] A. Rosenhahn, J. Schneider, C. Becker, and K. Wandelt, "The formation of al_2o_3 layers on ni_3al(111)," *Applied Surf. Sci.*, vol. 142, p. 169, 1999.

[19] F. Qin, N. Magtoto, and J. Kelber, "Ho-induced instability of al_2o_3/nial(110) and al_2o_3/nial(111) thin films under non-uhv conditions," *Surf. Sci.*, vol. 565, no. 2-3, p. L277, 2004.

[20] S. Pevedic, D. Schmaus, and C. Cohen, "Formation of a well-ordered ultrathin aluminum oxide film on ni(111): Determination of its thickness, composition and structure," *Surf. Sci.*, vol. 602, pp. 67–76, 2008.

[21] M. Yoshitake, T. Lay, and W. Song, "Well-ordered ultrathin al_2o_3 film formation on nial(110) by high-temperature oxidation," *Surf. Sci.*, vol. 564, no. 1-3, p. 211, 2004.

[22] M. Yoshitake, B. Mebarki, and T. Lay, "Crystallinity and thickness control of well-ordered ultrathin al_2o_3 film on nial(110)," *Surf. Sci. Lett.*, vol. 511, p. 313, 2002.

[23] C. Becker, "Preferential cluster nucleation on long range super structures on al_2o_3/ni_3al(111)," *Surf. Sci.*, vol. 486, no. 1-2, p. L443, 2001.

[24] S. Addepalli, B. Ekstrom, N. Magtoto, and J. Kelber, "Stm atomic-scale characterization of the γ'-al_2o_3 on ni_3al(111)," *Surf. Sci.*, vol. 442, p. 385, 1999.

[25] J. Angenete, K. Stiller, and E. Bakchinova, "Microstructural and microchemical development of simple and pt-modified aluminide diffusion coatings during long term oxidation at 1050c," *Surface and Coatings Technology*, vol. 176, p. 272, 2004.

[26] D. Sondericker and F. Jona, "Atomic structure of alloy surfaces ni$_3$al," *Phys. Rev. B*, vol. 34, no. 10, p. 6770, 1986.

[27] S. Chen, A. Voter, and D. Srolovitz, "oscilattory surface relaxations ni, al and their ordered alloys," *Phys. Rev. Lett*, vol. 57, no. 11, p. 1308, 1986.

[28] V. Kim and V. Kuznetsov, "Surface energy of ordered nial and ni$_3$al alloys," *Russ. Phys. J.*, vol. 37, no. 10, p. 985, 1995.

[29] D. Mullins and S. Overbury, "The structure and composition of the nial(110) and nial(100) surfaces," *Surf. Sci.*, vol. 199, p. 141, 1988.

[30] J. Noonan and H. Davis, "Atomic arrangements at metal surfaces," *Science*, vol. 234, p. 310, 1972.

[31] H. Davis and J. Noonan, "Rippled relaxation in the (110) surface of the ordered metallic alloy nial," *Phys. Rev. Lett*, vol. 54, no. 6, p. 566, 1985.

[32] H. Davis and J. Noonan, "Atomic rippling of ordered alloy surface nial(110)," *J. Vac. Sci. Technol. A*, vol. 3, no. 3, p. 1507, 1985.

[33] S. Yalisove and W. Graham, "Multilayer rippled structure of the nial(110) surface: a medium energy ion scattering study," *Surf. Sci.*, vol. 183, p. 556, 1987.

[34] L. Senying and J. Leiro, "Rippled relaxation of ordered nial(110) surface," *Surf. Sci.*, vol. 397, p. 48, 1998.

[35] M. Kang and E. Mele, "Nial first principle determination of the rippled relaxation," *Phys. Rev. B*, vol. 36, no. 14, p. 7371, 1987.

[36] T. Nishimura, Y. Hoshino, T. Okazawa, and Y. Kido, "Structure of ultrathina aluminum oxide layer on nial(110) substrate," *Phys. Rev. B*, vol. 77, p. 073405, 2008.

[37] J. Libuda, F. Winkelman, and M. Baumer, "Structure and defect of an ordered alumina film on nial(110)," *Surf. Sci.*, vol. 318, p. 61, 1994.

[38] I. Rivoaland, V. Maurice, P. Josso, M.-P. Bacos, and Marcus.P., "The effect of sulfur segregation on the adherence of the thermally-grown oxide on NiAl - I:Sulfur segregation on the metallic surface of NiAl(001) Single crystals and at NiAl(001)/Al_2O_3 interfaces," *Oxidation of Metals*, vol. 60, no. 1/2, p. 137, 2003.

[39] I. Rivoaland, V. Maurice, P. Josso, M.-P. Bacos, and Marcus.P., "The effect of sulfur segregation on the adherence of the thermally-grown oxide on NiAl - II: The oxidation behavior at 900°C of standard, desulfurized of sulfur-doped NiAl(001) single-crystals," *Oxidation of Metals*, vol. 60, no. 1/2, p. 159, 2003.

[40] J. Haynes, Y. Zhang, W. Lee, B. Pint, I. Wright, and K. Cooley, "Effects of platinum additios and sulfur impurities on the microstructure and scale adhesion behavior of single-phase cvd aluminide bond coatings," in *TMS Annual Meeting*, 1999.

[41] J. Smialek, D. Jayne, J. Schaeffer, and W. Murphy, "Effects of hydrogen annealing, sulfur segregation and diffusion on the cyclic oxidation resistance of superalloys: a review," *Thin Solid Films*, vol. 253, p. 285, 1994.

[42] H. Grabke, D. Wiemer, and Viefhaus, "Segregation of sulfur during growth of oxide scales," *App. Surf. Sci.*, vol. 47, p. 243, 1991.

[43] J. Smialek, "Maintaining adhesion of protective al_2o_3 scales," *JOM*, vol. 52, no. 1, p. 22, 2000.

[44] J. Haynes, B. Pint, K. More, Y. Zhang, and I. Wright, "Influence of sulfur, platinum and hafnium on the oxidation behavior of CVD NiAl bond coatings," *Oxidation of Metals*, vol. 58, no. 5/6, p. 513, 2002.

[45] I. Bennett and W. Sloof, "Modelling the influence of reactive elements on the work of adhesion between a thermally grown oxide and a bond coat alloy," *Materials and Corrosion*, vol. 57, no. 3, p. 223, 2006.

[46] Y. Jiang, J. Smith, and A. Evans, "First principles assessment of metal/oxide interface adhesion," *Applied Physics Letters*, vol. 92, no. 141918, 2008.

[47] J. Feng, W. Zhang, W. Jiang, and H. Gu, "Interfaces between al_2o_3 and $\beta - ni_{1-x}al_x$ alloys: Complex structures and ab initio thermodynamics," *Phys. Rev. Lett.*, vol. 97, no. 24, p. 246102, 2006.

[48] W. Zhang, J. Smith, X. Wang, and A. Evans, "Influence of sulfur on the adhesion of the nickel/alumina interface," *Phys. Rev. B*, vol. 67, p. 245414, 2003.

[49] K. Carling, W. Glover, H. Gunaydin, T. Mitchell, and E. Carter, "Comparison of s, pt and hf adsorbtion on nial(110)," *Surface Science*, vol. 600, p. 2079, 2006.

[50] P. Hou and K. McCarty, "Surface and interface segregation in β-NiAl with and without Pt addition," *Scripta Mater.*, vol. 54, no. 5, p. 937, 2006.

[51] T. Gheno, D. Monceau, D. Oquab, and Y. Cadoret, "Characterization of sulfur distribution in Ni-Based superalloy and thermal barrier coatings after high temperature oxidation:A SIMS analysis," *Oxidation of Metals*, vol. 73, p. 95, 2010.

[52] B. Gleeson, W. Wang, S. Hayashi, and D. Sordelet, "Effects of platinum on the interdiffusion and oxidation behaviour of ni-al based alloys," *Materials Science Forum*, 2004.

[53] Y. Zhang, W. Lee, J. Haynes, I. Wright, B. Pint, K. Cooley, and P. Liaw, "Effects of pt incorporation on the isothermal oxidation behavior of chemical vapor deposition aluminide coatings," *Metall Mater Trans A*, vol. 32, no. 7, p. 1727, 2001.

[54] C. Jiang, M. Besser, D. Sordelet, and B. Gleeson, "A combined first-principles and experimental study of the lattice site preference of pt in b2 nial," *Acta Mater.*, vol. 53, p. 2101, 2005.

[55] K. Marino and E. Cater, "The effect of platinum on defect formation energies in β-NiAl," *Acta Mater*, vol. 56, no. 14, p. 3502, 2008.

[56] R. Yu and P. Hou, "First-principles calculations of the effect of pt on nial surface energy and the site preference of pt," *Applied Phys.Let.*, vol. 91, no. 1, p. 011907, 2007.

[57] Y. Jiang and J. Smith, "Pt effects in γ-ni(al)/α-al_2o_3 adhesion," *J. Mater. Sci.*, vol. 44, p. 1734, 2009.

[58] K. Marino and E. Cater, "The effect of platinum on Al diffusion kinetics in β-NiAl: Implications for thermal barrier coating lifetime," *Acta Mater*, vol. 58, p. 2726, 2010.

[59] I. Rommerskirchen and V. Kolarik, "Oxidation of β-nial, undoped and doped with ce, y, hf," *Materials and Corrosion*, vol. 47, p. 625, 1996.

[60] H. Guo, L. Sun, H. Li, and S. Gong, "High temperature oxidation behavior of hafnium modified nial bond coat in eb-pvd thermal barrier coating system," *Thin Solid Films*, vol. 516, p. 5732, 2008.

[61] E. Dickey, B. Pint, K. Alexander, and I. Wright, "Oxidation behavior of platinum-aluminum alloys and the effect of zr doping," *J Mater. Res.*, vol. 14, no. 12, p. 4531, 1999.

[62] J. Jedlinski and S. Mrowec, "The influence of implanted yttrium on the oxidation behaviour of β-nial," *materials Science and Engineering*, vol. 87, p. 281, 1987.

[63] B. Pint, I. Wright, W. Lee, Y. Zhang, K. Prussner, and K. Alexander, "Substrate and bond coat compositions:factors affecting alumina scale adhesion," *Materials Science and Engineering*, p. 201, 1998.

[64] E. Schumann, J. Yang, and M. Graham, "Direct Observation of the interaction of yttrium and sulfur in oxidized NiAl," *Scripta Materialia*, vol. 34, no. 9, p. 1365, 1996.

[65] E. Schumann, J. Yang, M. Ruhle, and M. Graham, "High-resolution sims and analytical tem evaluation of alumina scales on β-nial containing zr and y," *Oxidation of Metals*, vol. 46, no. 1/2, p. 37, 1996.

[66] Funkenbusch,A.W. and Smeggil,J.G. and Bornstein,N.S., "Reactive element-sulfur interaction and oxide scale adherence," *Metallurgical Transactions A*, vol. 16A, p. 1164, 1985.

[67] B. Pint, "The oxidation behavior of oxide-dispersed β-nial: I.short-term performance at 1200∘c," *Oxidation of Metals*, vol. 49, no. 5/6, 1998.

[68] B. Pint, K. More, and I. Wright, "Effect of quarternary additions on the oxidation behavior of hf-doped nial," *Oxidation of Metals*, vol. 59, no. 3/4, 2003.

[69] J. Smialek, "Sulfur impurities and the microstructure of alumina scales," *NASA/TM*, vol. 107375, 1996.

[70] J. Raynolds, J. Smith, G. Zhao, and D. Srolovitz, "Adhesion in nial-cr from first principles," *Phys. Rev. B*, vol. 53, no. 20, p. 13883, 1996.

[71] H. Grabke, M. Brumm, and B. Wagemann, "The oxidation of nial," *Materials and Corrosion*, vol. 47, p. 675, 1996.

[72] M. Brumm and H. Grabke, "The oxidation behaviour of nial-i. phase transformations in the alumina scale during oxidation of nial and nial-cr alloys," *Corrosion Science*, vol. 33, no. 11, p. 1677, 1992.

[73] P. Hou, "Segregation phenomena at thermally grown al_2o_3/alloy interfaces," *Annu. Rev. Mater. Res.*, vol. 38, p. 275, 2008.

[74] D. Prajitno, B. Gleeson, and D. Young, "The cyclic oxidation behaviour of α-cr+β-nial alloys with and without trace zr addition," *Corrosion Science*, vol. 39, no. 4, p. 639, 1997.

[75] S. Hong, A. Anderson, and J. Smialek, "Sulfur at nickel-alumina interfaces," *Surf. Sci.*, vol. 230, p. 175, 1990.

[76] D. Lees, "On the reasons for the effects of dispersions of stable oxides and additions of reactive elements on the adhesion and growth-mechanisms of chromia and alumina scales-the sulfur effect?," *Oxidation of Metals*, vol. 27, no. 1/2, p. 75, 1987.

[77] V. Tolpygo and D. Clarke, "Microstructural evidence for counter-diffusion of aluminum and oxygen during the growth of alumina scales," in *5th international Conference on the Microscopy of Oxidation*, 2002.

[78] B. Pint, "Optimization of reactive-element additions to improve oxidation performance of alumina-forming alloys," *J. Am. Ceram. Soc.*, vol. 8, no. 4, p. 686, 2003.

[79] B. Pint and K. More, "Characterization of alumina interfaces in tbc systems," *J. Mater. Sci.*, vol. 44, p. 1676, 2009.

[80] S. Frank, S. Divinski, U. Sodervall, and C. Herzig, "Ni tracer diffusion in the b2-compound nial: Influence of temperature and composition," *Acta. Mater.*, vol. 49, p. 1399, 2001.

[81] C. Herzig and S. Divinski, "Bulk and grain boundary diffusion in intermetallic compounds," in *Diffusion processes in advanced technological materials* (D. Gupta, ed.), William Andrew Inc and Springer-Verlag, 2005.

[82] R. Nakamura, K. Fujita, Y. Iijima, and M. Okada, "Diffusion mechanisms in b2 nial phase studied by experiments on kirkendall effect and interdiffusion under high pressures," *Acta. Mater.*, vol. 51, p. 3861, 2003.

[83] G. Chen, J. Zhng, and K. Xu, "self-diffusion of ni in b2 type intermetallic compound nial," *J. Alloys Comp.*, vol. 430, p. 102, 2007.

[84] K. Marino and E. Carter, "First-principles characterization of ni diffusion kinetics in β-nial," *Phys. Rev. B*, vol. 78, no. 184105, 2008.

[85] Q. Xu and A. Van der Ven, "First-principles investigation of migration barriers and point defect complexes in B2-NiAl," *Intermetallics*, vol. 17, p. 319, 2009.

[86] K. A. Marino and E. A. Carter, "Ni and al diffusion in ni-rich nial and the effect of pt additions," *Intermetallics*, vol. 18, no. 8, p. 1470, 2010.

[87] Y. Mishin, A. Lozovi, and A. Alavi, "Evaluation of diffusion mechanisms in NiAl by embedded-atom and first-principles calculations," *Phys. Rev. B*, vol. 67, no. 014201, 2003.

[88] B. Soule De Bas and D. Farkas, "Molecular dynamics simulations of diffusion mechanisms in nial," *Acta. Mater.*, vol. 51, p. 1437, 2003.

[89] S. Divinski and C. Herzig, "On the six-jump cycle mechanism of self-diffusion in nial," *Intermetallics*, vol. 8, p. 1357, 2000.

[90] G. Hancock and B. McDonnel, "Diffusion in the intermetallic compound nial," *Phys. Stat. Sol. (a)*, vol. 4, p. 143, 1971.

[91] Y. Minamino, Y. Koizumi, N. Tsuji, M. Morioka, K. Hirao, and Y. Shirai, "Pt diffusion in b2-type ordered nial intermetallic compound and its diffusion mechanisms," *Sci. Tech. Adv. Mater.*, vol. 1, p. 237, 2000.

[92] R. Bouchet and R. Mevrel, "Calculating the composition-dependent diffusivity matrix along a diffusion path in ternary systems application to β-(ni,pt)al," *Calphad*, vol. 23, p. 295, 2003.

[93] P. Hou and K. Priimak, "Interfacial segregation, pore formation and scale adhesion on NiAl alloys," *oxidation of metals*, vol. 63, no. 1-2, p. 113, 2005.

[94] Christien,F. and Pouteau,P. and Le Gall,R. and Saindrenan,G. and Jaslier,Y., "Segregation du soufre a la surface d'un materiau multicouche. Role du platine dans l'ecaillage des couches d'oxyde protectrices," *J. Phys. IV France*, vol. 10, p. 173, 2000.

[95] S. Fabris and C. Elsasser, "Σ13(1014) twin in α-Al_2O_3:A model for a general grain boundary," *Phys. Rev. B*, vol. 64, p. 245117, 2001.

[96] J. Buban, K. Matsunaga, J. Chen, N. Shibata, W. Ching, T. Yamamoto, and Y. Ikuhara, "Grain boundary strengthening in alumina by rare earth impurities," *Science*, vol. 311, p. 212, 2006.

[97] F. Wakai, T. Nagano, and T. Iga, "Hardening in creep of alumina by zirconium segregation at the grain boundary," *J. Am. Ceram. Soc.*, vol. 80, no. 9, p. 2361, 1997.

[98] S. Azuma, N. Shibata, S. D. Findlay, T. Mizoguchi, T. Yamamoto, and Y. Ikuhara, "HAADF-STEM observations of a Σ13 grain boundary in α-Al_2O_3 from two orthogonal directions," *Phil. Mag. Lett.*, vol. 90, no. 8, p. 539, 2010.

[99] S. Fabris, S. Nufer, C. Elsasser, and T. Gemming, "Prismatic Σ3 twin boundary in α-Al_2O_3 investigated by density functional theory and transmission electron microscopy," *Phys. Rev. B*, vol. 66, p. 155415, 2002.

[100] S. Fabris and C. Elsasser, "First-principles analysis of cation segregation at grain boundaries in α-Al_2O_3," *Acta Mater.*, vol. 51, p. 71, 2003.

[101] J. Cho, H. M. Chan, M. P. Harmer, and J. Rickman, "Influence of Yttrium doping on grain misorientation in aluminum oxide," *J. Am. Ceram. Soc.*, vol. 81, no. 11, p. 3001, 1998.

[102] J. Chen, Y. Xu, P. Rulis, L. Ouyang, and W. Ching, "Ab initio theoretical tensile test on Y-doped $\Sigma = 3$ grain boundary in α-Al_2O_3," *Acta Mater.*, vol. 53, p. 403, 2005.

[103] M. Castillo-Rodriguez, A. Munoz, J. Castaing, P. Veyssiere, and A. Dominiguez-Rodriguez, "Basal slip latent hardening by prism plane slip dislocations in sapphire (α-al_2o_3)," *Acta Mater.*, vol. 58, p. 5610, 2010.

[104] K. Kishitake, H. Era, and S. Baba, "Tensile strength of plasma-sprayed alumina and/or zirconia coating on titanium," *ASM Int.*, vol. 4, p. 353, 1995.

[105] Y. Zhang, S. Lu, G.-H.and Deng, T. Wang, H. Xu, M. Kohyama, and R. Yamamoto, "Weakening of an aluminum grain boundary induced by sulfur segregation: A first principles computational tensile test," *Phys. Rev. B*, vol. 75, p. 174101, 2007.

[106] H. Yoshida, Y. Ikuhara, and T. Sakuma, "High-temperature creep resistance in rare earth doped fine grained Al_2O_3," *J. Mater. Res.*, vol. 13, no. 9, p. 2597, 1998.

[107] B. Veal, A. Paulikas, B. Gleeson, and P. Hou, "Creep in α-Al_2O_3 thermally grown on β-NiAl and NiAlPt alloys," *Surf. Coat. Tech.*, vol. 202, p. 608, 2007.

[108] P. Kenway, "Calculated structures and energies of grain boundaries in α-Al_2O_3," *J. Am. Ceram. Soc.*, vol. 77, no. 2, p. 349, 1994.

[109] A. Marinopoulos and C. Elsasser, "Microscopic structure and bonding at the rhombohedral twin interface in α-Al_2O_3," *Acta. Mater.*, vol. 48, p. 4375, 2000.

[110] A. Marinopoulos, S. Nufer, and C. Elsasser, "Interfacial structures and energetics of basal twin in α-Al_2O_3: First principles density functional and empirical calculations," *Phys. Rev. B*, vol. 63, p. 165112, 2001.

[111] I. Milas and C. E.A, "Effect of dopants on alumina grain boundary sliding: implications of creep inhibition," *J. Mater. Sci.*, vol. 44, p. 1741, 2009.

[112] I. Milas, B. Hinnemann, and C. E.A, "Structure of and ion segregation to an alumina grain boundary: implications for growth and creep," *J. Mater. Res.*, vol. 23, p. 1494, 2008.

[113] O. Ruano, J. Wadsworth, and O. D. Sherby, "Deformation of fine-grained alumina by grain boundary sliding accommodated by slip," *Acta Mater.*, vol. 51, p. 3617, 2003.

[114] T. Hoche, P. Kenway, H.-J. Kleebe, M. Finnis, and M. Ruhle, "The structure of special grain boundaries in α-Al_2O_3," *J. Phys. Chem. Solids*, vol. 55, p. 1067, 1994.

[115] J. Cho, M. P. Harmer, H. M. Chan, J. Rickman, and A. M. Thompson, "Effect of Yttrium and lanthanum on tensile creep behavior of aluminum oxide," *J. Am. Ceram. Soc.*, vol. 80, p. 1013, 1997.

[116] N. Du, Y. Qi, P. Krajewski, and A. Bower, "Aluminium $\sigma 3$ grain boundary sliding enhanced by vacancy diffusion," *Acta. Mater.*, vol. 58, p. 4245, 2010.

[117] K. Nakamura, T. Mizoguchi, N. Shibata, K. Matsunaga, T. Yamamoto, and Y. Ikuhara, "First-principles study of grain boundary sliding in α-Al_2O_3," *Phys. Rev. B*, vol. 75, p. 184109, 2007.

[118] G. Kresse and J. Furthmuller, "Efficient Iterative Schemes for *ab initio* Total-energy Calculations Using a Plane-wave Basis Set," *Phys. Rev. B*, vol. 54, no. 16, p. 11169, 1996.

[119] H. Jonsson, G. Mills, and K. Jacobsen, "Nudged Elastic Band Method for Finding Minimum Energy Paths of Transitions," in *Classical and Quantum Dynamics in Condensed Phase Simulations* (B. Berne, G. Ciccotti, and D. F. Coker, eds.), p. 385, World Scientific, 1998.

[120] S. Wei and M. Chou, "*Ab initio* Calculation of Force Constants and Full Phonon Dispersions," *Phys. Rev. Lett*, vol. 69, no. 19, p. 2799, 1992.

[121] A. Van de Walle, M. Asta, and G. Ceder, "The Alloy Theoretic Automated Toolkit: A User Guide," *CALPHAD journal*, vol. 26, p. 539, 2002.

[122] P. Hohenberg and W. Kohn, "Inhomogeneous electron gas," *Phys. Rev.*, vol. 136, no. 3B, p. B864, 1964.

[123] W. Kohn and L. Sham, "Self-consistent equations including exchange and correlation effects," *Phys. Rev.*, vol. 140, no. 4A, p. A1133, 1965.

[124] K. Capelle, "A bird's-eye view of density-functional theory," in *Proceedings of the VIIIth Brazilian Summer School on Electronic Structure*, 2002.

[125] P. Dirac, "Note on exchange phenomena in the thomas atom," *Proc. Cambridge Phil. Soc.*, vol. 26, no. 3, p. 376, 1930.

[126] D. Ceperley and B. Adler, "Ground state of the electron gas by a stochastic method," *Phys. Rev. Lett*, vol. 45, no. 7, p. 566, 1980.

[127] J. Perdew, K. Burke, and Y. Wang, "Generalized gradient approximation for the exchange-correlation hole of a many-electron system," *Phys. Rev. B*, vol. 54, no. 23, p. 16533, 1996.

[128] X. Hua, X. Chen, and W. Goddard III, "*Generalized* generalized gradient approximation: An improved density functional theory for accurate orbital eigenvalues," *Phys. Rev. B*, vol. 55, no. 24, p. 16103, 1997.

[129] J. Perdew and S. Kurth, "Density functionals for non-relativistic coulomb systems in the new century," in *A primer in density functional theory* (M. M. C. Fiolhais, F. Nogueira, ed.), Springer, 2003.

[130] J. Hafner, "Atomic-scale computational materials science," *Acta Mater.*, vol. 48, p. 71, 2000.

[131] R. M. Martin, *Electronic Structure: Basic Theory and Practical Methods*. Cambridge University Press, 2004.

[132] D. Marx and J. Huttler, *Ab initio molecular dynamics: Basic theory and advanced methods*. Cambridge University Press, 2009.

[133] D. Vanderbilt, "Soft self-consistent pseudopotentials in a generalized eigenvalue formalism," *Phys. Rev. B*, vol. 41, no. 11, p. 7892, 1990.

[134] P. Blochl, "Projector augmented-wave method," *Phys. Rev. B*, vol. 50, no. 24, p. 17953, 1994.

[135] E. Mete, "Dft in practice: Part ii pseudopotentials," in *NanoDFT'09, Izmir institute of Technology*, 2009.

[136] N. Holzwarth, G. Matthews, R. Dunning, A. Tackett, and Y. Zeng, "Comparison of the projector augmented-wave, pseudopotential and linearizd augmented-plane-wave formalisms for density-functional calculations of solids," *Phys. Rev. B*, vol. 55, no. 4, p. 2005, 1997.

[137] J. D. Kresse, G., "From ultrasoft pseudopotentials to the projector augmented-wave method," *Phys. Rev. B*, vol. 59, no. 3, p. 1758, 1999.

[138] C. Choi and R. Elber, "Reaction path study of helix formation in tetrapeptides:effect of side chains," *J. Chem. Phys.*, vol. 94, p. 751, 1991.

[139] G. Henkelman, *Methods for Calculating Rates of Transitions with Application to Catalysis and Crystal Growth*. PhD thesis, University of Washington, 2001.

[140] G. Henkelman, G. Johannesson, and H. Jonsson, "Methods for Finding Saddle Points and Minimum Energy Paths," in *Theoretical Methods in Condensed Phase Chemistry* (S. Schwartz, ed.), vol. 5, Springer, 2001.

[141] G. Henkelman and H. Jonsson, "Improved tangent estimate in the nudged elastic band method for finding minimum energy paths and saddle points," *J. Chem. Phys.*, vol. 113, no. 22, p. 9978, 2000.

[142] G. Henkelman, B. Uberuaga, and H. Jonsson, "A climbing image nudged elastic band method for finding saddle points and minimum energy paths," *J. Chem. Phys.*, vol. 113, no. 22, p. 9901, 2000.

[143] N. Ashcroft and N. Mermin, *Solid State Physics*. Saunders College Publishing, 1st ed., 1976.

[144] R. Feynman, "Forces in molecules," *Phys. Rev.*, vol. 56, p. 340, 1939.

[145] A. Becke and E. K.E., "A simple measure of electron localization in atomic and molecular systems," *J. Chem. Phys*, vol. 92, p. 5397, 1990.

[146] J. Philibert, *Atom movements:Diffusion and mass transport in solids*. Les Editions de Physique, 1991.

[147] H. Mehrer, *Diffusion in Solids, Fundamentals, Methods, Materials, Diffusion controlled processes*. Springer-Verlag Berlin Heidelberg, 2007.

[148] J. Manning, "Diffusion kinetics for atoms in crystals," *Am. J. Phys.*, vol. 36, no. 10, p. 922, 1968.

[149] N. Stolwijk, M. Van Gend, and H. Bakker, "Self-diffusion in the intermetallic compound coga," *Phil. Mag. A*, vol. 42, no. 6, p. 783, 1980.

[150] M. Manjeera, *A first principles methodolgy for diffusion-coefficients in metals and dilute alloys*. PhD thesis, The Pennsylvania State University, 2008.

[151] G. Vineyard, "Frequency factors and isotope effects in solid state rate processes," *J. Phys. Chem. Solids*, vol. 3, no. 1-2, p. 121, 1957.

[152] C. Kao and Y. Chang, "On the composition dependencies of self-diffusion coefficients in b2 intermetallic compounds," *Intermetallics*, vol. 1, p. 237, 1995.

[153] I. Belova and G. Murch, "Tehe anti-structural bridge mechanism for diffusion in ordered alloys of the b2-type," *Intermetallics*, vol. 6, p. 115, 1998.

[154] E. Elcock, "Vacancy diffusion in ordered alloys," *Proc. Phys. Soc.*, vol. 73, p. 250, 1959.

[155] P. Lazar, *Ab initio modelling of mechanical and elastic properties of solids*. PhD thesis, University of Vienna, 2006.

[156] A. Griffith, "The phenomena of rupture and flow in solids," *Trans. Royal Soc. London Ser. A.*, vol. 221, p. 163, 1921.

[157] D. Roylance, "Introduction to fracture mechanics." Department of Materials Science and Engineering, MIT, 2001.

[158] G. Irwin, "Fracture dynamics," *Am. Soc. Mater.*, pp. 147–66, 1948.

[159] E. Orowan, "Fundamentals of brittle behavior in metals," in *Fatigue and Fracture of Metals (MIT Symposium)*, New York: Wiley and Sons, 1952.

[160] P. Lazar and R. Podloucky, "Cleavage fracture of a crystal: density functional theory calculations based on a model wihich includes structural relaxations," *Phys. Rev. B*, vol. 78, p. 104114, 2008.

[161] K. Kang and W. Cai, "Brittle and ductile fracture of semiconductor nanowires-molecular dynamics simulations," *Phil. Mag.*, vol. 87, p. 2169, 2007.

[162] J. Rice and R. Thomson, "Ductile versus brittle behavior of crystals," *Phil. Mag.*, vol. 29, p. 73, 1974.

[163] S. Zhou, A. Carlsson, and R. Thomson, "Crack blunting effects of dislocation emission from cracks," *Phys. Rev. Lett.*, vol. 72, no. 6, p. 852, 1994.

[164] C. Wang and C.-Y. Wang, "Density functional theory study of Ni/Ni_3Al interface alloying with Re and Ru," *Surf. Sci.*, vol. 602, no. 14, p. 2604, 2008.

[165] H. Monkhorst and J. Pack, "Special points for Brillouin-zone integrations," *Phys. Rev. B*, vol. 13, no. 12, p. 5188, 1976.

[166] J. Guo, D. Ellis, and D. Lam, "Electronic structure and energetics of sapphire (0001) and ($1\bar{1}02$) surfaces," *Phys. Rev. B*, vol. 45, no. 23, p. 13647, 1992.

[167] Y. Song, Z. X. Guo, R. Yang, and D. Li, "First principles study of site substitution of ternary elements in nial," *Acta Mater.*, vol. 49, p. 1647, 2001.

[168] M. Escano, T. Nguyen, H. Nakanishi, and H. Kasai, "Another way of looking at bonding on bimetallic surfaces: the role of spin polarization of surface metal d states," *J. Phys.:Condens. Matter*, vol. 21, no. 492201, p. 1, 2009.

[169] C. Jiang, "Site preference of transition-metal elements in B2 NiAl: A comprehensive study," *Acta Mater.*, vol. 55, p. 4799, 2007.

[170] J. Rose, J. Smith, and J. Ferrante, "Universal features of bonding in metals," *Phys. Rev. B*, vol. 28, p. 1835, 1983.

[171] N. Medvedeva, O. Mryasov, Y. N. Gornostyrev, D. Novikov, and A. Freeman, "First-principles total-energy calculations for planar shear and cleavage decohesion processes in B2-ordered NiAl and FeAl," *Phys. Rev. B*, vol. 54, p. 13506, 1996.

[172] J. Buban, S. Hanyu, K. Matsunaga, T. Yamamoto, and Y. Ikuhara, "Investigation of Y-doping in alumina grain boundaries using STEM," *Microsc. Microanal*, vol. 11, p. 1448, 2005.

[173] D. Alfe, G. Price, and M. Gillan, "Oxygen in the earth's core: a first principles study," *Phys. Earth. Plane. Int.*, vol. 110, p. 191, 1999.

[174] J. Wang and R. Raj, "Estimate of the Activation Energies for Boundary Diffusion from Rate-Controlled Sintering of Pure Alumina, and Alumina Doped with Zirconia or Titania," *J. Am. Ceram. Soc.*, vol. 73, no. 5, p. 1172, 1990.

[175] C. Lu, Y. W. Mai, P. L. Tam, and Y. G. Shen, "Nanoindentation-induced elastic-plastic transition and size effect in α-al2o3(0001).," *Philosophical Magazine Letters*, vol. 87, no. 6, p. 409, 2007.